TEDLA, GETACHEW EBUY, Ph.D. Designing and Testing a Molecularly Targeted Glioblastoma Theranostic: Experimental and Computational Studies. (2018)
Directed by Dr. Christopher L. Kepley. 140 pp.

With an extremely poor patient prognosis glioblastoma multiforme (GBM) is one of the most aggressive forms of brain tumor with a median patient survival of less than 15 months. While new diagnostic and therapeutic approaches continue to emerge, the progress to reduce the mortality associated with the disease is insufficient. Thus, developing new methods having the potential to overcome problems that limit effective imaging and therapeutic efficacy in GBM is still a critical need. The overall goal of this research was therefore to develop targeted glioblastoma theranostics capable of imaging disease progression and simultaneously killing cancer cells. To achieve this, the state of the art of liposome based cancer theranostics are reviewed in detail and potential glioblastoma biomarkers for theranostic delivery are identified by querying different databases and by reviewing the literature. Then tumor targeting liposomes loaded with $Gd_3N@C_{80}$ and doxorubicin (DXR) are developed and tested in vitro. Finally, the stability of these formulations in different physiological salt solutions is evaluated using computational techniques including area per lipid, lipid interdigitaion, carbon-deuterium order parameter, radial distribution of ions as well as steered molecular dynamic simulations. In conclusion the experimental and computational studies of this dissertation demonstrated that DXR and $Gd_3N@C_{80}$-OH loaded and lactoferrin & transferrin dual-tagged, PEGylated liposomes might be potential drug and imaging agent delivery systems for GBM treatment.

DESIGNING AND TESTING A MOLECULARLY TARGETED GLIOBLASTOMA THERANOSTIC: EXPERIMENTAL AND COMPUTATIONAL STUDIES

by

Getachew Ebuy Tedla

A Dissertation Submitted to
the Faculty of The Graduate School at
The University of North Carolina at Greensboro
in Partial Fulfillment
of the Requirements for the Degree
Doctor of Philosophy

Greensboro
2018

Approved by

_____
Committee Chair

APPROVAL PAGE

This dissertation written by GETACHEW EBUY TEDLA has been approved by the following committee of the Faculty of The Graduate School at the University of North Carolina at Greensboro.

Committee Chair_____

Committee Members_____

_____

_____

_____

Date of Acceptance by Committee

_____

Date of Final Oral Examination

ACKNOWLEDGEMENTS

I would like to express my deep appreciation to my committee chair Dr. Christopher L. Kepley for his critical comments, suggestions and guidance. Without his support this dissertation would not have been possible. I would like to thank my committee members, Dr. Anthony Dellinger, Dr. Dennis R. Lajeunesse and Dr. Ethan Will Taylor for their willingness and for opening their door every time I needed a discussion. Thanks also to Dr. Kristen Reinhardt for providing access to the supercomputer and the UNCG department of nanoscience for the financial support. My heart felt gratitude goes to my Johanna & Amy, my dear parents, brothers and sisters. Above all, I thank the Almighty God for his infinite love and care.

TABLE OF CONTENTS

Page

LIST OF TABLES

Page

LIST OF FIGURES

Page

CHAPTER I

INTRODUCTION

I.1 Significance

In the United States, nearly 80,000 new primary central nervous system (CNS) tumors are diagnosed each year with one-half being malignant [1, 2]. The majority of diagnosed malignant brain tumors are gliomas with glioblastoma being the most common and aggressive form. Due to the high frequency of glioblastoma, finding new therapeutics and diagnostics for gliomas is a priority and improvements in drug development and measurement of tumor response to therapy may allow advancement of these efforts for other types of brain tumors [3]. The current standard of care for newly diagnosed glioblastoma patients involves maximum safe surgical resection, followed by radiotherapy plus concomitant and adjuvant temozolomide [4]. Given the difficulties with identifying precise tumor borders for resection and few therapeutic options, a joint meeting was held in 2014 among the Food and Drug Administration (FDA), National Cancer Institute (NCI), clinical scientists, imaging experts, clinical trials cooperative groups, representatives from pharmaceutical and biotechnology companies, and patient advocate groups to discuss new avenues for research in glioblastoma [summarized in [3]]. It was concluded that there is a “need to optimize the use of imaging as a surrogate

tool to better understand the response to novel therapeutics and the development of a set of priorities and action standardization of the MRI protocol for multicenter studies". Thus, there is a significant need in improving the ability to assess the impact of therapies in neuro-oncology.

Contrast agents for magnetic resonance imaging (MRI) containing para-magnetic ions such as gadolinium (Gd) are often used to improve the contrast between tissues, thereby providing a more accurate diagnosis of a desirable region [5]. Several contrast agents (Magnevist®, Gadovist®, Omniscan®) are currently used which cannot easily penetrate an intact blood–brain barrier (BBB) unless it is disrupted [6, 7]. In addition, these contrast agents are rapidly eliminated from the blood pool due to their low molecular weight. Moreover, they can extravasate from the vasculature into surrounding tissues accumulation in a tumor due to the enhanced permeability and retention (EPR) effect [8] several strategies have been employed to increase specificity and retention time [8] but still the complete cure of gliomas is extremely challenging. Further, combining the ability to detect glioma borders with the ability to kill the cancer cells in one image-guided theranostic has been an emerging, leading to poor contrast of a tumor compared with healthy tissues. To increase circulation time of contrast agents and their focus of research [9-11].

I.2 Innovation

Approximately 150 drugs are in development for cancer treatment based on nanotechnology [12]. The potentials of nano-formulations include drug solubility,

extended retention time and stability in the body, selective targeting, and reduced side effects while delivering treatments that are more potent [13]. Another advantage is the facilitation of drug delivery across biological barriers, such as BBB which limits access to brain tumors [14]. Additionally, nano-based formulations can also facilitate a combination of diagnostics with therapeutics (theranostics) for cancer [14].

Recent scientific reports underlined that lactoferrin (Lf) protein aids transcytosis across the BBB [15] and transferrin receptor (TfR) to be expressed on glioma cells and glioma stem cells [16]. On the other hand unlike other contrast agents such as Gd-DTPA [17], the fullerene cage in $Gd_3N@C_{80}$ is extraordinarily stable species which avoids a free Gd release. In addition, $Gd_3N@C_{80}$ has 25-fold more relaxivity compared to traditional Gd contrast agents due to the 3 Gd atoms inside the fullerene cage [18] and no overt toxicological endpoints have been observed in several studies with the $Gd_3N@C_{80}$ [18, 19].

Therefore, the innovative formulations herein are < 100 nm, PEGylated, Tf & Lf tagged (dual targeting), doxorubicin (DXR) and $Gd_3N@C_{80}$ loaded theranostics. The theranostics are characterized and their effectiveness is tested in-vitro on U251-MG cells. Furthermore, the stability and dynamics of $Gd_3N@C_{80}$ containing lipid bilayers in physiological salts solutions and at human body temperature are evaluated using molecular dynamic simulations.

I.3 Approach

The overall goal of this dissertation is to develop a glioblastoma nanotheranostic having enhanced tumor targeting, imaging, and cancer killing capabilities. To this end liposomal cancer theranostics are reviewed and possible targets are identified. Then dual and single targeted theranostics are developed and their cellular uptake by glioblastoma cells examined in vitro. Finally, the stability of these theranostics is evaluated by studying the structural stability of C_{80} or $C_{80}(OH)_{42}$ loaded lipid bilayers solvated in physiological salt solutions by using NAMD molecular dynamics simulations. The specific aims, the rationales and the strategies to realize the overall goal are explained below:

I.3.1 AIM 1: Review cancer theranostic liposomes and explore potential glioblastoma biomarkers

Rationale: To develop a new effective theranostic liposome, it is necessary to assess the state of the art of liposome based cancer theranostics and study the limitations of existing formulations. Furthermore, receptors useful for the transcytosis process across the BBB and potential glioblastoma biomarkers should be explored.

Strategy: liposomes based cancer theranostics are categorically reviewed with more emphasis on the formulation mechanisms, single/dual targeted and non-targeted theranostic liposomes and their application in cancer treatments. Potential glioblastoma biomarkers are identified through literature review and by enquiring different databases that are freely available for public use.

I.3.2 AIM 2: Synthesize, characterize and test glioblastoma-targeting theranostics

Rationale: While IL-13 receptors appear to be uniquely upregulated to high levels of glioblastoma cells there is concern about non-glioblastoma cell binding of IL-13 receptors (e.g. immune cells). Therefore, it is necessary to develop and test new dual/single ligand theranostic liposomes while keeping the diagnostic ($Gd_3N@C_{80}$) and therapeutic (DXR) components the same.

Strategy: Although several potential targets have been identified through the strategy mentioned in aim 1, it was necessary to test those with promising results in clinical trials. Phase I and Phase II clinical trial results demonstrated that the transferrin receptor as a viable target for tumor reductions in patients with glioblastoma [20, 21]. Lactoferrin was also reported to be a viable ligand to cross the BBB. Hence these two targets, transferrin & lactoferrin, were considered for the dual targeting process.

Theranostic development: Functionalized and non-functionalized $Gd_3N@C_{80}$ containing PEGylated liposomes are developed by a thin lipid film hydration process. DXR was remotely loaded into the liposomes using a PH gradient. The liposomes were tagged with transferrin and lactoferrin using amine-amine or amine-carboxylic conjugation processes. Encapsulation efficiencies are computed using standard curves and the particles are characterized using zetasizer, nanosight, Fourier-transform Infrared Spectroscopy (FTIR) and Ultraviolet-Visible Spectrophotometry (UV-VIS) analysis.

Theranostic testing: The ability of each theranostic to bind or endocytosed, and kill glioma tumor cells must be demonstrated in vitro. The hypothesis is that the theranostics modified with transferrin & lactoferrin will have better BBB crossing

capability, be up taken by glioblastoma cells, and kill glioma tumor cells. To this end the expressions of targets were assessed using western blotting and PCR. To compare the cytotoxic effect of these dual and single targeted theranostics, a microscopic examination of U251-Mg cells was carried out after the cells are treated for 24 & 72 hours. The enhanced cytotoxic effect of these theranostics was further confirmed by MTT assay.

I.3.3 AIM 3: Study the stability of these theranostics using molecular dynamic simulations

Rationale: The stability of $Gd_3N@C_{80}$ containing liposomes and the interaction of the fullerene cages with the lipid bilayer components must be evaluated in different physiological salt solutions and at human body temperature. The hypothesis is that; OH-functionalized or non- functionalized $Gd_3N@C_{80}$ will never affect the structural stability of the lipid bilayer compartment of those liposomes in physiological salt solutions.

Strategy: A complete structural stability study using experiments requires several equipment and expensive chemicals. Therefore, the strategy was to study structural properties using molecular dynamics simulations and compare the results with experimental reports in the literature. As Gd_3N in $Gd_3N@C_{80}$ is firmly confined within the fullerene cage, the molecular dynamics simulations focus on the external compartments (C_{80} and $C_{80}(OH)_{42}$). To this end the structural variations of C_{80} or $C_{80}(OH)_{42}$ (C_{80}/$C_{80}(OH)_{42}$) loaded versus C_{80}/$C_{80}(OH)_{42}$ free lipid bilayers immersed in different physiological salt solutions are evaluated. The dynamics of functionalized and non-functionalized fullerenes across the lipid bilayers are also evaluated using steered

molecular dynamic simulations. And the results are discussed in terms of the stability of the molecules inside the lipid bilayers and in terms of the interactions of the molecules with the lipid bilayers.

CHAPTER II

UPDATE ON LIPOSOME-BASED CANCER THERANOSTIC AND GLIOBLASTOMA BIOMARKERS

II.1 Abstract

Glioblastoma is the deadliest brain tumor where the average survival of a newly diagnosed case is less than 15 months. While new diagnostic and therapeutic approaches continue to emerge there has still been little progress in reducing the mortality associated with the disease. Liposome-based theranostics, which combine diagnostic and therapeutic capabilities, are one strategy being investigated for glioblastoma treatment. Here, current theranostic liposomes for cancer treatments are reviewed along with challenges associated with their development and use. This review highlights potential biomarkers, mined from different databases, as targets for optimum glioblastoma theranostic delivery. These biomarkers can be targeted to improve the delivery of imaging agents and cytotoxic or cytostatic drugs through ligand-receptor mediated endocytosis, antibody (fragment) based delivery, peptide based delivery, or other mechanisms such as a recombinant immunotherapy modality.

II.2 Introduction

The integration of diagnosis and therapy into a single nanoparticle has led to the birth of a field named ‘nanotheranostics’ which has given hope to developing innovative research to diagnose, treat, and follow up patients with various forms of cancer [22]. The rationale for using nano-size based molecules for developing nanotheranostics includes their small size to potentially overcome challenges with crossing the BBB, ability to be targeted to cancer-specific biomarkers, and the proven multimodal capabilities of designing nano-sized structures which serve different functions. However, it is still challenging to incorporate multiple components, having different purposes, on a single nano scale theranostic that is entirely adequate for combined diagnostics and therapy.

Several noninvasive imaging methods are currently being used for glioblastoma diagnostics. These include magnetic resonance (MR), computed tomography (CT), ultrasonic (US) and positron emission tomography (PET) imaging techniques. These can simultaneously be integrated with therapeutic strategies, such as chemotherapy, gene therapy, photodynamic therapy (PDT), and photo thermal therapy (PTT) to monitor the bio distribution, drug release kinetics and therapeutic efficacy [23]. Nanomaterials are an attractive platform for developing such theranostics [24, 25].

Liposome can be an important component of theranostics. There have been growing numbers of trials and approvals of liposome-based delivery systems. Several liposome-based therapeutics and diagnostics, including those approved by the FDA, are now used in the clinic, in clinical trials, or in pre-clinical developments [26-28]. The most

recently approved liposomal drug carrier Onivyde® (liposomal irinotecan), a topoisomerase I inhibitor is used as a second line treatment for metastatic pancreatic cancer [27]. Nevertheless, there is no FDA approved theranostic liposome, and there is no FDA approved targeted liposome for glioblastoma treatment. Given the wide acceptance, safety, and effectiveness of liposomes as a platform for developing new diagnostics, therapeutic, and nanotheranostics, all the efforts to develop new nanotheranostics using liposomes are discussed, in this chapter, with a focus on specific glioblastoma targets.

II.3 The Potential of Theranostic Liposomes and Formulation Strategies

The advantage of liposome-based nanotheranostics is twofold. First combining multiple imaging modalities and therapeutic functions in one complex is possible by exploiting the inner core, the double layer or by attaching imaging or therapeutic agents from outside after functionalizing the phospholipids. Second, liposomes are flexible, biocompatible, biodegradable and are suitable for conjugation with ligands or antibodies [29]. Liposomes can also easily fuse with target cancer cells on the surface, which facilitates the transport of drugs across biomembranes.

The formulation of liposomes for drug delivery was started with non-targeted liposomes in the 1960s [30-32] and has evolved over time to those incorporating nanoparticle, PEGylating and targeting moieties [31, 33]. Liposomes are also being designed to release their payload as a result of external stimuli such as heat [34], light [35], magnet [36], ultrasound or internal stimuli including enzymes, redox or PH sensitive [37]. Liposomes are exploited for cancer drug delivery, reaching up to phase IV

in a clinical trial (example LIPUSU® for Metastatic breast cancer) and some are already FDA approved for cancer treatment (example MyocetTM also for Metastatic breast cancer) [38]. DOXIL® was clinically approved for the treatment of Kaposi's sarcoma and ovarian breast cancers and recently Marqibo® was approved for Lymphoblastic leukemia [31, 32]. Hence the following sections focus on theranostic liposomes, in cancer studies, utilizing quantum dots (QDs), metals, and radionuclides.

II.3.1 QDs-encapsulated theranostic liposomes

Many studies have attempted to develop QD-based theranostic liposomes for cancer treatment by integrating the fluorescence properties of QD with therapeutic drugs (Table 1). QDs together with magnetic, paramagnetic or radioactive particles were engineered for more sensitive and quantitative diagnostic applications [22]. Liposome-QD hybrid vehicles were also developed by incorporating trioctylphosphine oxide (TOPO) capped, CdSe/ZnS QD into the lipid bilayers containing DSPC, cholesterol, and DSPE-PEG2000 followed by loading anticancer drug DXR into the aqueous core, remotely, by a PH gradient [39].

Novel drug delivery monitoring systems can also be designed using QDs by associating the fluorescence intensity of the QDs to drug concentration [40]. Liposomal formulations having QD in the lipid bilayer and camptothecin (CPT) or irinotecan inside the core compartment of cationic lipids were reported to indicate improved florescence, cytotoxicity and migration inhibition role in melanoma cells [41]. The intensity of fluorescence or localization of QDs inside cell compartments can be maximized by

loading QD-drug conjugates inside targeted liposomes. For example, D-alpha-tocopherol polyethylene glycol 1000 succinate mono-ester coated theranostic liposome containing docetaxel and QDs was developed for breast cancer [42]. In those formulations folate receptor targeted liposomes showed significantly higher cellular uptake compared to non-targeted liposomes [42].

More recently, a tumor-targeted lipid nanocarrier for gene delivery and tumor bio-imaging using QD was developed by coupling an aptamer to the epidermal growth factor (EGF) receptor and was found to be effective tumor targeting [43]. QDs and Topotecan (TOPO) containing liposomes were formulated using a thin lipid film hydration followed by a pH-gradient based drug loading process. In these formulations, liposomal TOPO showed significantly higher cellular uptake and cytotoxicity compared to free TOPO when tested in HeLa and A549 cells [44]. Other theranostic liposomes incorporating QDs and apomorphine reported in [45] avoided liver uptake and enhanced brain targeting as confirmed by a hyperspectral analysis of QDs localization [45].

II.3.2 Gadolinium (Gd)-encapsulated theranostic liposomes

Approximately 40% of magnetic resonance imaging (MRI) examined cancer patients receive Gd-based contrast agents which has proven to improve cancer detection and diagnosis [46-48]. One of the limitations of using free Gd as a contrast agent is the possibility of developing nephrogenic systemic fibrosis (NSF), especially in renal impaired patients resulting from free Gd deposition in tissues [48]. Nonetheless, several theranostics have been reported in the literatures that incorporate Gd as the imaging

component (Table 1). The αvβ3 integrin targeting peptide c(RGDyk) has been used to tag Gd-DOTA and paclitaxel (PTX)-containing liposomes for drug delivery to A549 tumor cells and shown a 16-fold increase in T1 relaxivity compared to non-targeted groups [49]. Similarly, neural cell adhesion molecule-targeted binding peptide coated liposomes loaded with both DXR and a lipophilic Gd derivative were generated that induced an enhanced *in vitro* DXR internalization within Kaposi's cells compared to untargeted liposomes [50]. These targeted, Gd-labeled liposomes allowed the concomitant MRI visualization of the drug delivery in the tumor region [50]. Another which integrates mesoporous silica nanoparticle (MSNs) with Gd and tagged with a pro-apoptotic peptide KLA provided better biocompatibility, exhibited cellular uptake, and induces mitochondrial swelling and apoptosis in MCF-7 cells [51]. A theranostic liposome which integrates magnetic resonance (MR), near-infrared (NIR) fluorescence, nuclear imaging and DXR was reported in [52]. These liposomes were first formulated by incorporating DSPC, cholesterol, Gd-DOTADSPE, DOTA-DSP and by hydrating with ammonium sulfate solution. Then a lipidized NIR fluorescent detector, IRDye-DSPE, was post-inserted into the pre-manufactured liposomes. Finally, DXR was loaded remotely and the resulting liposomal formulation was radiolabeled with ^{99m}Tc or ^{64}Cu for single photon emission computed tomography (SPECT) or positron emission tomography imaging respectively (PET) [52]. Intratumoral injection of these theranostics in rats with squamous cell carcinoma of head and neck tumor xenografts, and subsequent imaging using MR, NIR, SPECT and PET displayed a promising result.

Attempts to minimize issues associated with free Gd toxicity, one strategy was to incorporate the Gd within carbon spheres such as $Gd_3N@C_{80}$ [18]. A glioblastoma-targeting theranostic (GTTN) liposome containing DXR and $Gd_3N@C_{80}$ targeted with IL-13 induced cell death in IL-13 receptor expressing U-87 cells *in vitro*, and shrink human brain tumors transplanted in mice compared to non-targeted [53].

Another strategy uses temperature or ultrasonic change within the tumor to utilize the therapeutic and diagnostic components of a theranostic. A thermosensitive liposome demonstrated enhanced DXR release and contrast upon heating to 40-42 °C and the process completely regressed EMT-6 tumor model in mice [54]. Similarly, a theranostic liposome developed using temperature sensitive copolymer, a dendron lipid attached to a Gd-chelate and DXR suppressed tumor growth after intravenous injection in tumor bearing mice [55]. Liposome drug release can also be controlled by ultrasound. For example, ultrasound-triggered release of DXR in Gd-containing liposomes was reported to increase drug accumulation in the intratumor environment, enhanced TI contrast, and caused a complete regression of adenocarcinoma [56]. Another generates MRI contrast when the liposomes are triggered by local exposure to ultrasound with concomitant release of DXR [57].

To sum up, there is a tremendous progress in the development of Gd containing theranostic liposomes and these efforts have promising future for cancer treatments. However, the contrast agents must be loaded inside stable and targeted liposome structures or has to be loaded into targeted liposomes in the form of stable Gd-chelates to avoid possible Gd dissociation.

II.3.3 Iron oxide-encapsulated theranostic liposomes

Superparamagnetic iron oxide nanoparticles (SPIONs) based T2 MRI contrast agents may be another alternative for patients at risk for Gd-induced NSF [58, 59]. A hybrid liposome containing amphiphilic hyaluronic acid hexadecylamine polymer (HA-C16) as a targeting ligand, dipalmitoyl-sn-glycero-3-phosphocholine (DPPC), cholesterol, SPION, and docetaxel (DTX), was examined for delivery to human breast cancer cells overexpressing CD44 receptors (Table 1) [60]. In this formulation, citric acid-coated SPIONs were embedded in the aqueous cores while DTX was encapsulated in the hydrophobic bilayer. Confocal as well as flow cytometry experiments indicated superior cellular uptake of HA-C16 tagged liposomes compared to non-targeting liposomes [60]. Similarly, liposomes loaded with a Gonadorelin-functionalized SPION and mitoxantrone (MXT) showed a significantly increased uptake by MCF-7 breast cancer cells overexpressing the luteinizing hormone releasing hormone (LHRH) receptor compared to the uptake of non-targeted liposomes [61]. A liposome-type formulation comprising iron oxide core, DXR containing polymer (dextran) coated with acetylated lipids and PEG demonstrated deep imaging capability [62]. Therefore, combining SPIONs with therapeutic drugs may overcome the limitations observed in Gd-based constructs when administered to glioma patients with a previous NSF history.

II.3.4 Radionuclide-liposome theranostics

Radiolabeled liposome theranostics are also being used for disease diagnosis and treatment of cancers [63, 64]. Rhenium (^{186}Re) is an attractive radionuclide for imaging

and tumor therapy due to its 3.78 days half-life, with 137 keV gamma emission for scintigraphic imaging and 1.07 MeV β emission with a tissue penetration depth range of 2-4 mm [65]. DXR containing liposome labelled with ^{186}Re for use in SPECT based imaging and chemotherapy demonstrated good bioavailability, tumor targeting and localization in a head and neck cancer xenograft model in rats [65]. A similar construct radiolabeled with Technetium (^{99m}Tc) was used to monitor the localization of liposomal drug in rats [66]. Other radionuclides such as Iodine ^{123}I/^{131}I have been employed for diagnosis and radionuclide based therapy of thyroid cancers [67]. Some of the challenges in using radionuclides for therapy is their short half-life, limited depth of penetration, and lower decay energy of the nuclides in a biological system. Conversely, if the energy of the emitted radiation is very high, it may cause a damaging effect on surrounding normal cells. Therefore, it is necessary to determine an optimum energy range radionuclide when developing theranostic liposomes with radionuclides.

II.3.5 Other metals-encapsulated theranostic liposomes

Other metals used as imaging agents include gold, silver and manganese which can be enclosed in the aqueous compartment, loaded in the liposome lipid bilayer or attached to the outer part of the liposomes (Table 1). Recently a bubble-generating nanoparticle incorporating ammonium bicarbonate and gold nano-rods in folic acid-conjugated liposomes was designed and proven to be effective for a multimodal imaging and DXR release using a hyperthermia when tested in S180 tumor-bearing mice [68]. Similarly, a thermosensitive hybrid system incorporating gold, silver, and iron oxide

nanoparticles in the lipid bilayers loaded with DXR was reported in [69] and demonstrated an improved DXR release due to external heating. Furthermore a low temperature-sensitive liposomal theranostic incorporating $MnSO_4$ and DXR was formulated and tested for drug release efficiency on rat fibrosarcoma tumor cells using MRI [70]. Interestingly, the relaxivity of the Mn^{2+} inside the temperature sensitive liposomes was above free Mn^{2+} hypothesized to be due to a partial binding of Mn^{2+} with the phospholipid head groups which increases its interaction with water by reducing the Brownian motion of free Mn^{2+} [70].

Table 1. Summary of Liposome-based Cancer Theranostics Categorized with Imaging Agents. Most lipid abbreviations accord the nomenclature in [71], otherwise explained in the references provided

.

Imaging agent	Drug	Disease (cell line)	Lipid composition	target (ligand)	Reference
QD	CPT	Melanoma	SPC, Chol, DSPE-PEG		[41]
QD	DTX	MCF-7	DPPC, Chol, TPGS, DSPE-mPEG-FA	Folic acid	[42]
QD	TOPO	Hela, A549	DSPC, Chol		[44]
QD	Apomorphine	bEND3	PC, Chol, SA, DSPE-MPEG		[45]
QD	SiRNA	MDA-MB-231	DMKE, Chol, DSPEM-PEG2000	Anti EGFR aptamer	[43]
$Gd_3N@C_{80}$	DXR	GBM	DPPtdCho, Chol, DSPE-PEG	IL-13, IL13R2	[53]
Gd-DOTA	Paclitaxel	A549	DSPC, DSPG, MPEG-2000-DSPE	Peptide ($\alpha_V\beta_3$ targeting)	[49]
Gd-DOTA	DXR	Head and neck	DSPC, DSPE, Chol		[52]
Gd-DTPA	DXR	EMT-6 cells	DPPC/Brij78		[54]
GdDOTAMA(C18)	DXR	TS/A	DPPC/DSPC/Chol/DSPE-		[56]
Gd-DOTAMA(C18)2	DXR	Kaposi's cells	POPC/DSPE-PEG-PDP/DSPE-PEG	NCAM-targeting Peptide	[50]

GD-DOTA	DXR	Colon carcinoma 26	EGGPC, Chol, PEG-PE		[55]
Gadoteridol [Gd(HPDO3A) (H2O)]	DXR	Breast-TS/A	DPPC/DSPC/Chol/DSPE-PEG2000		[57]
Gd (MSNs)	KLA peptide	MCF-7	DPPC, DSPE-PEG2000, Chol		[51]
SPIONs	DTX	Breast	DPPC, Chol	HA-C16	[60]
SPIONs	MXT	Breast	HSPC, Chol, and PEG2000-	Gonadorelin(peptide)	[61]
SPIONs	DXR	Lung/pancreatic	DOPE, DSPC-PEG2000, Chol,		[62]
^{99m}Tc	DXR		Lipids used to formulate DOXIL®		[66]
^{136}Re Radionuclide	DXR		Lipids used to formulate DOXIL®		[65]
Indocyanine green (Photoacustic)	DXR	Breast	HSPC, DSPE-PEG2000, Chol	MUC-1	[72]
Gold	DXR	MCF-7	Lecithin, Chol, DSPE-PEG_{2000}	Folic acid	[68]
Gold, silver, SPIONs	DXR		DPPC, MSPC, DSPE-PEG_{2000}		[69]

II.4 Glioblastoma Targets

Several stategies to overcome the BBB are reported in the litrature among which receptor mediated delivery is a matured and better option [73, 74]. Several glioblastoma-specific targets are also reported [75-78] (Table 2). However, it is critically important that any moiety targeted on cancer cells does not result in activation of the cells. Here, a synopsis of glioblastoima targets are provided that could be examined in the context of their potential in developing glioblastoma-specific theranostics.

Table 2. List of Receptors that are often used for Targeted Drug Delivery in Glioblastoma Treatments

Receptor	Role in glioblastoma	Related references
Ephrin type-A receptor 2 (EphA2)	Proliferation	[79, 80]
Urokinase plasminogen activator receptor (uPAR)	Proliferation/activation	[81, 82]
Transferrin receptor (TfR)		[83]
Epidermal growth factor receptor (EGFR/ERBB1)	Proliferation	[84, 85]
Epidermal growth factor receptor variant III (EGFRVIII)	Proliferation/angiogenesis	[86, 87]
Interleukin receptor 4 (IL-4Ra)		[88]
Interleukin receptor 13 (IL-13Ra2)		[89]
Fibroblast growth factor-inducible 14 (Fn14) receptor		[90, 91]
Vascular endothelial growth factor 2 (VEGFR2)	Proliferation/angiogenesis	[85, 92]
Receptor tyrosine kinase 2 (Erb-b2/HER2)		[93]

Anaplastic lymphoma receptor tyrosine kinase (ALK)		[94]
Transforming growth factor, beta receptor II (TGFBR2)		[95]
C-X-C motif chemokine receptor 4 (CXCR4)		[96]
Met proto-oncogene (MET)	Proliferation	[97, 98]
MER proto-oncogene, tyrosine kinase (MerTK)		[99]

II.4.1 Determination of potential glioblastoma targets

The overall strategy for exploring new potential glioma targets is depicted in (Figure 1). Receptor genes common in the Human Protein Atlas version 16.1, Ensemble 83.38 (focusing on glioma) [100-102] and receptor-ligand binding information from UCLA database of interacting proteins [103] were mined using Visual Basic Application code. The glioma data from the Human Protein Atlas incorporates immunohistochemistry data from tissue microarrays of glioma tumor patients to provide expression scores based on: 1) staining intensity (negative, weak, moderate or strong) and 2) fraction of stained cells (rare, <25%, 25-75% or >75%) scored as “not detected”, “low”, “medium” and “high” [104]. Such expression level data integrated with protein-ligand interaction data provide valuable information on receptor’s role in cancer cell migration or invasion. Common receptors/genes with “high” and a “medium” scores were further evaluated for their expression level on different glioblastoma classes by querying open access databases such as the Repository for Molecular Brain Neoplasia Data (REMBERANDT) [105] and The Cancer Genome Atlas (TCGA [106]).

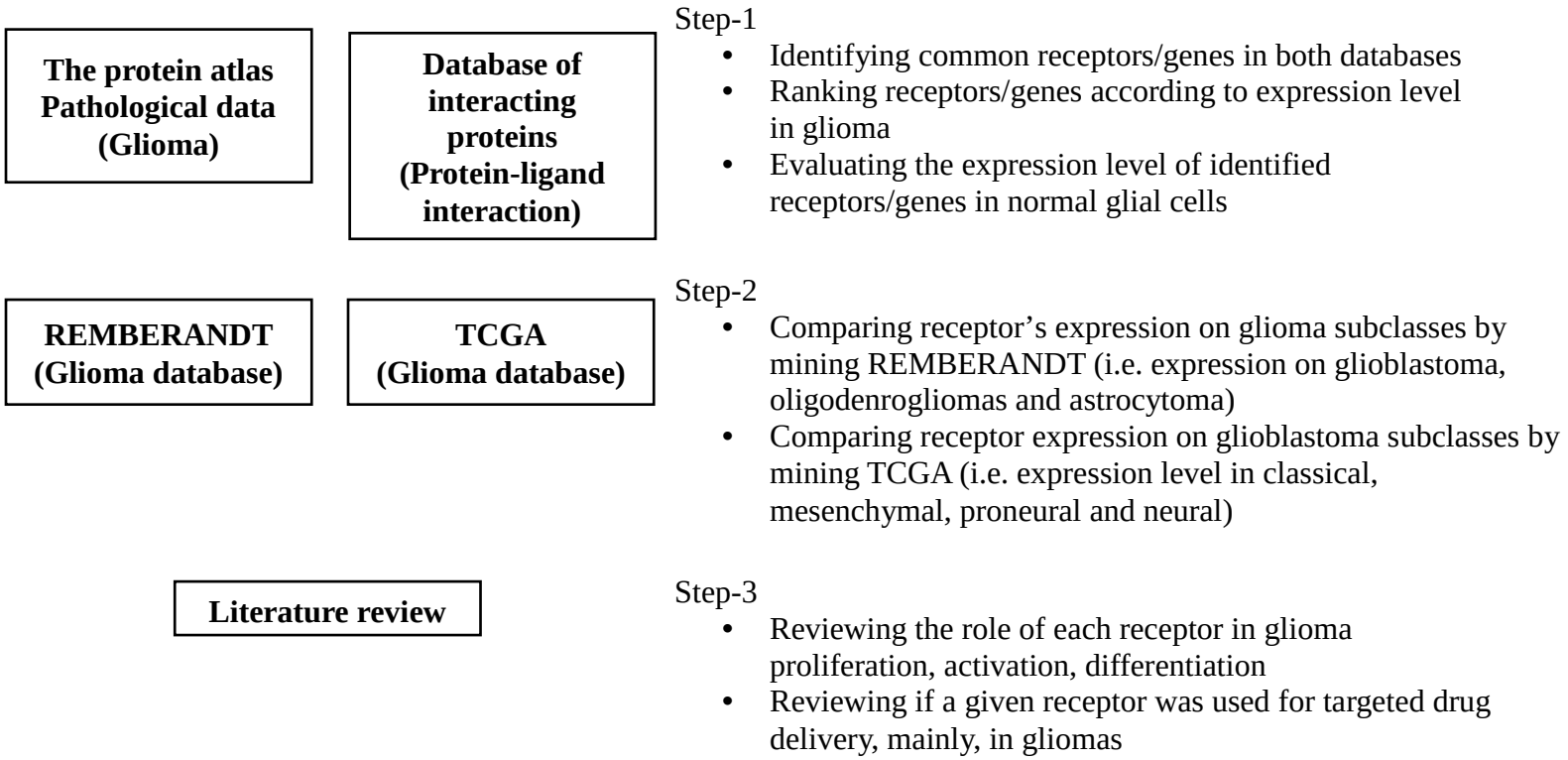

Figure 1. Potential Biomarkers (targets) Data Mining Strategy from Freely Available Databases Open for Public use. Receptor proteins/genes overly expressed in glioblastoma patients available in the protein atlas and database of interacting proteins [104] were selected by filtering common receptors, expression level, and by comparing these data with expression of the same receptors in normal glial cells. The expression of resulting receptors were further analyzed with respect to glioblastoma subtypes by querying the REMBRANDT and TCGA glioma data through project Betastasis [106]. As relying on databases alone may not be sufficient, literature was consulted to study the role of the receptors in glioma migration, proliferation, differentiation etc.

II.4.2 Receptor expression and their role in glioma

Following the data mining strategy explained in section 3.1, the total number of patients positive for a specific receptor (i.e. including less, moderate or higher expression levels) and those moderately and highly expressed (excluding those with lower expression) are indicated in Figure 2. The expression levels of those receptors in glioblastoma subclasses and normal glial cells was further assessed and presented in Table 3. As an example, protein tyrosine phosphatase, receptor-type, Z polypeptide 1 (PTPRZ1) is highly expressed in glioblastoma, oligodenderoglioma and astrocytoma [104]. Further, it is expressed in all classes of glioblastoma with more on classical and proneural subclasses (Table 3). Inhibiting PTPRZ inhibits glioblastoma cell proliferation and migration [107] and decreased the sphere forming abilities of C6 and U251-MG cancer cell lines [107] making it a potential target for theranostic delivery.

The protein tyrosine phosphatase receptor type B (PTPRB; Figure 2) is also highly expressed in glioblastoma but its role in cell inhibition or activation is not clear. While mutations in PTPRB increased angiogenesis in angiosarcoma [108], normal PTPRB overexpression didn't lead tumor aggression rather inhibits VEGFR2, VE-cadherin, and angiopoietin signalling, reduces cell proliferation and has general anti-cancer cell properties [108, 109]. Other studies suggest the receptor's interaction with its ligand pleiotrophin (PTN) may induce glioma migration [110]. The neurotrophic tyrosine kinase receptor type 2 (NTRK2) is highly expressed on gliomas making it a novel biomarker for glioma targeting [111, 112]. Further, chemokine receptor 2 (CCR2) is also

highly expressed on glioblastoma cells compared to normal glial cells [113]. CCR2 is involved in chemokine signalling and appears to play a dual role in mediating early tumor immunosurveillance and sustaining the growth and progression of established neoplasms and has been used as a way to inhibit glioma cell migration [113, 114].

Oncostatin M receptor (OSMR) is expressed relatively higher on mesenchymal sub-classes of glioblastoma and knocking-down of OSMR suppresses proliferation and tumor growth in mouse glioblastoma cells as well as in human brain tumor stem cell-xenografts in mice [115]. Furthermore, OSM-OSMR mediated signaling via signal transducer and activator of transcription 3 (STAT3) drives glioma cells towards a mesenchymal type making it an attractive target for glioblastoma targeting [116]. Activin A receptor type 1 (ACVR1) is another potential target which is expressed relatively higher on mesenchymal subclasses in glioblastoma. It was reported that ACVR1 mutations and aberrant bone morphogenetic protein (BMP) signaling as a new potential therapeutic target in pediatric diffuse glioma [117]. Epidermal growth factor receptor (EGFR) highly expressed in GBM is widely used as a target in glioblastoma treatments [118]. Platelet-derived growth factors A & B (PDGFRB and PDGFRA) are also potential targets for glioma treatments where targeting PDGFRB with a multi kinase inhibitor drug (imatinib) caused effective killing of glioma stem cells [119]. PDGFRB silencing also increased radio sensitivity of C6 glioma cells [120]. Other GBM targets for inhibition include P75 neurotrophin receptor [121], transforming growth factor beta receptor 1 [122], chemokine receptor 9 [123], tumor necrosis factor receptor superfamily members (e.g. TNFRSF11A) [124], bone morphogenetic protein receptor type IA [125], colony

stimulating factor 1 receptor [126] and the Leukemia inhibitory factor receptor alpha. IL13RA2 receptor is a promising target for glioblastoma treatment for a targeted fusion protein (IL13-PE38QQR; Cintredekin Besudotox), composed of human IL-13 and a truncated, mutated version of pseudomonas exotoxin (PE) is in phase III clinical trails [127-129].

Table 3. Potential Targets for Theranostic Delivery in Gliomas. The number of patients stained positive with respect to the total number of patients (column 2) and expression on normal cerebral cortex (column 3) are from The Protein Atlas and expression on glioblastoma subtypes (Column 4) is from TCGA. Expression on glioma subtypes (column 5) is from REMBERANDT. Abbreviations are: GBM- glioblastoma, ODGM -oligodendroglioma and ACM - astrocytoma.

Protein/gene [130]	# of patients [100]	Normal cerebral cortex expression [100]	Sub-class expression: (TCGA)[106] N-neural C-classical M-mesenchymal P-proneural	Sub-class expression: REMBRANDT[105, 106] GBM ODGM ACM	Involvement in proliferation, migration [131]	Cancer/ Glioma Related study
CCR9	11/11	none	N, C, M, P	A>C>B		[132, 133]
TNFRSF11A	11/12	none		A, C, B		[134]
MET	11/11	none		A, C, B		[85, 97]
CSF1R	11/12	none	M, P, N, C	A, C, B		[135, 136]
PDGFRB	9/11	none	M	A> C, B	proliferation, migration	
IFNAR1	8/10	none	M, N	A>B, C		[137]
NGFR	7/12	none	P	A>B, C		
EGFR	7/12	none	C	A>B, C	proliferation	
CCR2	5/12	none				[138]
INSR	10/12	low		B>C, A		[139]
TNFRSF1B	9/10	low	M, N	A>B, C		

OSMR	8/12	low	M, C	A>C, B	proliferation	[140]
ERBB3	7/11	low				
ACVR1	6/12	low	M, N	C>A>B		[141, 142]
NRP1	6/10	low	M, C	A>B>C	proliferation	[143]
BMPR1B	6/12	low	N	C>B, A		[144]
LIFR	12/12	medium-low	C	C>B, A	proliferation	
PTPRZ1	11/11	medium-low	C, P, M, N	C, A, B		[145, 146]
IGF2R	10/12	medium-low	M, P, C, N	A>C>B		
IL11RA	10/11	medium			proliferation	

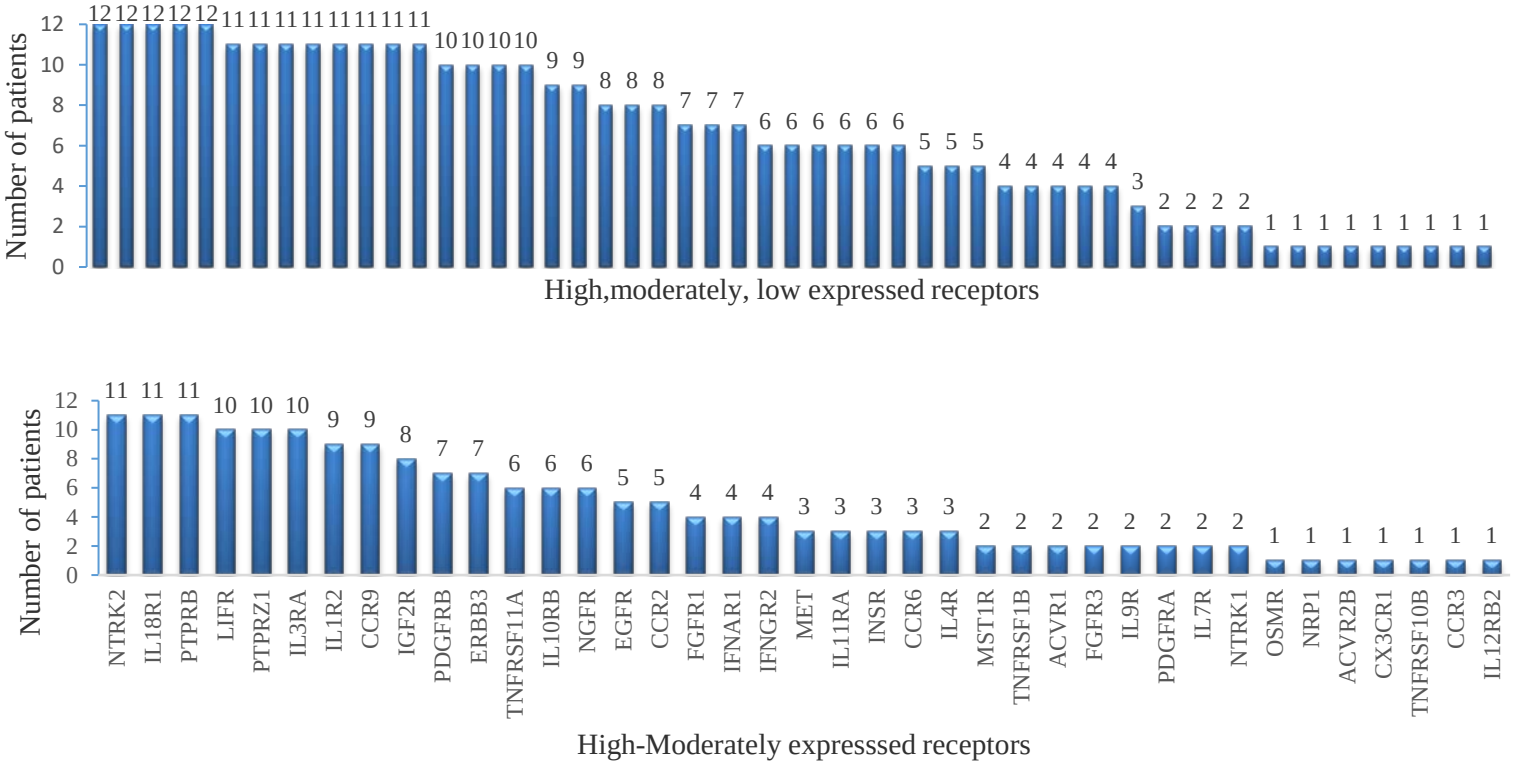

Figure 2. The Expression of Potential Targets in Glioma Patients Extracted using a VBA Code which searches for Commonly Expressed Proteins in the Human Pathology Atlas [104] and Database of Interacting Proteins [106]. A) The numbers on the top of each bar indicate the number of patients positive for a particlular receptor (includes high, moderate and low expression). B) Potential targets that are highly and moderately expressed.

II.5 Summary

To date there is no FDA approved targeted theranostic liposome for glioblastoma treatment. Any strategy for identifying suitable targeting ligands for glioblastoma must consider relative expression of the target on glioblastoma cells compared to healthy cells, whether the receptor/target activates or inhibits cells growth, and the ability to effectively develop and incorporate the targeting ligand on the surface of the theranostic. Combinatorial targeting of more than one glioblastoma marker such as those outlined in (Table *2* & Table 3) may enhance tumor specific killing while reducing unwanted binding to healthy cells and/or enhancing the ability of the theranostic to cross the blood-brain barrier. In addition, the resulting theranostic must be able to cross the blood-brain barrier without degradation, specifically target the tumor cells, and remain functional after reaching the cell in its ability to enhance imaging for diagnosis while in parallel release cancer killing therapeutics.

CHAPTER III

DESIGN AND TESTING OF DUAL-TARGETED $GD_3N@C_{80}$ CONTAINING GLIOBLASTOMA THERANOSTICS

III.1 Abstract

The majority of the malignant brain tumors are gliomas with glioblastoma being the most common and aggressive type. Due to its extreme infiltrative nature and higher occurrence frequency, finding new glioblastoma therapeutics and diagnostics is a high priority. In line to this several mono-targeting glioblastoma theranostic liposomes are reported in the literature. Herein, a dual-targeted theranostic is synthesized on the hypothesis that targeting multiple receptors would enhance delivery precision. DXR and endo-fullerene ($Gd_3N@C_{80}$) were encapsulated within liposomes and conjugated with transferrin (Tf) and lactoferrin (Lf). The hydrodynamic size, zeta potential, encapsulation efficiency and tagging with proteins of the $Gd_3N@C_{80}$ and DXR loaded liposomes were characterized using dynamic light scattering (DLS), inductively coupled plasma mass spectrometer (ICP), Fourier-transform infrared spectroscopy (FTIR), and ultraviolet-visible spectrophotometry (UV-VIS) analysis. As verification of efficacy, the Tf & Lf dual-tagged theranostic liposomes were able to significantly induce cell death compared to Lf mono-tagged theranostics.

III.2 Introduction

Close to 80,000 new glioma cell-involved primary central nervous system (CNS) tumours are diagnosed each year in the United States with roughly half being malignant [1, 2]. The prognosis of patients with malignant gliomas remains extremely poor, with a median survival of less than 15 months [147]. Hence, finding new therapeutics and diagnostics for gliomas is a high priority and improvements in drug development, and measurement of tumor response to therapy may allow advancement of these efforts for other types of brain tumors [148].

Among all gliomas, GBM, a World Health Organization grade IV glioma, is the most common and lethal primary malignancy of the central nervous system [149]. Targeted deliveries of therapeutics in GBMs mainly rely on single biomarkers, and the chemotherapeutics suffer from lack of specificity causing significant healthy cells death. Another major obstacle for any GBM diagnostic or therapy is transporting it across the blood brain barrier (BBB).

Using Lf as a targeting ligand for GBM is attractive as it is able to cross the BBB and the transferrin receptor (TfRC) is expressed on glioma cells and glioma stem cells [150, 151]. Indeed, Lf has been extensively used for targeted delivery of several drugs to the brain [152, 153] and was used for a magnetic resonance imaging (MRI) agent delivery to the brain [154]. Furthermore, Phase I and Phase II clinical trial results demonstrated that the transferrin receptor as a viable target for tumor reductions in patients with GBM [155]. Similarly, Tf is considered a viable ligand for targeted delivery in gliomas [156, 157].

Tf as well as Lf are often used separately in crossing the BBB and targeting glioma cells [158]. However, it was previously reported that Tf or Lf tagged nanoparticles have some limitations. For instance, Tf tagged nanoparticles were reported to be deposited in major organs such as heart, kidney, spleen, lung etc.[159]. On the other hand, Lf tagged nanoparticles were reported to be identified by macrophages more easily compared to Tf tagged nanoparticles [159]. Lf tagged nanoparticles were found to get accumulated more in liver compared to Tf attached nanoparticles [159] and there are debating reports on the BBB crossing capabilities of Tf-tagged versus Lf tagged nanoparticles [159, 160]. These debates could be due to differences on the expression level of TfR & LfR on the BBB as well as in cancer cells which may vary from patient to patient. Hence the formulation herein is based on the premise that by modifying the theranostic liposomes with the two ligands, i.e. Tf & Lf, it is possible to minimize the drawbacks observed in using the single ligands. The basis is that the dual modified thernostics will be less identified compared to Lf-tagged particles by macrophages, will have lower effect on TfR expressing major normal tissues, and will have the potential to cross the BBB through TfR, LfR and Tf & LfR depending on the level of expression of these receptors on a given glioma cell.

On top of efficiently targeting tumor cells, theranostics should incorporate excellent contrast agents. Water-soluble derivatives of gadolinium-containing metallofullerenes, $Gd_3N@C_{80}$, having 10.8 μ_B - 21 μ_B effective magnetic moment (μ_{eff}) values [161, 162] are excellent candidates for MRI. Further, magnetization curves of $Gd_3N@C_{80}$ at different temperatures shown no hysteresis indicating $Gd_3N@C_{80}$ as a

completely paramagnetic molecule [163]. These molecules are also characterized by higher r_1 relaxivity, mainly, when designed to be water soluble. For example, Hydrochalarone-6 functionalized $Gd_3N@C_{80}$ shown r_1 relaxivity of 205 mM^{-1} s^{-1} (68 mM^{-1} s^{-1} Gd, compared with 3.8 mM^{-1} s^{-1} for Magnevist [164]). $Gd@C_{82}(OH)_{40}$, with just one Gd^{+} was reported to have significantly higher r_1 relaxivity (67 $mM^{-1}s^{-1}$) than Gd-DTPA [165].

The purpose of this work was therefore to develop a new targeted theranostic that incorporates imaging and therapeutic entities within the same GBM-targeted molecule. A liposome-based carrier vehicle was used to incorporate the anti-cancer drug doxorubicin (DXR) and $Gd_3N@C80$ which was proven to provide excellent MRI contrast in different studies [53, 166, 167]. The liposome was then dual tagged with Tf and Lf and tested for efficacy in vitro. This strategy may provide a better way to diagnose and treat GBM.

III.3 Materials and Methods

III.3.1 Materials then reagents

Liposome components L-α-phosphatidylcholine (Egg, Chicken) (EGG-PC), 1,2-dipalmitoyl-sn-glycero-3-phosphoethanolamine-N- [methoxy (polyethylene glycol)-2000] (PEG200PE), 1,2-distearoyl-sn-glycero-3-phosphoethanolamine-N- [amino (polyethylene glycol)-2000] (DSPE-PEG (2000)-NH_2), 1,2-distearoyl-sn-glycero-3-phosphoethanolamine-N- [carboxy (polyethylene glycol)-2000] (DSPE-PEG (2000)-COOH) and Cholesterol were purchased from Avanti polar lipids. N-(3-Dimethylaminopropyl)-N′-ethylcarbodiimide hydrochloride (EDCI) and N-Hydroxysuccinimide (NHS) for protein-liposome conjugation, DXR-HCl (cancer drug),

Lf human and Tf for targeting liposomes were purchased from Sigma Aldrich. Dialysis cassettes at 2000 and 3500 Kd molecular weight cut-off to remove un-encapsulated materials; Vybrant® MTT Cell Proliferation Assay Kit for cell viability test and Novex™ 8% Tris-Glycine Mini Gels for western blotting were purchased from Thermo Fisher Scientific. Gadolinium (Gd), a standard for induced coupling plasma spectrometer measurements, was purchased from Fisher Scientific. $Gd_3N@C_{80}$-OH and $Gd_3N@C_{80}$ were purchased from Luna Innovations [53, 164]. The G1/221/12 mouse anti-human Tf receptor primary antibody was from Developmental Studies Hybridoma Bank. Rabbit anti-mouse secondary antibodies were from Thermo Fisher Scientific.

III.3.2 Cell culture, real time PCR (RT-PCR) and Western blots

U251-MG cells were grown in Eagle's Minimum Essential Medium (EMEM) supplemented with 2 mM Glutamine, 1% non-essential amino acids, 1 mM Sodium Pyruvate and 10 % fetal bovine serum (FBS). Cells were maintained at 37 °C in the presence of 6% CO_2.

The expression of targets in U251-MG cells were verified using PCR [168]. Briefly, total cellular RNA was isolated using the one-step RNeasy mini-kit (Qiagen, Valencia, CA) according to the manufacturer's procedure [169] and primers, sequences shown in Table 4, are generated using Primer-BLAST as described in [170]. PCR reactions were performed by setting a reverse-transcription reaction temperature of 50 °C (30 min) and an initial PCR activation temperature of 95 °C (15 min). The 3-step cycling

conditions were set to 94 °C (45 secs), 54 °C (30 secs) and 72 °C (1 min) for denaturing, annealing and extension respectively (30 cycles). Finally, products were run in 2% gel.

The expression of Tf receptor was verified using Western blotting as described [171]. Briefly, U251-MG lysates proteins were separated by SDS-PAGE, transferred onto nitrocellulose, and probed with 0.3 µg/ml mouse anti-human anti-transferrin receptor antibody. After washing HRP-conjugated rabbit anti-mouse antibody (0.4 µg/ml) was added for an hour, washed, and bands visualized using clarity Max™ Western ECL Blotting Substrate mixture on Amersham Imager 600 (Figure 3).

Table 4. Forward and Reverse Primers Sequences used for the Real Time Polymerase Chain Reactions. TfR-Transferrin receptor, DAG-Dystroglycan, EGFR-Epidermal growth factor receptor, FABP7-Fatty acid binding protein 7, Interleukin receptor subunit α 2, Lactoferrin and platelet derived growth factor receptor (PDGFR).

Protein	Forward & Reverse primer (FP & RP) sequence 5'->3'	Tm
TfR	FPAGGACGCGCTAGTGTTCTTCTG +	62.59
	RPCATCTACTTGCCGAGCCAGG -	60.53
DAG	FPCCCAGTACGTCAAGACCCTG+	59.75
	RPGCACACAGAGCATTAGAAGCC-	59.60
EGFR	FPTTGCCGCAAAGTGTGTAACG+	59.97
	RPCGATGGACGGGATCTTAGGC-	60.04
FABP7	FPAGAAACTGTAAGTCTGTTGTTAGCC+	59.24
	RPTCTGCCCAGAACTTGTGTAACT-	59.56
IL13RA2	FPGCGGGGAGAGAGGCAATATC+	60.04
	RPGATAGACTGGCGGCAAAGGT-	60.11
PDGFR	FPGCTGTTACCCACTCTGGGAC +	60.04
	RPTGGTGTCCTTGCTGCTGATG -	60.61
LTF	FPGTGCCATTGCAACCCTTGTC+	60.32
	RPGAGTTCGTGGCTGTCTTTCG-	59.2

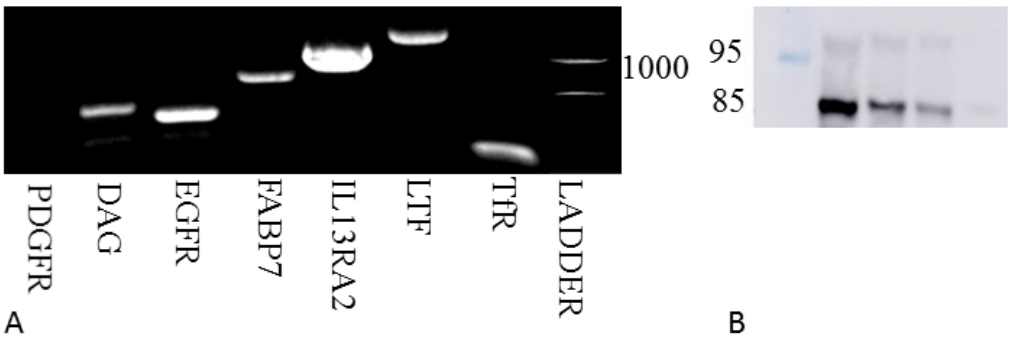

Figure 3. Testing Target Expression Using RT-PCR & Western Blots. A) RT-PCR Analysis on Agarose Gel Electrophoresis of total RNA Extracted from U251-MG cells Demonstrates the Expression of DAG1, EGFR, FAB7, IL13Rα2, LTF and TfR. B) Western Blots on 8% tris-glycine Gel-electrophoresis were probed with G1/221/12 Mouse Anti-Human Tf Receptor Primary Antibody followed by HRP Tagged Rabbit Anti-Mouse Secondary Antibody and Imaged Using Amersham Imager 600.

III.3.3 Liposome preparation and characterization

III.3.3.1 Liposomes preparation

$Gd_3N@C_{80}$ free as well as $Gd_3N@C_{80}$ encapsulated liposomes were formulated by disolving, EGGPC + Chol (8.1:1.75), EGGPC + Chol + $Gd_3N@C_{80}$ (8.1:1.75:0.5), EGGPC + Chol + PEG2PE + $Gd_3N@C_{80}$ (7.1:1.75:1:0.5) and EGGPC + Chol + AmineDSPE + $Gd_3N@C_{80}$ (7.1:1.75:1:0.5) mg ratios in 5 ml chloroform. After removing the organic solvent, the lipid layer was subjected to hydration using 300 mM $(NH_4)_2HPO_4$ solution at 7.4 PH, then vortexed and sonicated until the lipid layer was completely dissolved in the hydrating medium. The multi-laminar vesicles (MLV) were extruded through 400 -100 nm filters respectively. Free molecules, those not part of the formulated liposomes, were removed using a 2 Kd molecular weight cut off dialysis cassette immersed in HEPES saline solution (140 mM NaCl, 10 mM HEPES buffer).

DXR was loaded (0.25 mg/ml) remotely by incubating the liposomes & DXR in a 7 °C saline HEPES buffer (Figure 4).

$Gd_3N@C_{80}$-OH encapsulated, PEGylated liposomes composed of EGGPC: CHOL: PEG2PE: DSPE-PEG2K-NH_2 (53:43:4:1) or EGGPC: CHOL: PEG2PE: DSPE-PEG2K-Amine: DSPE-PEG2K-COOH (53:43:4:0.5:0.5) were formulated as shown in Figure 4 [172-175]. Briefly, lipids dissolved in chloroform were evaporated using rotary evaporator to form a thin lipid film followed by hydration with 250 mM ammonium sulfate and $Gd_3N@C_{80}$-OH (1.4 mg/ml) solution adjusted to a 5.4 PH (4 °C) which results in multilamellar vesicles (MLV). The liposomes were resized using an Avanti mini extruder passing seven times through 200 and 100 nm pore diameter polycarbonate filters respectively.

Next, liposomes were conjugated with proteins using EDC/NHS chemistry. Briefly, 748 mg of EDCI and 1.13 mg of NHS were added to 3 different 1 ml carboxylic functionalized liposomes and the mixture was gently stirred for 10 min at room temperature. Mono-tagged liposomes were formulated by adding equal amount of Tf and Lf (5 mg) to the two 1 ml suspensions respectively and the mixture was kept for 3 h at room temperature. For a dual tagging process, an equal amount of protein (half each) was mixed with COOH-functionalized liposomes for the same period as in the case of mono-tagged liposomes. Unattached proteins were removed using dialysis cassette immersed in HEPES (4-(2-hydroxyethyl)-1-piperazineethanesulfonic acid) saline buffer for overnight. The attachment of proteins to the liposomes was confirmed as described below. Lastly,

0.44 mg of DXR was added to 1 ml of each class of liposomes (for a lipid concentration of 6.54 mg/ml, the final DXR concentration was 0.76 mM). After a through mixing, the suspensions were incubated at 40 °C in a water bath and intermittently shaken for 20 min to produce DXR and $Gd_3N@C_{80}$ encapsulated liposomes.

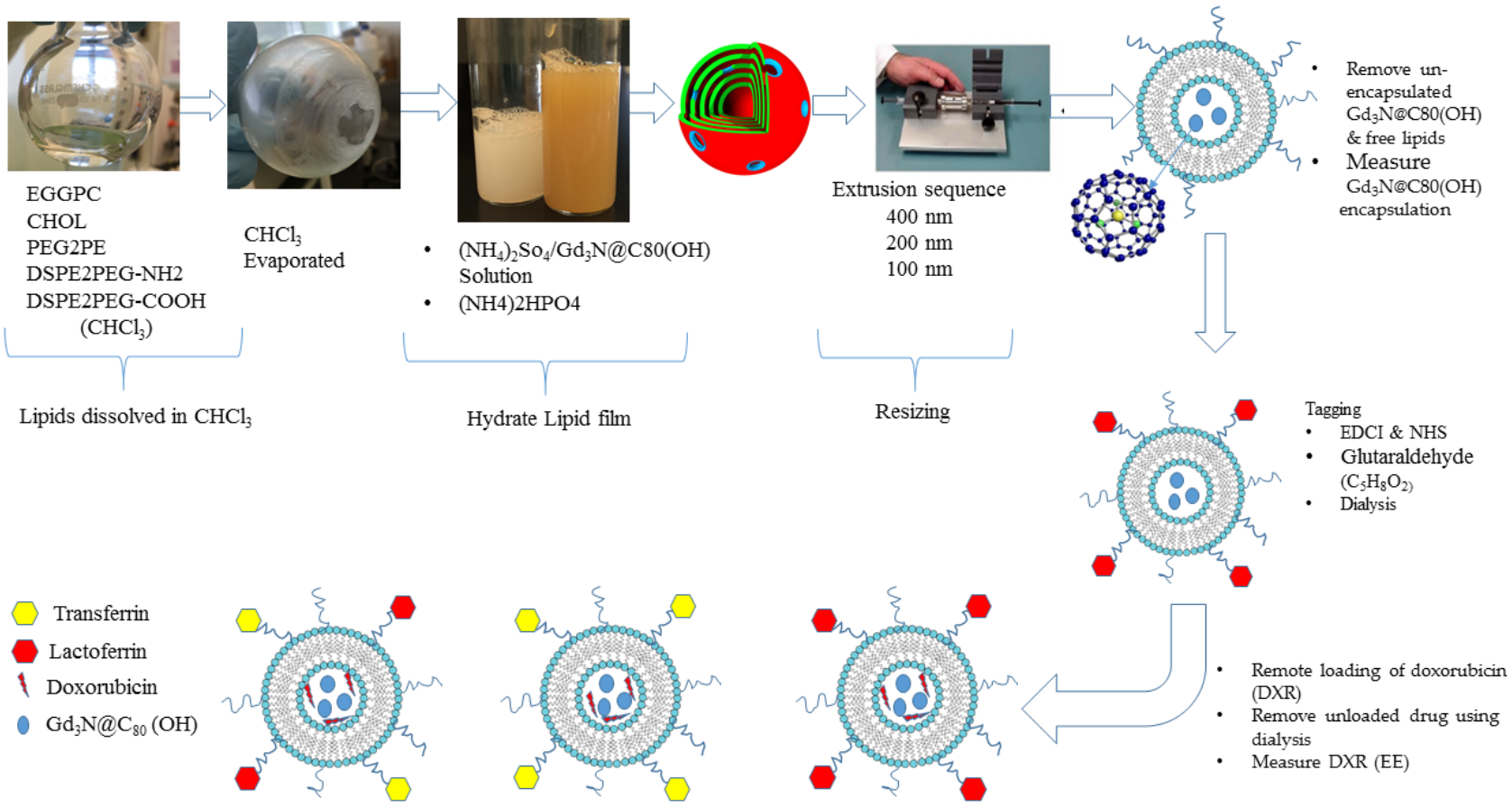

Figure 4. A Flowchart Indicating the Formulation and Tagging of DXR and $Gd_3N@C_{80}$-OH Loaded Liposomal Theranostics.

III.3.3.2 DXR and Gadolinium quantification

The amount of DXR inside the liposomes was measured using Biotech MX/Mono-based Microplate Reader. First, an absorbance standard curve was established for 12.5, 6.25, 3.125 and 1.5625 µg/ml DXR at 475 & 580 and 470/570 nm excitation and emission wavelengths. The DXR concentration inside the protein tagged liposomes was estimated by measuring the absorbance, after lysis with methanol, and using the standard curve equation. The encapsulation efficiency of the liposomes was calculated using the equation ($EE= (W_{inside} / W_{total}) X 100$) where W_{inside} is the inside liposome DXR concentration and W_{total} is the initial DXR concentration. Similarly, the amount of Gd was estimated via inductively coupled plasma optical emission spectrometry (Varian 710-ES ICP). Briefly, the $Gd_3N@C_{80}$ encapsulated liposomes were diluted to 3 ml (3% nitric acid) and the emission intensity of Gd in the sample was measured together with the emission intensity of standard Gd concentrations. The final amount of Gd ($Gd_3N@C_{80}$) inside the theranostics was estimated from the standard curve equation developed for known concentrations. The encapsulating efficiency was calculated using ($EE= (W_{inside} / W_{total}) X 100$) where W_{inside} is the concentration of Gd inside the theranostics and W_{total} is the total concentration of Gd in functionalized and non-functionalized stock $Gd_3N@C_{80}$ solution used for hydration (formulation).

III.3.3.3 Characterization using TEM, UV-VIS and FTIR spectra

The spherical assembly of the liposomes was examined using transmission electron microscopy (Carl Zeiss Libra 120 plus TEM Microscope). Briefly, TEM grids were sputter coated using a Leica Ace Sputter coater. Then the grids were immersed into the sample, air dried, and the particles were examined at several magnifications. UV-VIS spectroscopic absorbance was measured to assess the attachment of proteins to liposomes. Similarly, FTIR spectra were measured to confirm the targeting process and to evaluate the presence of functional groups associated to the liposomes and ligands. For this purpose the symmetric/asymmetric stretch of CH_2 (around 2850 cm^{-1}, 2920-2960 cm^{-1} respectively), the carbonyl stretching mode C=O (1800–1680 cm^{-1}) and the phosphate head group vibration regions (1260–1000 cm^{-1}) [176] are considered to monitor liposome components. The existence and modification of amine/carboxylic functional groups, before and after tagging the liposomes with proteins were assessed by evaluating the N-H stretch, N-H bend and C-N stretch occurring at 3300-3500, 1600 and 1080-1360 cm^{-1} wavenumbers. Similarly, the presence of carboxylic acid was assessed in the 1725-1700 cm^{-1} region [176].

III.3.3.4 Size and zeta potential measurements

The size and zeta potential of the liposomes were measured using Malvern zetasizer and Brownian motion of the liposomes was captured using Nanosight nano-tracking analysis. For zetasizer measurements, liposomes were diluted with water (at

0.1/0.9 ratio) and the refractive index, the viscosity and dielectric constants of the dispersant were set to 1.33 (at 25 °C), 0.87 cP and 78.5, respectively. As the average size and zeta potential values alone may not be informative enough, the quality control correlation graphs as well as the corresponding size and zeta potential values are presented. The particle size was also measured using NanoSight LM10 device mounted on an optical microscope at 20 X objective and the Brownian motion of the liposomes was captured at room temperature and is provided as supplementary material.

III.3.4 Cytotoxicity

The cytotoxic effect of the theranostic on U251-MG cells was examined using the MTT assay. U251-MG cells were seeded in triplicate for 72 hours in a 96-well plate at a density of 2.8 X 10^4 cells per well. After the cells reached confluency, the theranostic or controls were added (12 µg/ml DXR in 100 µl) in cell culture medium. The first groups of control cells were treated with equal volume of DXR-free liposomes. Positive control cells were also treated with an equal concentration of free DXR (no liposomes), 12 µg/ml, and another group of wells were left untreated to serve as negative controls. After 72 hours of treatment, the cell viability was determined by MTT method as described in the Vybrant MTT cell proliferation assay kit according to the manufacture's protocol [177].

III.3.5 Statistical analysis

Statistical analyses were performed using Excel. The variances between the samples were analysed and significance levels were calculated using Student's t-test (*$p < 0.05$, **$p < 0.01$, ns $p > 0.05$) and data are presented as mean ± standard deviation.

III.4 Results and Discussions

III.4.1 RT-PCR and Western blot

The expression of genes and proteins on a cell line could be affected by culturing condition, the number of passaging etc. Furthermore, issues on U251-MG and U373-MG cell lines were reported where the cell lines might no longer reflect the original tumors that they are supposed to represent [178]. Therefore, the expression Tf receptor in U251-MG along with other potential targets was tested using RT-PCR. The test confirmed the expression of Tf-receptor (TfR), IL13Rα2, EGFR, DAG1, FABP7 and LTF genes on the cell line and a control receptor that is not (or very less) expressed in U251-MG cells PDGFR [100] (Figure 3). Western blotting also revealed the expression of TF receptor on U251-MG cells with 85KD band marker. Furthermore, the intensity of the western blots increases with cell concentration across the lanes confirming the presence of the receptor on U251-MG cells.

III.4.2 Liposome development and characterization

III.4.2.1 Characterization using TEM, UV-VIS & FTIR

TEM images of the liposomes at different magnifications confirmed the spherical assembly of the liposomes (Figure 5). The UV-VIS and FTIR spectra measurements

support the successful conjugation of proteins to the liposomes as depicted by a clear difference in the absorbance signatures of those proteins tagged liposomes compared to non-tagged counterparts. Proteins absorb UV light at 280 and 200 nm, due to the absorption of aromatic amino acids and the absorption of peptide bonds respectively. Several authors have reported UV-VIS signatures of Tf [179] and Lf (Fig 1 A of [180]) and both ligands have similar relatively higher absorption at 280 nm. As Tf and Lf are proteins of the same family with similar shape, similar absorbance signatures were anticipated around 280 nm in Tf-tagged, Lf-tagged as wells as Tf+Lf tagged formulations. As anticipated, a clearly evident higher absorption at nearly 290 nm wavelength, on the UV-VIS spectra in protein-tagged liposomes is observed compared to the absorbance signature of the non-tagged liposome (Figure 6). A high absorption around 230 nm wavelength is in agreement to previously reported UV-VIS liposomes' signatures [181, 182] and a relatively amplified absorption around 280 nm are consistent with an extinction measurement of Tf attached liposomes reported in [182].

The presence of PEG in the PEGylated liposomes is supported by FTIR absorbance around 2880 cm-1 due to a C-H stretch of PEG (Figure 7) [183]. CH2 asymmetric stretching near 2925 cm−1 and symmetric stretch near 2850 cm−1 , CH2 scissor and bend at 1460 and 1420 cm-1 respectively are in agreement with previous EGGPC signatures [184]. PO2 asymmetric stretching near 1220 cm−1 and symmetric stretch at 1088 cm-1 (Figure 7) are also in agreement with previously reported signatures of EGGPC or EGGPC/Cholesterol liposomes [184]. Those signatures support unaffected and non-modified EGGPC in the liposome particles. As in the case of the UV-VIS

spectra, the FTIR signatures also support the tagging process. The peak near 1650 cm-1 in the FTIR signature of protein tagged liposomes could be related to amide I band associated with a C=O stretching vibrations of peptide bonds. The peaks near 1540 cm-1 (N-H bending vibration/C-N stretching vibration) and 1240 cm-1 (C-N stretching vibration/N-H bending vibration) could be due to the amide II band and amide III bands, respectively (Figure 7). The peak near 3300 cm-1 can also be N-H bending vibration and the peak near 1400 cm-1 from protein side-chain of COO- and are indicated maximum in the protein tagged liposomes. The highest amplitude on 3300-2500 cm-1 depicted on non-tagged liposomes compared to protein tagged liposomes may show a modification of the carboxylic functional group, in the later, during the conjugation process (Figure 7). The higher amplitudes between 1320-1210 cm-1, typical wave number range for C-O stretch, in non-tagged liposomes than on protein tagged ones may indicate the modification of carboxylic functional group. NH stretch at 3288 cm-1 clearly visible on Lf, Tf, Lf and Tf tagged liposomes compared to non-tagged counterparts is likely from secondary amines (Figure 7). These results, in general, support the conjugation of the liposomes with the proteins.

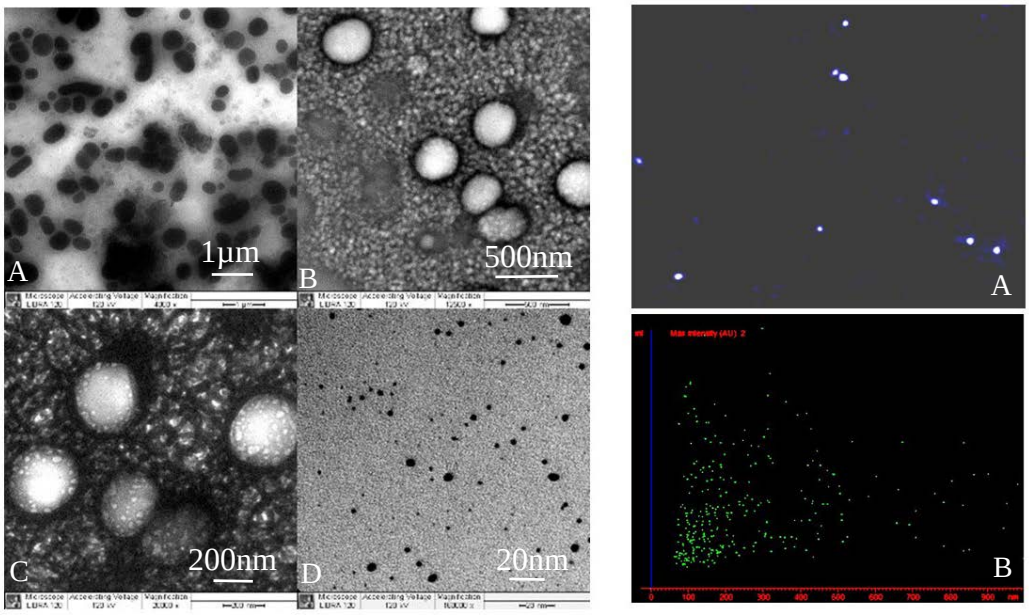

Figure 5. Transmission Electron Microscope Images and Brownian Movement Analysis Support the Formulation of Stable Liposomes. In the left panel TEM images of (EGGPC + Cholesterol) Liposomes, main lipid components of all Liposomes, at (A) 4,000 X, (B) 12,500 X, (C) 20,000 X and (D) $Gd_3N@C_{80}$ at 160,000 X. In the right column, (A) a snapshot of a video capturing Brownian Motion analyzed using Nanoparticle Tracking Analysis (NTA), and (B) corresponding size distribution versus intensity of $Gd_3N@C_{80}$ loaded Liposomes. A video file of the particles moving under Brownian motion is also provided in supplementary information 1.

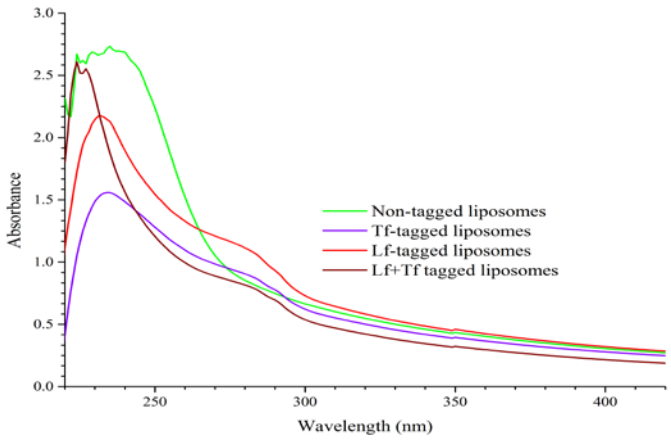

Figure 6. UV-Vis Spectra Support the Formulation of Protein Tagged Theranostics. Tf tagged liposomes are indicated in purple, Lf tagged liposomes (red), dual-tagged (Lf and Tf) liposomes (brown) and non-tagged liposomes indicated in green. The presence of absorbance amplitude change is evident on protein tagged liposomes compared to that of non-tagged liposomes.

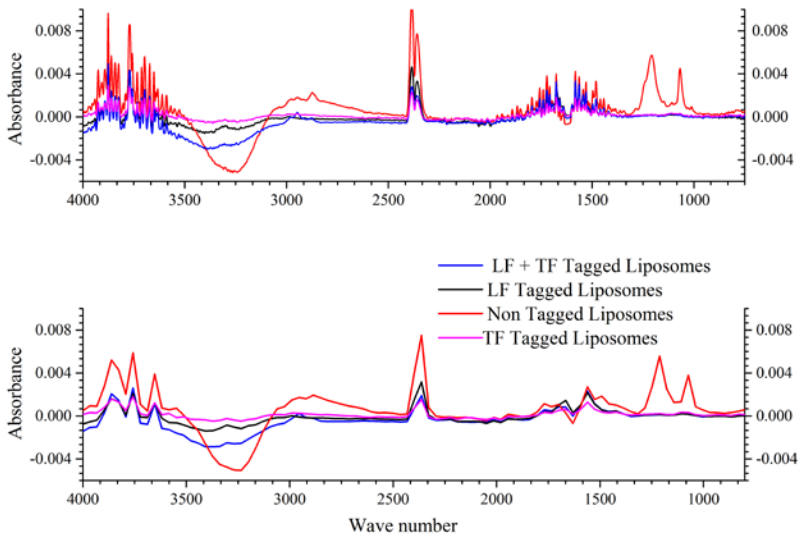

Figure 7. FTIR Spectra Support the Tagging and PEGylating of Theranostic Liposomes. The FTIR Absorption Spectra of Protein tagged Liposomes compared to non-tagged are indicated after subtracting the buffer spectra. FTIR scanning parameters were set to 4 scans at 4 cm^{-1} resolution covering 400-6,000 cm^{-1} wavenumber range (for a detailed explanation of the absorbance see sections 2.5 and 3.6). The smoothed version of the original figure (top) is shown at the bottom.

III.4.2.2 Encapsulation efficiency

A scatter plot and correlation based encapsulation efficiency predictions confirmed successful loading of the liposomes with DXR as well as with $Gd_3N@C_{80}$ particles (Figure 8). DXR encapsulation efficiency of non-functionalized $Gd_3N@C_{80}$ containing liposomes formulated using ammonium phosphate hydration process was 94% and accords the encapsulation efficiency reported in [175]. However, the non-functionalized $Gd_3N@C_{80}$ encapsulation efficiency was low (2%). In an attempt to increase $Gd_3N@C_{80}$ encapsulation efficiency, OH-functionalized $Gd_3N@C_{80}$ dissolved in ammonium sulphate solution was used for the hydration process. In the later approach, $Gd_3N@C_{80}$ encapsulation efficiency of the liposomes was increased to 13%. After DXR

loading and targeting these functionalized $Gd_3N@C_{80}$ containing liposomes, the DXR encapsulation efficiencies were 45%, 57% and 46% respectively for (Tf + Lf), Tf and Lf tagged liposomes.

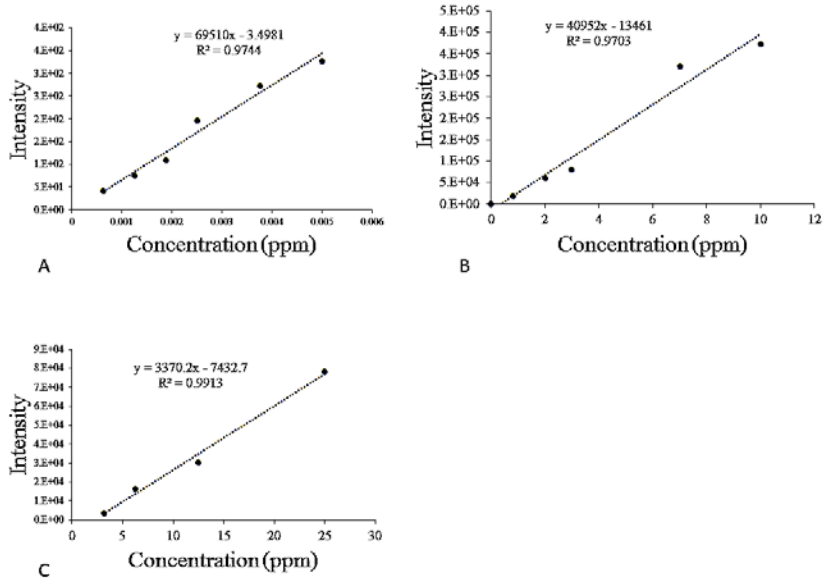

Figure 8. Standard Curves to Estimate DXR and Gd Encapsulation Efficiencies. A) A linear Standard Curve used to predict $Gd_3N@C_{80}$-OH Encapsulation Efficiency in Liposomes. Emission Intensity of different concentrations of Gd standards dissolved in 3% HNO_3 solvent matrix were measured using ICP and $Gd_3N@C_{80}$ was predicted from the correlation equation. B) A linear Standard Curve equation used to predict gadolinium concentration in $Gd_3N@C_{80}$-OH solution. C) Linear Standard Curve used to predict DXR Encapsulation Efficiency of targeted Theranostic Liposomes. DXR excitation and absorption were set to 470 & 570 nm wavelengths respectively.

III.4.2.3 Size and zeta potential measurements

The average hydrodynamic size of non-tagged liposomes was 146 nm (Table 5) and after the tagging process it was 148, 142, and 148 for Tf, Lf and (Tf + Lf) tagged liposomes respectively (Table 5, Figure 9). After the liposomes are loaded with DXR, the average hydrodynamic sizes were 139, 142 and 149 nm for Tf, Lf and Tf + Lf tagged theranostics respectively (Table 5). The size differences observed after loading with DXR could be due to additional processes such as the remote loading and dialysis. The polydispersity index (PDI) values for most of the formulations are within 0.2 suggesting a narrow size distribution range. Approximately 70% of the liposomes are 60-80 nm in size (Figure 10). Such smaller-size liposomal formulations depicted by single as well as dual tagged and PEGylated particles are predicted to have less interaction with plasma proteins, i.e. their smaller sizes will help evaded a capture by the reticuloendothelial system (RES), may ensure longer half-life in the blood, and have a potential to accumulate at the tumor site [185]. These size distributions are also in accord with the size of nanoparticles reported to cross the BBB and got accumulated in the brain [186, 187]. The average zeta potential of $Gd_3N@C_{80}$ loaded non-tagged liposomes at 7.4 PH was -19 mV and after targeting it was -14, -16 and -17 mV for Tf, Lf, and Tf + Lf tagged liposomes respectively (Table 5, Figure 11). After the drug loading process, the average zeta potential was -19, -17 and -15 mV respectively for Tf, Lf and Tf +Lf tagged liposomes at the same PH (Table 5, Figure 11). The zeta potential values in this study are in accord with the zeta potential values reported being effective for brain delivery [187-189].

Table 5. Zeta Potential, Average Hydrodynamic Diameter and Polydispersity Index of Single, Dual and Non-tagged Liposomes Loaded with $Gd_3N@C_{80}$-OH and DXR. $Gd_3N@C_{80}$-loaded represent devoid of DXR and ((DXR + $Gd_3N@C_{80}$)-loaded) contains both.

Liposome type	Zeta Potential (mean ± SD mV)	Average Size (mean nm)	PDI
Tf -tagged- ($Gd_3N@C_{80}$-loaded)	-14.7±1.07	148.3	0.215
Lf- tagged- ($Gd_3N@C_{80}$-loaded)	-16.5 ±1.04	142.2	0.257
(Tf +Lf)-tagged- ($Gd_3N@C_{80}$-loaded)	-17.1±1.27	148.7	0.218
Non-tagged-($Gd_3N@C_{80}$-loaded)	-19.8 ±1.56	146.3	0.220
Tf -tagged - ((DXR + $Gd_3N@C_{80}$) -loaded)	-19.9 ±0.81	139.4	0.204
Lf- tagged - (DXR +$Gd_3N@C_{80}$-loaded)	-17.6±1.31	142.4	0.184
(Lf+ Tf)- tagged - (DXR +$Gd_3N@C_{80}$-loaded)	-15.5±0.61	149.3	0.212

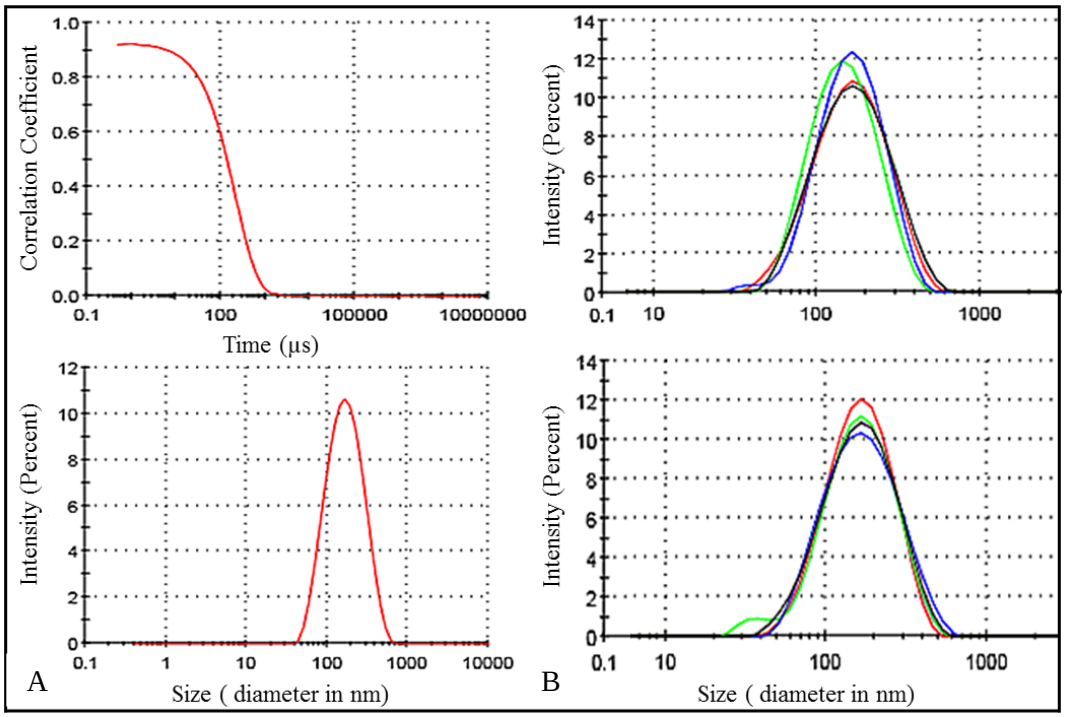

Figure 9. DLS Size Measurements and Size Distribution Analysis of ($Gd_3N@C_{80}$ + DXR) Loaded-Targeted Liposomes versus ($Gd_3N@C_{80}$ only) Loaded-Targeted Liposomes Support the Formulation of Stable Theranostics. A) Example of correlation coefficient graph of (Tf + Lf) tagged, $Gd_3N@C_{80}$ and DXR loaded liposomes at the top with corresponding size distributions indicated at the bottom. B) An overlay of size distribution versus intensity of Lf-tagged $Gd_3N@C_{80}$ & DXR loaded (blue), (Lf + Tf)-tagged $Gd_3N@C_{80}$ &DXR loaded (black), Tf-tagged $Gd_3N@C_{80}$ and DXR loaded (green) and non-tagged liposomes portrayed in red are shown at the top. At the bottom, an overlay of Size distribution versus intensity of Lf-tagged $Gd_3N@C_{80}$ loaded (green), (Lf + Tf)-tagged $Gd_3N@C_{80}$ loaded (blue), Tf-tagged $Gd_3N@C_{80}$ loaded liposomes (red) and non-tagged liposomes are represented in black.

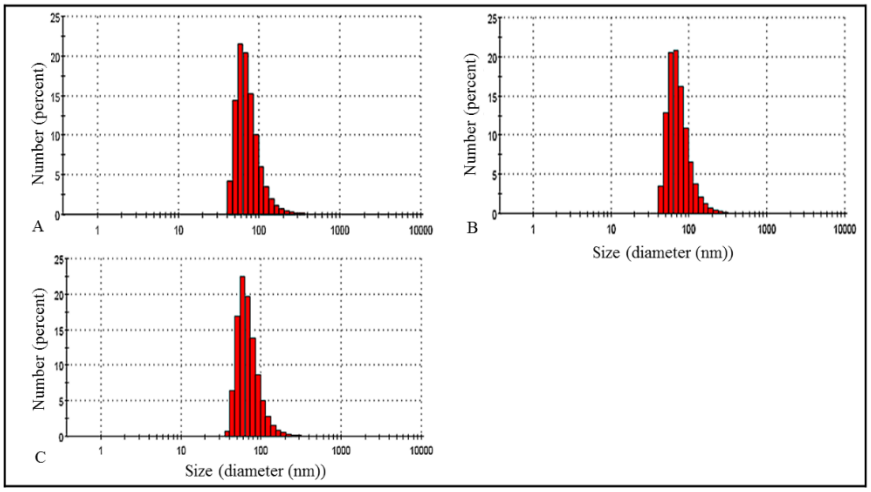

Figure 10. The Size Distribution of Liposomes by their Number Confirms that Most Nanoparticles Possess < 100 nm Hydrodynamic Diameter. A) Lf + Tf tagged $Gd_3N@C_{80}$ & DXR loaded, B) Tf tagged $Gd_3N@C_{80}$ &DXR loaded, C) Lf tagged $Gd_3N@C_{80}$ + DXR loaded liposomes.

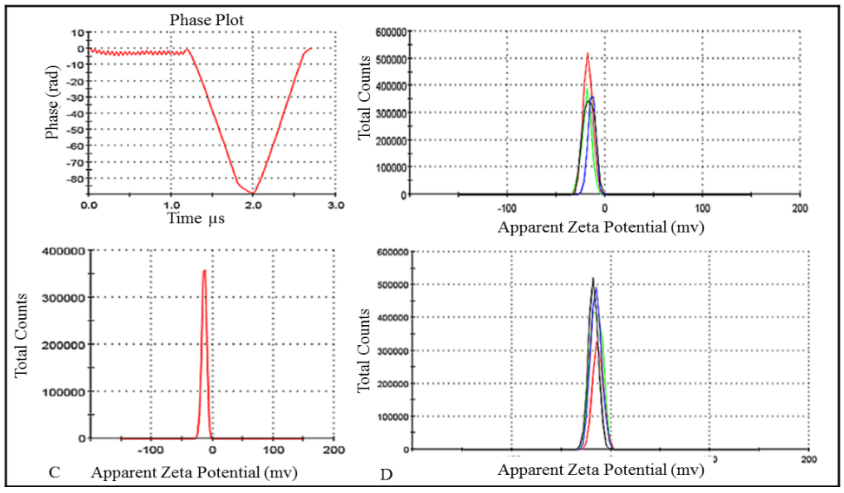

Figure 11. Zeta Potential Measurements Support the Formulation of Stable, at Physiological PH, Drug and Imaging Agent Containing Liposomes. A) Example phase plot of (Tf + Lf) tagged, $Gd_3N@C_{80}$ and DXR loaded, liposomes shown at the top with corresponding apparent zeta potential given at the bottom. B) An overlay of zeta potential distribution of ($Gd_3N@C_{80}$ + DXR) loaded liposomes shown at the top where non-tagged liposomes portrayed in red, Lf-tagged liposomes (black), (Lf + Tf)-tagged liposomes (blue), Tf tagged liposomes (green) & an overlay of zeta potential distribution of $Gd_3N@C_{80}$ only loaded liposomes shown at the bottom where non-tagged liposomes are represented in black, Lf tagged liposomes (green), (Lf + Tf) tagged (blue), Tf tagged liposomes represented in red.

III.4.3 In vitro evaluation

Tf and Lf are quite similar in sequence and structure and coordinate iron in the same manner, but they differ in their affinities for iron as well as their receptor binding properties [190]. While Tf is known to couple with Tf receptor, Lf is suggested to couple with its own receptor [191] but also with Low density lipoprotein receptor-related protein 1 (LRP1) and LRP2 [192]. The difference in the expression of levels of TfR and LfR is more pronounced in U251-MG cells compared to the expression levels in other glioma cells such as U87-MG [101]. As the difference in the magnitude of TfR and LfR (example LRP1) expression in U87-MG is not clear (the protein atlas [193]), U251-MG

was selected for the in vitro evaluation. As shown in Figure 9 A, the viability assay is in line to the expression level of the receptors in U251-MG. Tf-modified theranostics are more toxic followed by (Tf+Lf) and then Lf-tagged. (Tf+Lf)-modified are less toxic, mainly, because they possess half of the Tf in Tf-modified theranostics. However, it is critical to notice that (Tf+Lf)-modified theranostics also reduced the cell viability significantly (Figure 12). As DXR-free liposomes never induce a significant negative effect on the metabolic activity of the cells, viability reductions observed in Tf-tagged and (Tf + Lf)-tagged theranostics treated cells are most likely due to DXR and these results in line to the viability reductions observed in free DXR treated cells (Figure 12). Therefore, one reason for the difference in toxicity (i.e. for the reductions in metabolic activity of the cells) is the degree of expression of the receptors targeted by the ligands. The expression of LRP1 and intelectin1 (ITLN1) is quite low and no LRP2 expression is observed on U251-MG cells (the protein atlas [193]).

Keeping the differences in the degree of expression of these receptors on U251-MG cells and the proportion of Tf in the theranostics, a higher toxicity of Tf-tagged theranostics compared to Lf-tagged theranostics support the notion that the mechanism of delivery is indeed receptor mediated. The cell viability reductions in (Lf + Tf)-tagged theranostics treated cells (73%) corroborate with the lower viability recorded in cells treated with Tf-tagged theranostics (41%) and in Lf-tagged theranostics treated cells (92%). The viability assay, shown in Figure 12 A, is also in line with the light microscope visualization taken after the treatments (Figure 12 B). Free DXR, Tf-tagged as well as (Tf + Lf)-tagged theranostics resulted in lower cell proliferations compared to

untreated controls. These results support the hypothesis that (Tf + Lf)-tagged theranostics have the potential to specifically kill TfR expressing cancer cells. The superiority of the dual modification compared to single modified counterparts is that it would be less toxic to major organs that express TfR while killing the cancer cells which express TfR, LfR or both TfR & LfR to a larger extent.

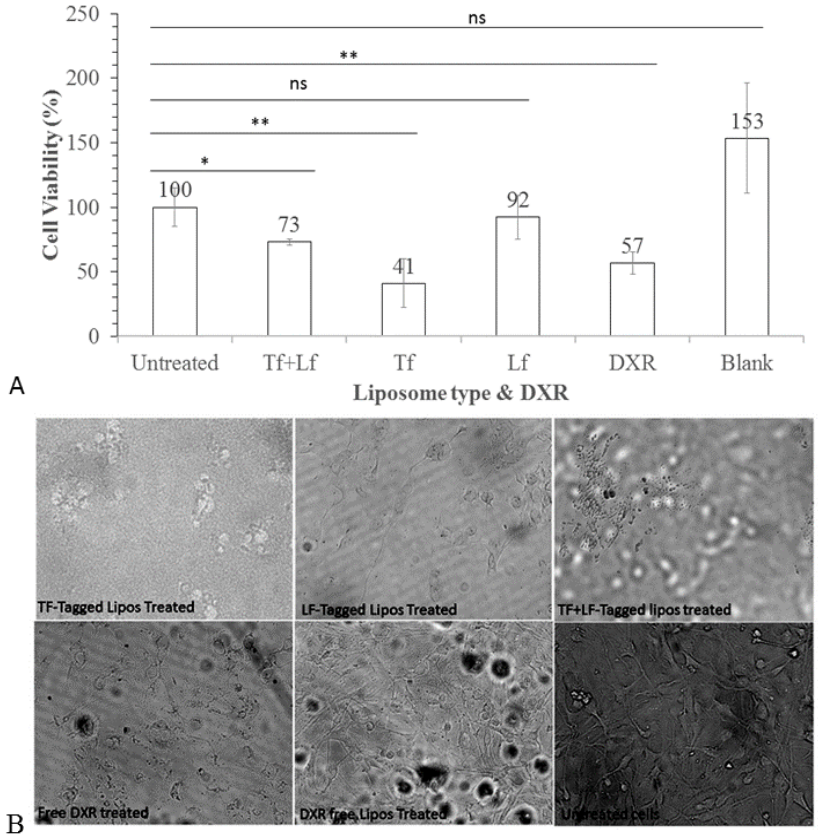

Figure 12. MTT Cell Viability Assay Confirms the Cytotoxic Effect of Single (Tf) and Dual tagged (Tf + Lf) Theranostics on U251-MG cells. The cell viability is indicated in percent after 72 hrs. incubation of U251-MG cells with Tf & Lf tagged (Tf + Lf), Tf tagged (Tf), Lf tagged (Lf) liposomes all loaded with $Gd_3N@C_{80}$ & DXR; blank liposomes (loaded with $Gd_3N@C_{80}$ but devoid of DXR) and free DXR (non-encapsulated DXR). The untreated cells were set to 100% (controls) cellular viability. These results are representatives of three independent experiments and the data values are expressed as the mean ± standard deviation (SD), n=3. B) A comparison of U251-MG cells treated with DXR free liposomes with respect to those treated with DXR loaded liposomes supported the cytotoxic effect of the theranostics on glioma cells. Cells treated with targeted liposomes loaded with DXR and those treated with free DXR shown low viability as depicted with light microscope visualizations of the cells after 72 hrs. of the treatment. The images from right to left represent U251-MG cells treated with TF tagged ($Gd_3N@C_{80}$ & DXR loaded), LF tagged ($Gd_3N@C_{80}$ and DXR loaded), TF + LF Tagged ($Gd_3N@C_{80}$ &DXR loaded liposomes), free DXR, blank liposomes ($Gd_3N@C_{80}$ loaded but DXR free), and untreated cells.

III.5 Conclusion

Search for new therapeutics and diagnostics for GBM, the deadliest brain tumor, has been a higher priority. In this chapter novel, theranostic liposomes tagged with both Lf and Tf (1:1 ratio) are constructed for the first time to harness the potential of crossing the BBB and kill transferrin receptor expressing GBM and glioma stem cells. These dual-tagged theranostics contain DXR and a novel imaging agent ($Gd_3N@C_{80}$-OH) and are PEGylated. Furthermore, > 70% of these theranostic liposomes possess 60-80 nm diameter and have < 0.2 polydispersity index which signifies narrow particle-size distribution. Encapsulation efficiency, zeta potential, FTIR and UV-VIS measurements support the formulation of DXR & $Gd_3N@C_{80}$-OH loaded, targeted and stable liposomes at physiological PH. These dual-tagged theranostics exhibited improved inhibitory effects in U251-MG cells compared to Lf mono-tagged counterparts. The results of this study demonstrated that DXR and $Gd_3N@C_{80}$-OH loaded and Lf & Tf dual-tagged, PEGylated liposomes might be potential drug and imaging agent delivery systems for GBM treatment.

CHAPTER IV

ASSESSING THE STRUCTURAL STABILITY OF $GD_3N@C_{80}$ AND $GD_3N@C_{80}(OH)_{42}$ CONTAINING LIPID BI-LAYERSIN PHYSIOLOGICAL SOLUTIONS USING MOLECULAR DYNAMIC SIMULATIONS

IV.1 Abstract

Gadolinium (Gd) loaded fullerenes are potential MRI components of future theranostic liposomes due to their higher relaxivity, up to 25 fold higher, compared to traditional contrast agents. However, the dynamics and structural stability of $Gd_3N@C_{80}$ containing lipid bilayers in physiological salt solutions and the interactions of $Gd_3N@C_{80}$ with the lipid bilayer constituents are uncertain. In this chapter, the structural stability of C_{80} & $C_{80}(OH)_{42}$ containing lipid bilayers constructed from POPC, DSPE, cholesterol (CHOL) and solvated in KCl, NaCl and $CaCl_2$ solutions are evaluated using molecular dynamic simulations. To this end, root means square deviations (RMSD), area per lipid (APL), radial distribution function (RDF) of ions, number density profiles (NDP), order parameters (SCD), lipid bilayer thickness (LBT) and lipid interdigitations (LI) are calculated to assess the effect of the molecules on the stability of the lipid bilayer structure or vice versa. Further, the dynamics of the fullerene cages across different regions of the lipid bilayers are studied using steered molecular dynamic simulations

(SMD). The results indicate that C_{80} & $C_{80}(OH)_{42}$ remains structurally stable throughout the simulation windows. Furthermore, the molecules moved off the center towards the lipid head groups but never induced substantial structural instability of the bilayers. Carbon-deuterium order parameter (SCD) simulations indicated that lipids residing closer to C_{80} (< 20 Å) have lower lipid order compared to lipids residing closer to $C_{80}(OH)_{42}$. However, the overall lipid bilayer (LBL) structures remain stable throughout the simulation windows. The energy required to displace $C_{80}(OH)_{42}$ across the lipid bilayer is found to be higher than the energy required to displace C_{80}, partly, due to hydrogen bonding of the former with POPC in the lipid bilayers. These results support the hypothesis that OH-functionalized fullerene cages and thereby OH functionalized Gd-fullerene containing liposomes to be stable in physiological salt solutions.

IV.2 Introduction

As discussed in the previous chapters, Gd-loaded endofullerenes such as $Gd@C_{82}$ and $Gd_3N@C_{80}$ have attracted much attention as potential magnetic resonance imaging (MRI) contrast agents, given their inherent higher 1H relaxivity compared to most commercial contrast agents [194]. Moreover, the fullerene cage is predicted to be stable and thus prevent toxic Gd ions from being released [179]. Thus, their use as the diagnostic component of new molecular species continues to grow [53, 167, 195].

In spite of the numerous *in-vitro* and *in-vivo* studies on $Gd_3N@C_{80}$ incorporated into liposomal formulations, computational studies to explore the localization and the interaction of functionalized or non functionalized C_{80} with liposome-lipids are

uncommon. The very few molecular dynamics simulations that explored the interactions of fullerenes and their derivatives with lipid bilayers include those reported in [196, 197]. However, these studies focus on the interaction of C_{60} with lipid membranes developed from single lipid (dipalmitoylphosphatidylcholine, DPPC) and their approaches mainly focus on the potential mean of force analysis. To my knowledge, there are no reported molecular dynamic simulations based structural stability study of C_{80} and its derivative containing lipid bilayers in physiological salt solutions. Furthermore, molecular dynamics simulations based studies are essential as experiments associated with phospholipids and Gd endofullerenes are expensive.

The aims are: 1) to investigate the stability of $Gd_3N@C_{80}$ and $Gd_3N@C_{80}(OH)_{42}$ inside lipid bilayers by exploring structural variations of the outer compartments i.e. C_{80} & $C_{80}(OH)_{42}$ inside lipid bilayers that are immersed in different physiological salts. 2) To study the effect of these molecules on the structural stability of lipid bilayers or vice versa. 3) To evaluate the localization preference of C_{80} and $C_{80}(OH)_{42}$ through energy as well as force computations by applying steered molecular dynamic simulations using NAMD. To this end, structural stabilities of different C_{80} containing lipid bilayers, mainly composed of the lipids tested in the last chapter, are investigated by analyzing the RMSD of the molecules, ND profiles, SCD of lipid chains, LI analysis to assess correlation based leaflet overlap and number of atoms in contact, LBT computations and RDF of cations/anions with respect to lipid head groups by immersing the different lipid bilayers in 0.15 M of NaCl, KCl and $CaCl_2$ solutions.

IV.3 Materials and Methods

The structure information of fullerene isomer (C_{80}) was downloaded in XYZ format from [198, 199]. From the XYZ file, mol2 and protein data bank (PDB) files were generated using Open Babel GUI chemical toolbox. Finally, $Gd_3N@C_{80}$, $Gd_3N@C_{80}(OH)_{42}$ and $C_{80}(OH)_{42}$ were created using ChemSketch and SYBYL-X 2.0 software (Figure 13). To investigate the effect of Gd_3N on the structures of $Gd_3N@C_{80}$ or $Gd_3N@C_{80}(OH)_{42}$, Gd containing and Gd-free counterparts were energy minimized using SYBYL-X 2.0 in Tripos force field by applying a conjugate gradient method for 100 iterations (Table 6). As the lipids used for the theranostics in the last chapter include egg L-α-phosphatidylcholine (EGGPC), polyethylene glycolphosphatidyl ethanolamine (PEGPE) and CHOL and since 1-palmitoyl-2-oleoyl PC is a major constituent of EGGPC, 1-palmitoyl-2-oleoyl-sn-glycero-3-phosphocholine (POPC) is considered as an excellent synthetic substitute for EGGPC [200]. Further, POPC mimic mammalian phospholipids such as EGGPC for it has a saturated chain in its Sn-1 leg and unsaturated chain in its Sn-2 leg. Hence POPC, major component of the lipid bilayers herein, is mixed with CHOL and DSPE at 85:10:5 fractions.

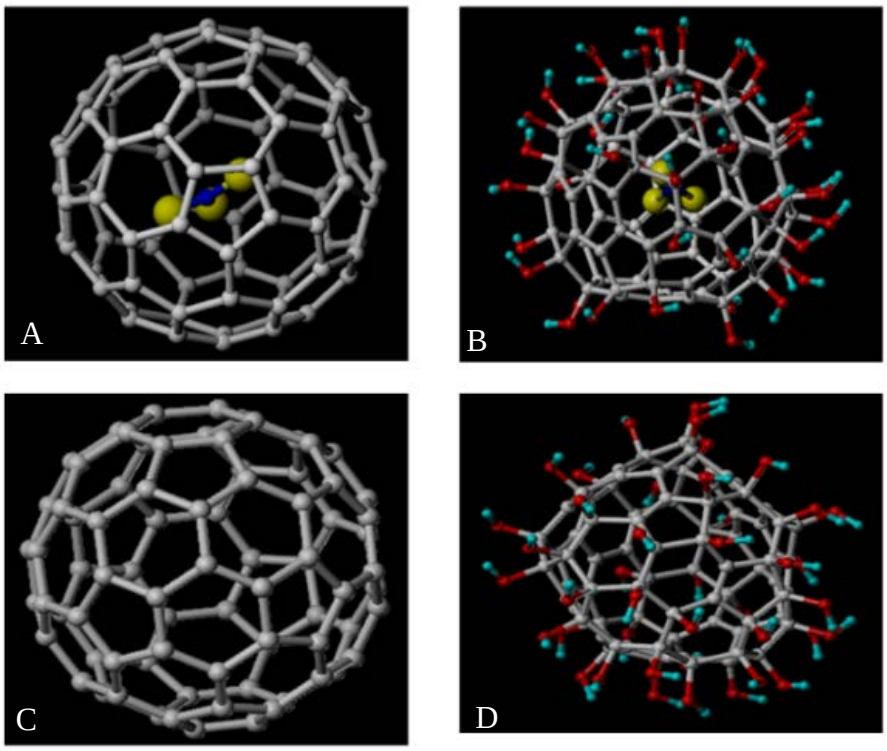

Figure 13. Molecular Structures of C_{80} and its Derivatives Considered for The Study. The figures represent, (A) $Gd_3N@C_{80}$, (B) $Gd_3N@C_{80}(OH)_{42}$, (C) C_{80} and (D) $C_{80}(OH)_{42}$. All are generated using Chemsketch and converted to PDB and mol2 formats using Open Babel software. SYBYL-X 2.0 was used for energy minimization processes using Tripos force field by applying a conjugate gradient method for 100 iterations. The minimization energy values of each component are given in Table 6.

IV.3.1 Lipid bilayer structure descriptions

First, CHARMM parameter (Equation 1 below) and topology files for functionalized and non-functionalized fullerenes were generated using [201]. Then, C_{80} and $C_{80}(OH)_{42}$ containing lipid bi-layers were generated using [202] as follows. C_{80} and $C_{80}(OH)_{42}$ were uploaded in PDB format setting the Z axis as the lipid bilayer normal and the center of the lipid bilayers as the origin of the systems. The fullerenes were positioned at the origin and aligned along the Z axis. The overall lipid bilayer structural assemblies

in different physiological salt solutions considered herein are given in Figure 14 & Table 7. In general, the lipid bilayer systems are 10 X 10 nm width consisting of 32 CHOLs, 272 POPC and 16 DSPE equally distributed in the upper and lower leaflets. The average size of C_{80} was 3.89 and 3.87 Å for major and minor axis respectively. The systems were solvated with 0.15 M of KCl, NaCl, CaCl2 solutions which count up to 24438 water molecules (TIP3), 20 potassium, sodium and calcium ions and 20 or 40 chloride ions in mono and divalent solution respectively. The CHARMM-GUI membrane [202] builder makes the system neutral for long-range electrostatic interactions using the particle-mesh-Ewald method by configuring the ions position through Monte Carlo simulations considering the van der Waals and scaled Coulombic interactions [202].

$$U = \sum_{Bonds} K_b (b - b_o)^2 + \sum_{Angles} K_\theta (\theta - \theta_o)^2 + \sum_{Dihedrals} K_\phi [1 + \cos(n\phi - \zeta)] + \sum_{impropers - dihedrals} K_\omega (\omega - \omega_o)^2 + \sum_{Urey-Brandley} K_u (u - u_o)^2 + \sum_{non-bonded(ij)} \left[\left(\frac{R\min_{ij}}{r_{ij}} \right)^{12} - \left(\frac{R\min_{ij}}{r_{ij}} \right)^{5} \right] + \frac{q_i q_j}{\varepsilon r_{ij}}$$

Equation 1. CHARMM potential energy function. Kb, kθ, and kϕ are bond, angle and dihedral force constants, kω is out of plane bending force constant, Ku is Urey-Bradley constant, Rmin is where the Lennard-Jones potential crosses the x-axis and rij the distance between the interacting particles.

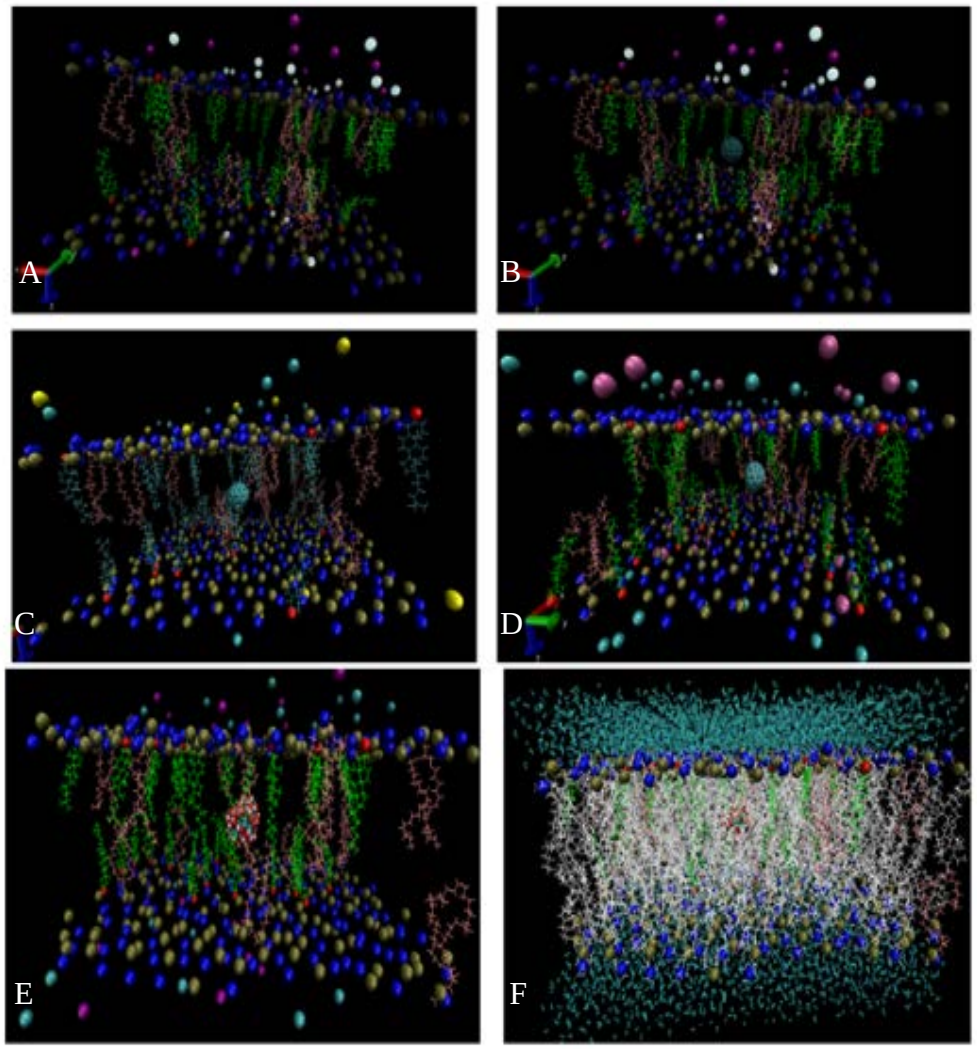

Figure 14. Molecular Assemblies of the Different Lipid Bilayers to Study the Effect of C_{80} and $C_{80}(OH)_{42}$ on the Stability of the Lipid Bilayer Structures Immersed in Physiological Salt Solutions. A) C_{80}/$C_{80}(OH)_{42}$ free lipid bilayer in KCl solution, B) C_{80} containing lipid bilayer in KCl solution, C) C_{80} containing lipid bilayer in NaCl solution, D) C_{80} containing lipid bilayer in $CaCl_2$ solution, E) $C_{80}(OH)_{42}$ containing lipid bilayer in KCl solution and F) lipid bilayer containing all POPC, DSPE, Cholestrol and water shown to represent the whole lipid-water systems. The spheres represent K ions (white), sodium ions (yellow), cacium ions (purple) and the rest are chloride ions.

IV.3.2 MD simulations

The simulations were run with CHARMM force field using NAMD, a parallel molecular dynamics code designed for high-performance simulation of large biomolecular systems compatible with CHARMM potential functions, parameters, and file formats [203]. The systems were subjected to 5,000 energy minimization steps followed by simulations under constant number, volume and temperature (NVT) at 1 fs time step up to a total of 2 ns simulations till the lipid bilayer systems were equilibrated (Figure 15). The production simulation was conducted at a maximum of 2 fs time step totaling up to 20 ns for most of the LBLs and up to 34 ns for the LBL immersed in $CaCl_2$ solution. Trajectory data were collected every 500 fs during equilibration and 2,000 fs during production stages. In all simulations, the temperature was set to physiological temperature (310 K) and trajectory snapshots were taken at different time frames [204]. All simulations in the production stage were run under constant number of atoms, constant pressure (1 bar) and constant temperature (i.e NPT ensemble). Langevin dynamics was applied to non-hydrogen atoms to maintain a 310 K constant temperature with a Langevin coupling coefficient of 1 ps^{-1}. Similarly, Nosé-Hoover Langevin-piston algorithm was used to maintain constant pressure with a piston period of 50 fs and a piston decay of 25 fs [205]. The van der Waals interactions were switched off between 10 and 12 Å by using the forced-based switching function imbedded in NAMD. The structural properties of fullerene-free lipid bilayer immersed in 0.15 M KCl, non-functionalized fullerene containing lipid bi-layer in 0.15 M of KCl, NaCl and $CaCl_2$, and $C_{80}(OH)_{42}$ in 0.15 M KCl were calculated during the simulations. Visual Molecular

Dynamics (VMD) [206] was used to create snapshots of the lipid bilayers at different time frames and to capture the dynamics of functionalized and non-functionalized C_{80} within the lipid bilayers. Finally the evaluation parameters are plotted using QT-grace [207].

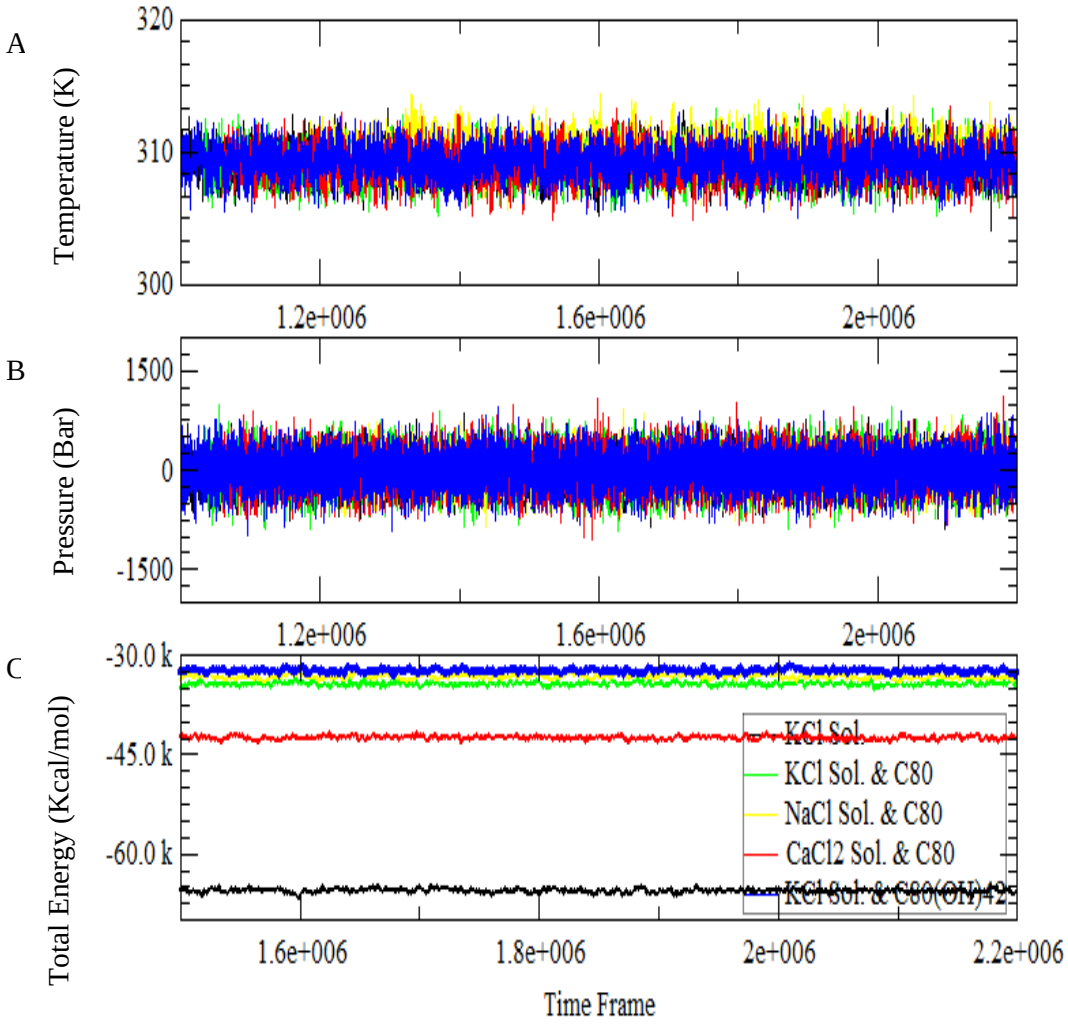

Figure 15. Equilibriation and Energy Minimization of the Different Lipid Bilayer Systems. The systems were equilibrated first under NVT and then under NPT before starting the production protocol. A) constant temperature (310 K), B) constant pressure (average 1 bar) and C) energy minimizations in Kcal/mol. Black lines are C_{80}/$C_{80}(OH)_{42}$ free lipid bilayers immersed in KCl solution, C_{80} containing lipid bilayers in KCl solution (green), C_{80} containing lipid bilayer in NaCl solution (yellow), $C_{80}(OH)_{42}$ containing lipid bilayer in KCl solution (blue) and the red lines represent C_{80} containing lipid bilayers immersed in CaCl2 solution.

IV.3.3 Equilibration and structural stability study

The RMSD of C_{80} & $C_{80}(OH)_{42}$ were calculated using the RMSD visualizer tool plugin in VMD [206]. APL of each lipid species and SCDs along the carbons in Sn-1 and Sn-2 were computed using VMD's MEMBPLUGIN [208]. ND profiles of water, POPC, DSPE, CHOL, K^+, Na^+, Ca^{++} and Cl^- were computed at different time frames along the bilayer normal to assess bilayer structural change or ions percolation [209]. The RDF of K^+, Na^+, Ca^{++} and Cl^- around the phosphatidyl and choline groups were determined using VMD [210] to assess the effect of C_{80} and $C_{80}(OH)_{42}$ on the distribution of bulk ions with respect to the lipid head groups [210]. The trajectories within 20 ns simulation are considered for the stability assessments.

IV.3.4 Steered molecular dynamic simulations

The SMD simulations are conducted at 310 K by controlling the temperature fluctuations using Langevin dynamics scheme embedded in NAMD with integrator parameter time step set to 2 femtosecond. One of the phosphorus (P) atoms of POPC was constrained to stationary and a carbon atom of C_{80}/$C_{80}(OH)_{42}$ was constrained to a point that moves along the z-axis at a constant speed of 0.0001 Å/timestep. The center of mass of C_{80}/$C_{80}(OH)_{42}$ was displaced up to a total of 80 Å by applying a harmonic potential having a force constant of 7.2 kcal/mole/Å. As the pulling simulation is performed very slowly (0.0001 Å/timestep), the process is assumed to be reversible. In other words, the work done during this reversible pulling process is assumed to be equal to the free energy difference of the system when C_{80}/$C_{80}(OH)_{42}$ are at the origin and when displaced out of

the lipid bilayer. Hence, the energies required to displace C_{80} versus $C_{80}(OH)_{42}$ inside lipid bilayers immersed in 0.15 M of KCl was compared. Then the energy required to displace C_{80} inside the lipid bilayers solvated with NaCl and $CaCl_2$ are discussed in terms of the interactions of monovalent and divalent ions with the lipid head groups and interpreted in terms of the overall stability of the lipid bilayers. To this end force profiles and work required to move the molecules, calculated at a constant velocity, are provided for structures taken at different time frames. For a detailed explanation on SMD, the reader is referred to NAMD application package [203].

IV.4 Results and Discussion

To model the energy variations of Gd containing fullerenes with respect to Gd free counterparts, the minimization energies of the different molecules were computed using Tripos force field and are given in Table 6. In those quantities, two differences are clear. First, new electrostatic energy forms have been developed from the functionalization process. Second, Gd containing C_{80} have relatively higher bending energy compared to Gd free equivalents. The increment in bending energy is due to the addition of Gd_3N atoms and it increased the stability of the molecules.

Studying the dynamics of $Gd_3N@C_{80}$ and $Gd_3N@C_{80}(OH)_{42}$ inside lipid bilayers by using any force field including CHARMM requires robust force field parameters encompassing the interaction of Gd, bonded and non-bonded interactions, with surrounding carbon and nitrogen atoms. As these parameters are typically obtained either from *ab-initio* or semi-empirical quantum mechanical calculations or by fitting to

experimental data such as neutron, X-ray and electron diffraction, NMR, infrared, Raman and neutron spectroscopy [211], the strategy was to study the interaction between the LBL lipid components and the fullerene cages or vice versa. Two reasons are taken in to account for this assumption. First, experimental evidences support the firm confinement and stability of Gd inside a very stable fullerene cage. Thus, the dynamics of $Gd_3N@C_{80}$/$Gd_3N@C_{80}(OH)_{42}$ inside the lipid bilayers or liposomes is mainly influenced by the outer cage. Second, conducting molecular dynamic simulations with poorly known CHARMM parameters that represent the interaction of Gd with neighboring atoms, would result in erroneous results. Hence the structural stability discussions given below focus on C_{80} and $C_{80}(OH)_{42}$ containing lipid bilayers. To sum up as the Gd_3N is common between in $Gd_3N@C_{80}$ and $Gd_3N@C_{80}(OH)_{42}$ and the main structural difference is the OH functionalization, the stability studies herein focus on the effects of the outer compartments of the molecules.

Table 6. Energy Minimization/Geometry Optimization for Gd Containing and Gd-free C_{80} & $C_{80}(OH)_{42}$ Molecules that are indicated in Figure 14.

Energy_Type (Kcal/mol)	Gd_3NC_{80}	C_{80}	$Gd_3NC_{80}(OH)_{42}$	$C_{80}(OH)_{42}$
Bond Stretching	51.260	11.067	92.327	15.365
Angle Bending	617.645	118.495	563.013	148.685
Torsional	177.125	176.622	164.111	105.321
Out of Plane Bending	1524.976	1475.513	111.380	44.313
1-4 van der Waals	12.469	23.905	40.835	1.936
van der Waals	236.112	-34.265	149.033	-56.897
1-4 Electrostatic	0	0	279.909	-49.006
Electrostatic	0	0	-782.345	35.394
Total Energy	2619.587	1771.33	618.262	245.111

Table 7. Lipid Bilayers Structural Constituents of the Different Systems Indicated in Figure 14. Fullerene type, Solution used for Solvation, Number of Lipid Residues, ions and water Molecules in each Bilayer System.

	$C_{80}(OH)_{42}$ LBL	C_{80} LBL	C_{80} LBL	C_{80} LBL	no C_{80} and derivative
Sol.	KCl	KCl	NaCl	$CaCl_2$	KCl
POPC	36448	36448	36448	36448	36448
DSPE	2128	2128	2128	2128	2128
CHOL	2368	2368	2368	2368	2368
Water	24438	24465	24420	24432	35007
Cation	20	20	20	20	30
Anion	20	20	40	20	30

IV.4.1 Equilibration and structural studies

IV.4.1.1 Root means square deviations (RMSD)

RMSD provides valuable information about two structures where the value is zero for identical structures, and increases as the two structures become more different [212]. As it is shown in Figure 16, the average RMSD for C_{80} and $C_{80}(OH)_{42}$ is 0.075 and 0.1 Å respectively and the average value remain almost constant throughout the simulation window. These, constant close to zero values from the beginning to the end of 20 ns simulation window, indicate that C_{80} as well as $C_{80}(OH)_{42}$ remain structurally stable within the lipid bilayers throughout the simulation time. The relatively larger RMSD (~0.025 Å) observed in the functionalized structure compared to the non-functionalized

counterpart could be due to OH functional groups which caused $C_{80}(OH)_{42}$ to have a relatively larger size and to show a relative structural change probably due to OH induced oscillations.

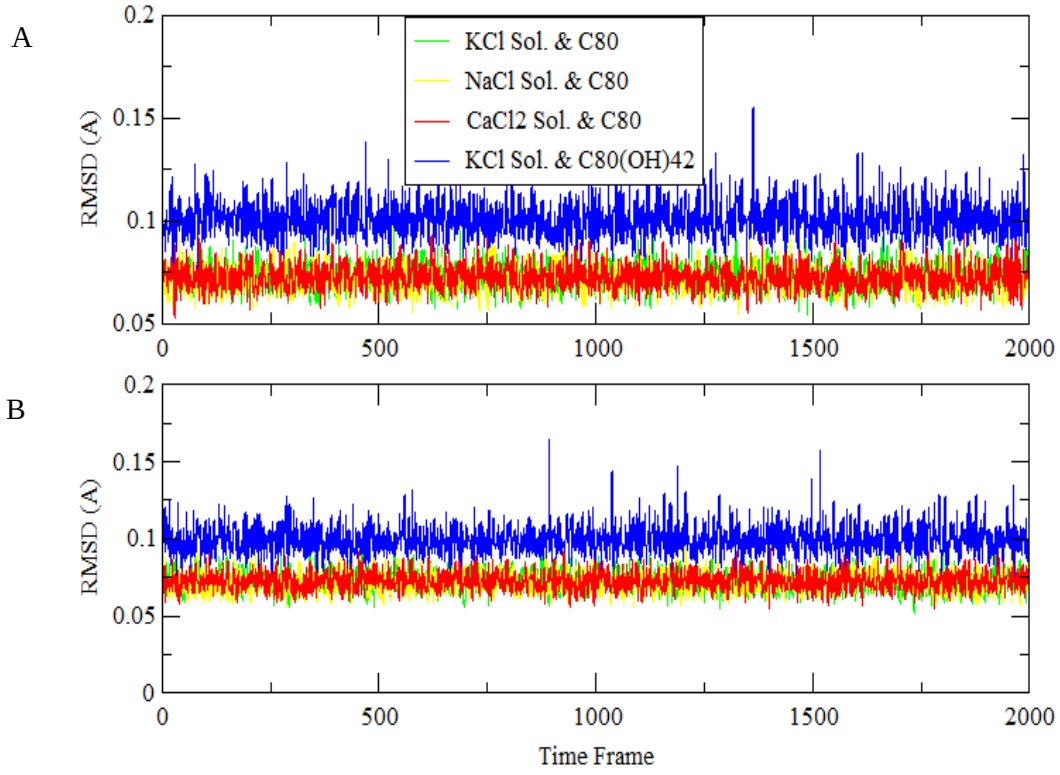

Figure 16. Avergae RMSD Plots of C_{80} and $C_{80}(OH)_{42}$ inside the LBLs. A) RMSD in the first 2000 time frames and (B) RMSD of the last 200 frames of the 20 ns simulation. The green line represents RMSD of C_{80} inside of a lipid bilayer immersed in KCl solution, RMSD of $C_{80}(OH)_{42}$ inside a lipid bilayer immersed in KCl solution is shown in blue, yellow line reperesent RMSD of C_{80} placed in a lipid bilayer that was immersed in NaCl solution and red line RMSD of C_{80} indie of lipid bilayer in $CaCl_2$ solution.

IV.4.1.2 Area per lipid (APL) and average thickness

APL is a crucial parameter which reflects lipid membrane properties, such as acyl chain ordering, compressibility, and molecular packaging. The time dependence of APL is also a good criterion to determine if a system has reached a steady state [213]. As shown in Figure 17 A, the APL for C_{80}\$C_{80}(OH)_{42}$-free and $C_{80}(OH)_{42}$ loaded lipid bilayers were similar from the beginning till the 20 ns simulations with a difference of about ~1.6%. This implies that, the presence of $C_{80}(OH)_{42}$ doesn't have any effect on the APL of POPC in the lipid bilayer. The APL of POPC in C_{80}-loaded lipid bilayer appears lower at the beginning but reaches to a 1.6% difference at later times in the simulation. The APL of DSPE is lower for C_{80} containing lipid bilayer immersed in KCl solution compared to C_{80} free and $C_{80}(OH)_{42}$ containing lipid bilayers in KCl solution for simulations conducted below 2 ns (Figure 17 B). These differences however become lower at later time of the simulation (Figure 17 B) which signifies the reorganization of the lipids to maintain the bilayer structure. Those observations are in accordance to the average thickness reported for the lipid bilayers (Figure 17 C) where the difference between $C_{80}(OH)_{42}$ containing and $C_{80}(OH)_{42}$-free bilayers was almost negligible throughout the simulation window. Comparing the APL of POPC in C_{80} loaded lipid bilayer immersed in monovalent versus divalent salt solutions indicate slight difference at the beginning of the simulation which may suggest lipid swelling in the latter. The APL difference between C_{80} containing bilayer in KCl solution and those immersed in NaCl and $CaCl_2$ was ~6%, observed within the first 2 ns, and this could be the cause for corresponding thickening of the bilayer resulting from the swelling of the lipids and these

results may signal a reorganization of the lipid bilayer at those simulation windows. While the difference in average thickness between $C_{80}(OH)_{42}$ containing and $C_{80}/C_{80}(OH)_{42}$ free LBLs is low (Figure 17 C), there was about 4 Å difference between C_{80} containing LBLs immersed in in NaCl and $CaCl_2$ solution from the $C_{80}/C_{80}(OH)_{42}$-free counterparts at the beginning of the simulation. These differences however, decreased as at a later time in the simulation (Figure 17 C).

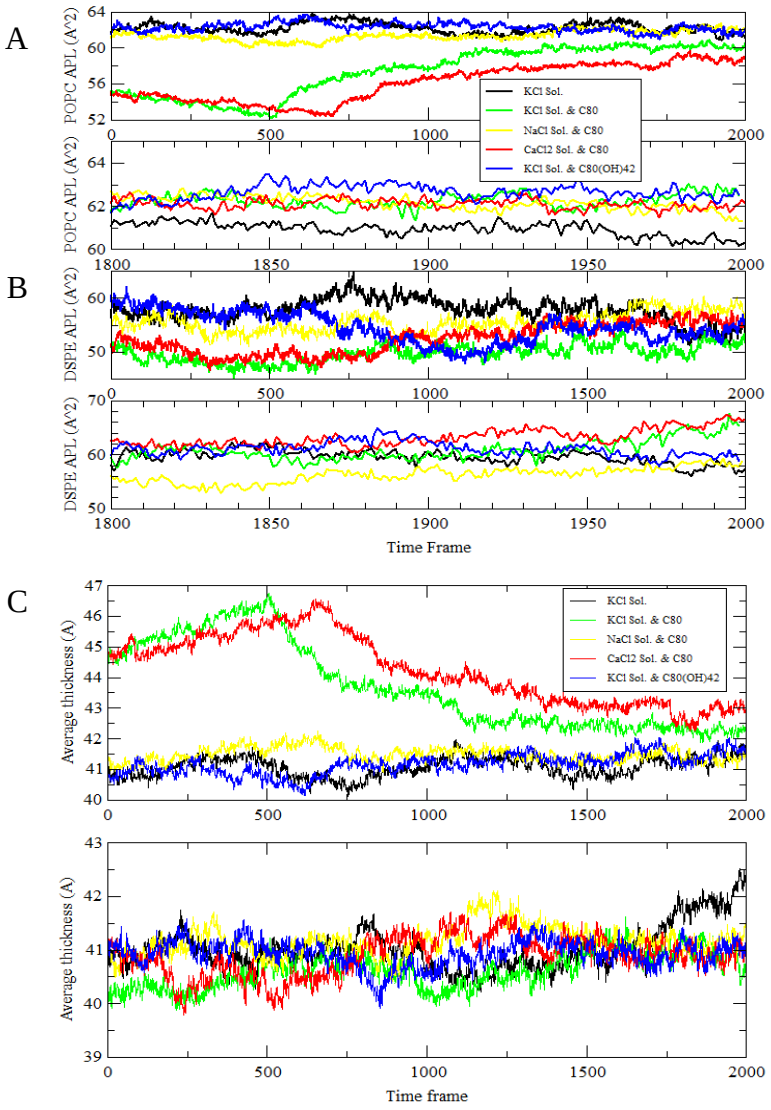

Figure 17. The Effect of C_{80}/$C_{80}(OH)_{42}$ on APL of POPC, DSPE and on the Lateral Average Lipid Bilayer Thickness (LBT) throughout the Simulation. A) APL of POPC where, the first 2000 frames are shown at the top and the last 2000 frames of the 20 ns simulation at the bottom. B) APL of DSPE where, the first 2000 frames are shown at the top and the last 200 frames of the 20 ns simulation at the bottom. C) Lateral average thickness of the LBLs.in the first 2000 and the last 2000 frames. Black, green, yellow, red and blue lines are designated for C_{80}/$C_{80}(OH)_{42}$ free lipid bilayer immersed in KCl solution, C_{80} containing lipid bilayer in KCl solution, C_{80} containing lipid bilayer in NaCl solution, C_{80} containing lipid bilayer in $CaCl_2$ solution and $C_{80}(OH)_{42}$ containing lipid bilayer in KCl solution respectively.

IV.4.1.3 Order parameter (SCD)

C_{80} as well as $C_{80}(OH)_{42}$ did not affect the overall carbon-deuterium order of Sn-1 & Sn-2 chains as depicted by insignificant SCDs difference between C_{80}/$C_{80}(OH)_{42}$-free LBL and C_{80}/$C_{80}(OH)_{42}$ containing LBLs (Figure 18). In general, the SCD values are higher close to the glycerol group and decreases towards the end of the tails (Figure 18). These values imply that the acyl chains of POPC and DSPE have a higher ordered in the head groups with a relatively less order towards the tail. These order parameter values are in agreement to those reported in [214].

The SCD of POPC in lipid bilayers depends on the percentage of CHOL incorporated into the LBLs [215]. In general, order parameter values in the Sn-1 and Sn-2 chains of POPC increase with the percentage of CHOL. For instance, a zero to 34 % incorporation of CHOL in a POPC + CHOL mixed bilayer was reported to increase the order parameter in the Sn-2 chain [215]. Therefore, a 1 to 1 comparison of the SCDs of POPC in lipid bilayers having different percentage of CHOL could mislead. However, as shown in Figure 18, SCD increase towards the head group, in both chains, and these values are in line to those reported in [215, 216]. Less symmetric SCD of DSPE compared to that of POPC could be due to the difference in phase transition between the two lipids where DSPE requiring a relatively higher temp (> 310 K). As the percentage of DSPE in the lipid bilayer structures is 5%, and as they are distributed throughout the membrane, the overall effect of DSPE could be insignificant. Considering the whole system, the SCD of the lipid bilayers containing C_{80} or $C_{80}(OH)_{42}$ is not different from the SCD of C_{80}-free lipid bilayer immersed in the same salt solution. Furthermore, the SCD

of C_{80} containing lipid bilayer is similar in different salt solutions. However, the SCDs of POPC located at < 40 Å, < 20 Å, <10 Å and < 5 Å from C_{80} indicated an intriguing result. The SCDs decrease as the lipids get closer to C_{80} (Figure 19). The local SCD decrement however is not significant enough to disturb the whole lipid bilayer system. On the other hand, lipids residing closer to $C_{80}(OH)_{42}$ never shown SCD variation as in the case of those residing closer to C_{80}. These results may imply that OH functionalization of C_{80} may have a positive effect in keeping the phase property of POPC.

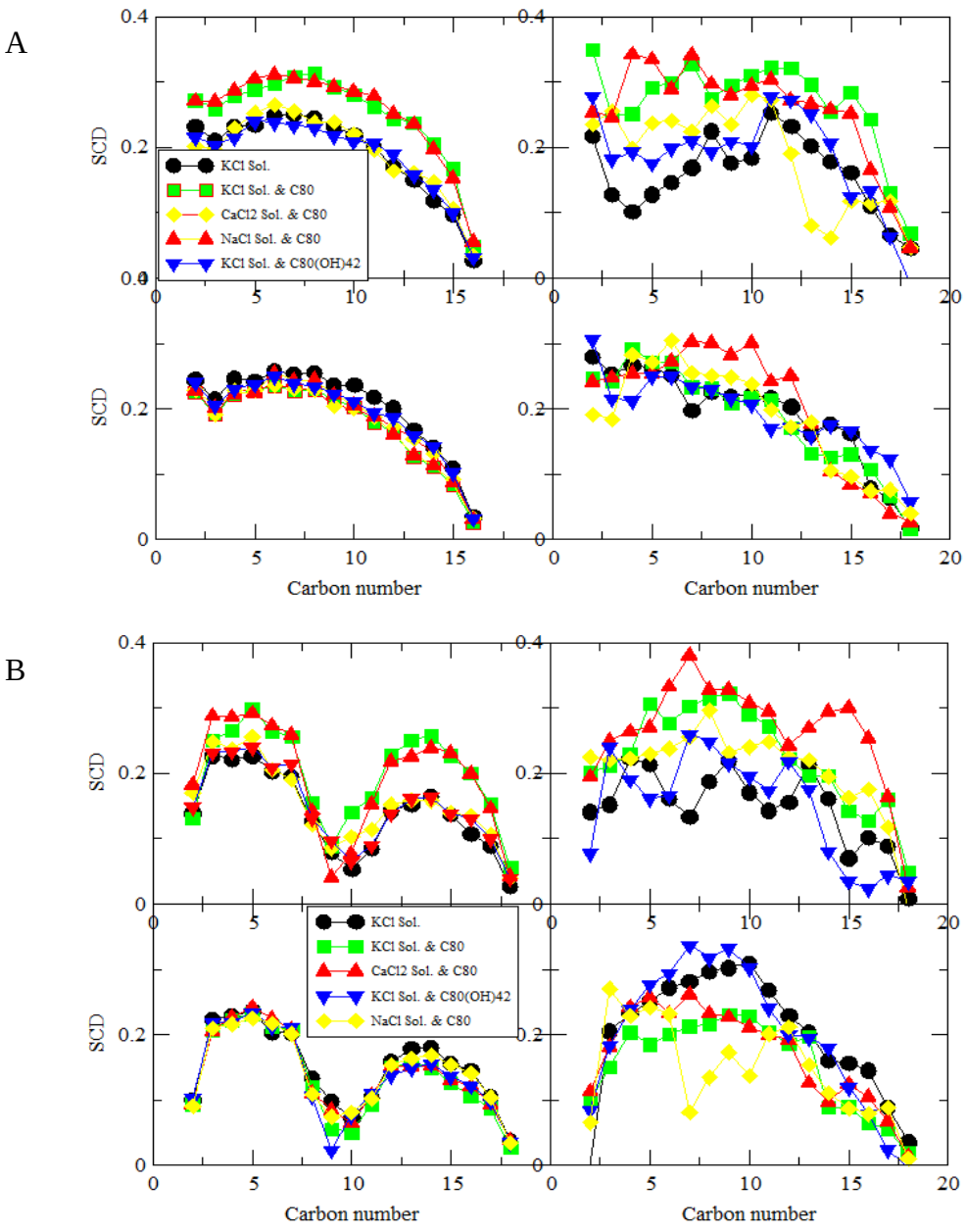

Figure 18. Simulated SCDs of POPC and DSPE to Study the Effect of C_{80}/$C_{80}(OH)_{42}$ on the Structural Stability of the Lipid Bilayers. Figure (A) SCDs along the Sn-1 chain and (B) SCD along Sn-2 chain. In each panel the SCD of POPC is shown on the left column and the SCD of DSPE is shown on the right. The top panels in each figure represent SCDs of the lipids at the beginning of the simulation and the bottom panels represent the SCDs after 20 ns simulation.

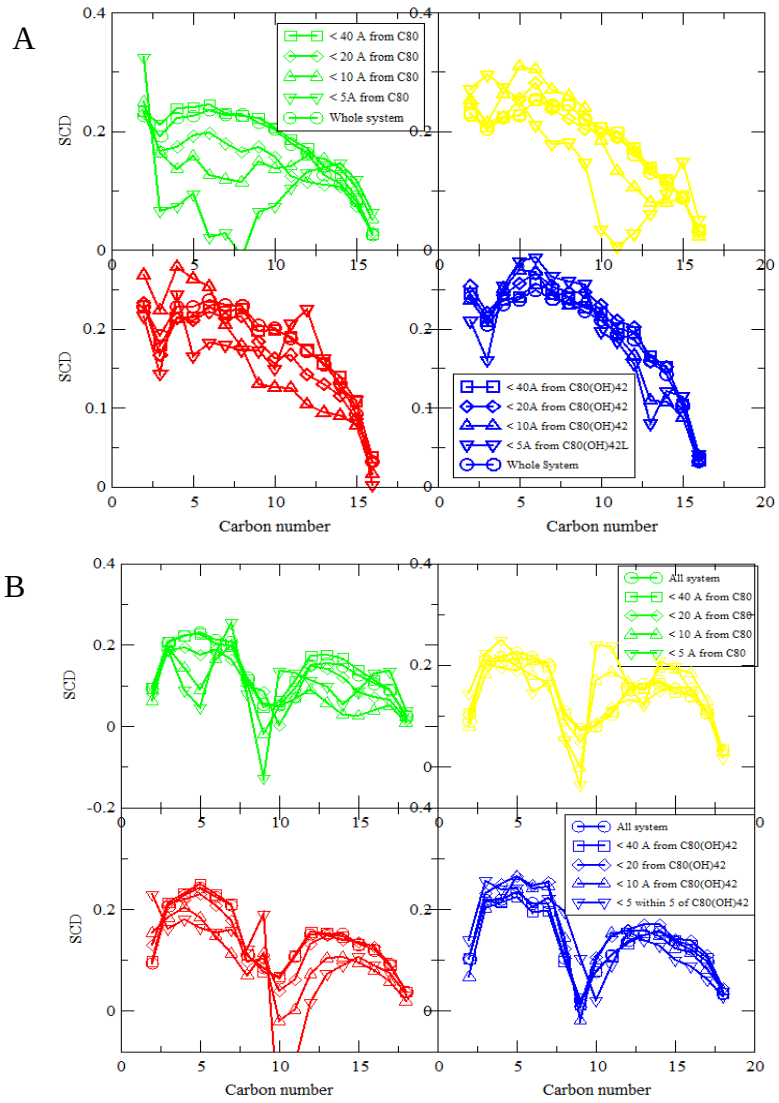

Figure 19. Simulated Carbon Deuterium SCD of POPC in the Presence of 10% of CHOL and 5% DSPE to Study the Effect of C_{80}/$C_{80}(OH)_{42}$ on Local Lipids. The panels represent (A) SCD along the Sn-1 chain and (B) Sn-2 chain. SCDs labeled in circle represent SCD of the whole system, SCD of lipids within 40 Å from C_{80}/$C_{80}(OH)_{42}$ (square), < 20 Å (diamond), < 10 Å (upward triangle) and < 5 Å (inverted triangle). The SCD simulations are conducted taking the last 50 frames of the 20 ns simulation.

IV.4.1.4 Number density profiles (NDP)

To assess the effect of local lipid SCD change on the overall stability of the system, the next strategy was to study water percolations, ion displacements and the localization of lipids. For this purpose, the number density of water, ions and lids is investigated (Figure 20). The width of a zero water number density region is in accord to the average thickness reported in Figure 17 and the lipid bilayers were stable enough to preclude water from entering as shown in the NDPs simulated in the beginning and at the end of 20 ns simulations. Similarly, the ions remain outside of the lipid bilayer throughout the simulation period for $C_{80}/C_{80}(OH)_{42}$ loaded as well as $C_{80}/C_{80}(OH)_{42}$ free lipid bilayers (Figure 20). In other words, no cations as well as anions were observed within the lipid bilayer (-20 to 20 Å vertical distance) throughout the simulation time windows (Figure 20). This indicates that, loading the membranes with $C_{80}/C_{80}(OH)_{42}$ doesn't affect lipids arrangement as well as it doesn't cause the ions/water to percolate deep into the lipid bilayer through the SCD compromised lipids situated closer to the molecules (Figure 20, Figure 21). From these ion distribution profiles, it is also evident that calcium, potassium and sodium ions seem to be strongly bound to the water side shown by a higher ions density closer to the lipid head group compared to the distribution in the hydrophobic region (Figure 20). These observations accord the information conveyed by POPC, DSPE and CHOL number density profiles indicated in Figure 21. In the region where the water density is zero, POPC, DSPE and CHOL number density is high and vice versa. These observations are similar for $C_{80}/C_{80}(OH)_{42}$ loaded and $C_{80}/C_{80}(OH)_{42}$ free lipid bilayers. Furthermore, there is no difference in water permeation,

ions percolation or lipid arrangement in C_{80} containing lipid bilayers attributed to the type of salt solutions used for solvation.

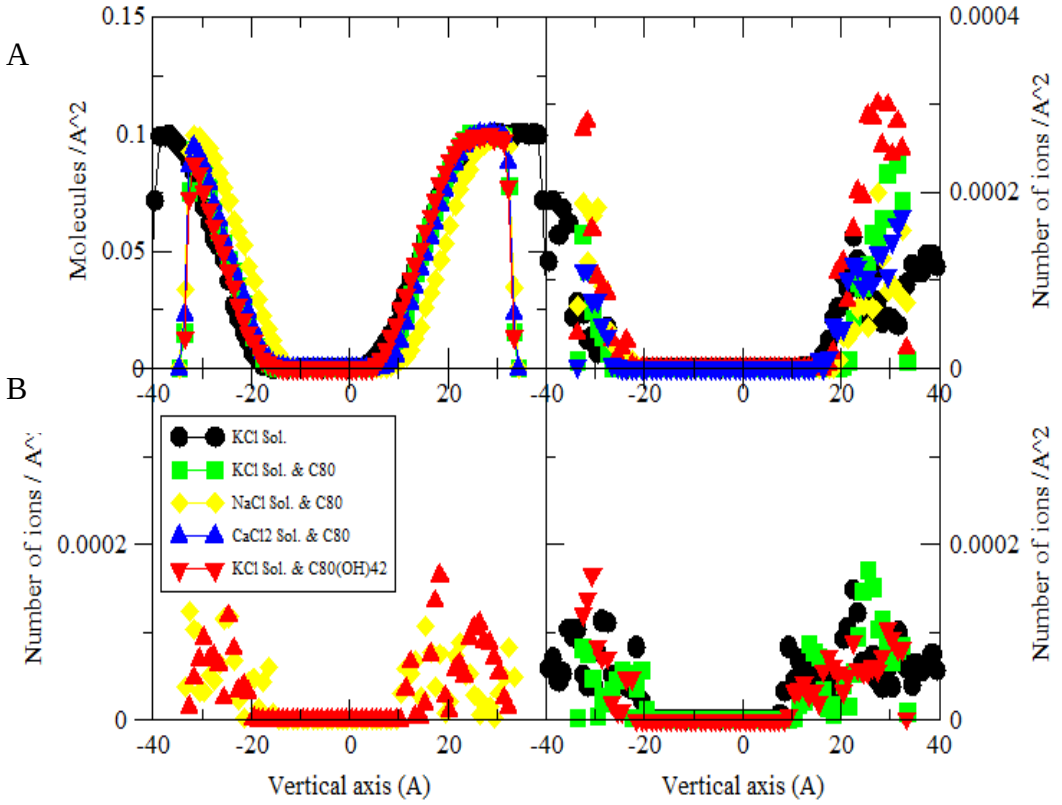

Figure 20. Water and ions Number Density Profiles to Study if C_{80}/$C_{80}(OH)_{42}$ Disrupt the Lipid Bilayer Structural Integrity. Or if the Interaction of Ions with the Lipid Bilayer Head Groups induce Percolation of ions/water into the Lipid Bilayers. A) Water (left) and chloride ions (right) number densities. B) Sodium & calcium (left) and potassium (right) number densities. The profiles are averages of the last 200 frames of 20 ns simulations. Black lines/points represent C_{80}/$C_{80}(OH)_{42}$ free lipid bilayer in KCl solution, green lines/points represent C_{80} containing lipid bilayer in KCl solution, yellow lines/points represent C_{80} containing lipid bilayer in NaCl solution, red lines/points are C_{80} containing lipid bilayer in $CaCl_2$ solution and blue lines/points represent $C_{80}(OH)_{42}$ containing lipid bilayer in KCl solution.

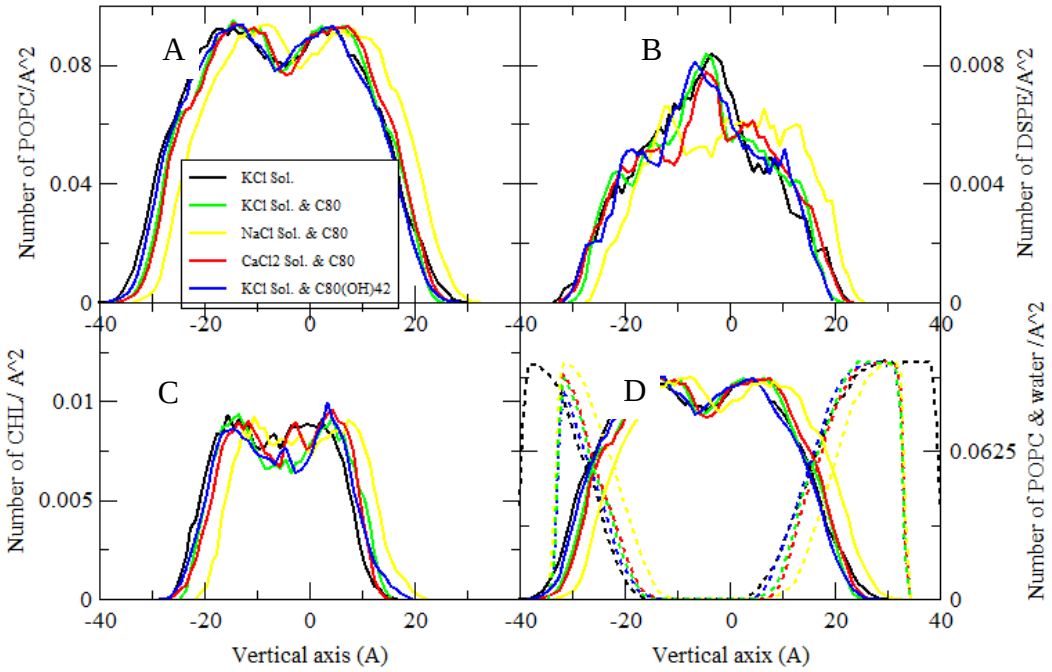

Figure 21. NDP of POPC, DSPE and CHOL to Study the Effect of $C_{80}/C_{80}(OH)_{42}$ on the Stability of the Hydrophobic Region of the LBL. The profiles are, A) POPC, B) DSPE, C) CHOL and D) POPC & water combined. Black, green, yellow, red and blue lines respectively represent $C_{80}/C_{80}(OH)_{42}$ free LBL in KCl solution, C_{80} containing LBL in KCl solution, C_{80} containing LBL in NaCl solution, C_{80} containing LBL in $CaCl_2$ solution and $C_{80}(OH)_{42}$ containing LBL in KCl solution respectively.

IV.4.2 Assessing the stability of $C_{80}/C_{80}(OH)_{42}$ LBLs in physiological salt solutions

IV.4.2.1 Radial distribution functions (RDF)

RDF analysis to investigate the effect of $C_{80}/C_{80}(OH)_{42}$ on the localization of K^+, Na^+ and Ca^{++} around phosphate head groups in POPC indicated a relatively higher cations accumulation around 3.8 Å from the phosphorus in POPC. This peak position remains the same for $C_{80}/C_{80}(OH)_{42}$ free lipid bilayer as well as for those C_{80} and $C_{80}(OH)_{42}$ containing LBLs (Figure 22). These results imply that the presence of either of the molecules didn't affect the interaction of POPC phosphate groups with K^+, Na^+ as

well as with Ca^{++}. While the cations start to assemble > 4 Å from the nitrogen in the lipid head groups, there is no difference on the localization or on the number of K^+ around nitrogen between $C_{80}/C_{80}(OH)_{42}$ containing and $C_{80}/C_{80}(OH)_{42}$-free LBLs immersed in the same solution (Figure 22). The Cl^- are localized around 4.5 Å from nitrogen of POPC in all the systems. The higher RDF amplitude observed for the lipid bilayer immersed in $CaCl_2$ solution could be due to the excess Cl^- present in $CaCl_2$ solution compared to the number of Cl^- present in KCl and NaCl solutions. To sum up, the cations and anions distribution around phosphate and nitrogen head groups in POPC remains almost similar in $C_{80}/C_{80}(OH)_{42}$ containing and $C_{80}/C_{80}(OH)_{42}$ free lipid bilayers.

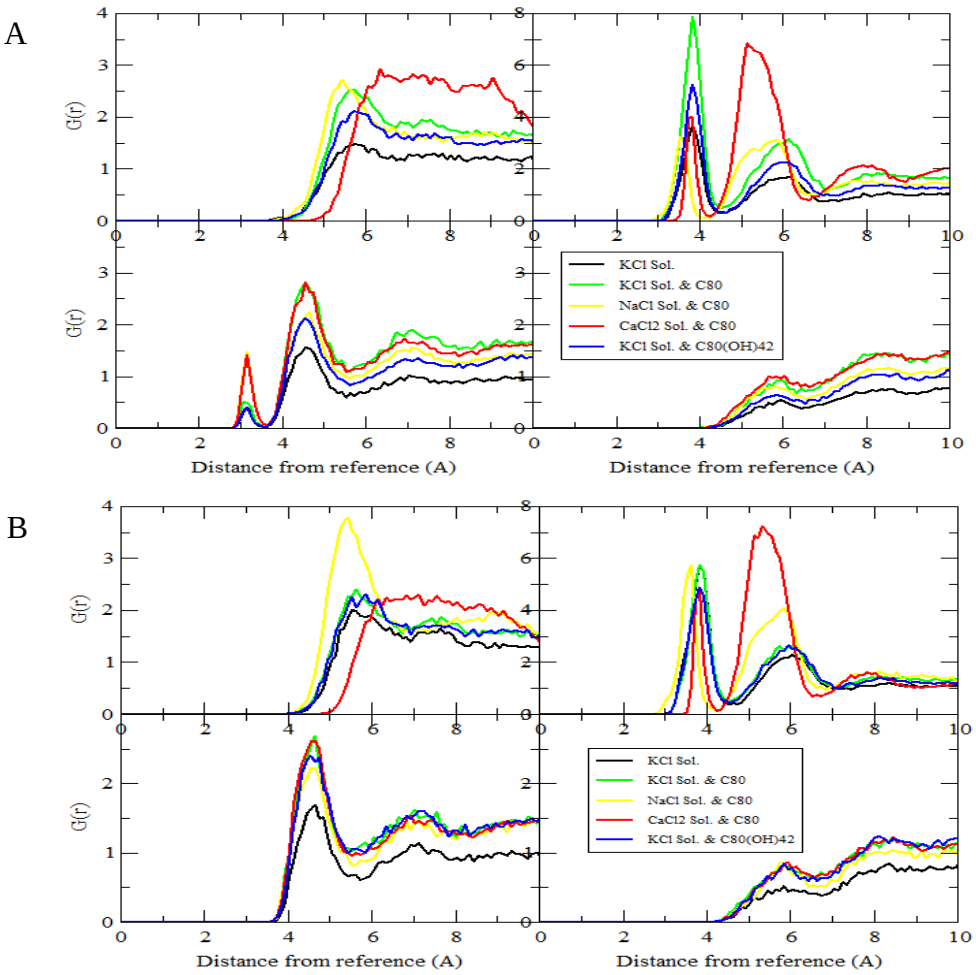

Figure 22. Radial Distribution Function of Cations and Anions with Respect to the Lipid Head Groups. The simulations are taken at the Beginning (A) and end of 20 ns simulations (B) to investigate the effect of C_{80}/$C_{80}(OH)_{42}$ on ions distributions and to study the stability of POPC, DSPE and CHOL containing LBLs in physiological salt solutions. The top panels of each figure constitute the distribution of cations with respect to N in POPC (left) and with respect to P of POPC (right). Cl^- distribution with respect to N of POPC (left) and with respect to P of POPC (right) are shown at the bottom. Black, green, yellow, red and blue lines represent the RDF of K^+ in C_{80}/$C_{80}(OH)_{42}$ free LBL immersed in KCl solution, K radial distribution in C_{80} containing LBL immersed in KCl solution, RDF of Na^+ in C_{80} containing lipid bilayer in NaCl solution, Ca^{++} RDF in C_{80} containing LBL immersed in $CaCl_2$ solution, and K^+ RDF in $C_{80}(OH)_{42}$ containing LBL immersed in KCl solution respectively.

IV.4.2.2 Lipid interdigitation and bilayer thickness (LI & LBT)

In optimally stable lipid bilayer structure, the distance between the two lamellae (leaflets) remains constant. However, in non-stable or compromised lipid bilayer the structures could be disturbed and the lipids in each leaflet may cross or subject to interdigitation. For instance, in a ripple and fluid phases lamellae the phase transition induces thinning and inter-leaflet interdigitations [217]. From the leaflet overlap and fraction of atoms in contact shown in Figure 23, one can see that there is no much difference on the degree of overlap between the leaflets among $C_{80}/C_{80}(OH)_{42}$ containing and $C_{80}/C_{80}(OH)_{42}$ free lipid bilayers. It is evident, however, that the degree of leaflet overlap as well as fraction of atoms in contact remains more equivalent in $C_{80}(OH)_{42}$ containing lipid bilayer and $C_{80}/C_{80}(OH)_{42}$ -free bilayer compared to those C_{80} containing counterparts. However, in all the lipid bilayers there was no abrupt change in leaflet overlap that signify separation of leaflets or extreme interdigitation. These results imply that the lipid bilayers demonstrated stable and ordered assembly for all the simulation time windows considered. In other words, the $C_{80}/C_{80}(OH)_{42}$ molecules have never induced lipid interdigitation as well as a perturbation that could affect the structural stability of the bilayers.

A 3D thickness map of a lipid bilayer devoid of $C_{80}/C_{80}(OH)_{42}$ indicates about 10 Å variations (Figure 24). Thickness variations in $C_{80}/C_{80}(OH)_{42}$ containing lipid bilayers are also within the same range (Figure 24, Figure 25). Relatively thicker or thinner patches (~4 Å thicker from average) were observed in all the lipid bilayers irrespective of the type of molecule loaded or the salt solutions. The relative thickenings were thought to

be related to the localization of CHOL as reported in [218] where CHOL had increased the thickness of 1,2 dimyristoleoylphosphatidylcholine (diC14:1PC) bilayers by 0.54 ± 0.03 nm. Nevertheless, the thick layer patches in this study seem to be unrelated to the localization of either CHOL, DSPE or C_{80}/$C_{80}(OH)_{42}$ (Figure 24, Figure 25). Furthermore, the localization of C_{80} seems to be unrelated to the type of solution that the bilayers are immersed in (Figure 26).

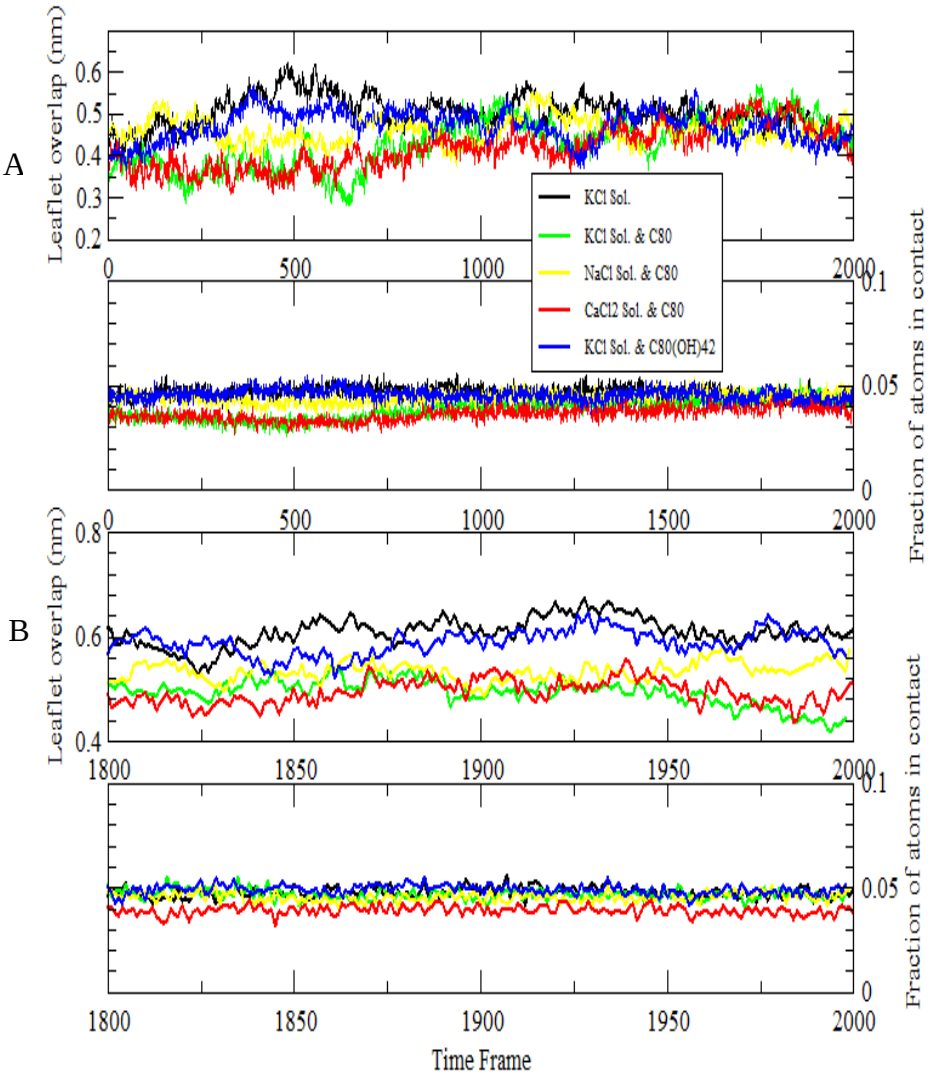

Figure 23. The Effect of C_{80}/$C_{80}(OH)_{42}$ on Lipid Interdigitation of POPC, DSPE and CHOL Containing Lipid Bilayer Immersed in Different Physiological Salt Solutions. A) Correlation based leaflet overlap (in nm) and the fraction of LBL atoms in contact calculated for the first 2000 frames and (B) the last 200 frames of the 20 ns simulation. Black, green and blue lines represent lipid interdigation level of C_{80}/$C_{80}(OH)_{42}$ free lipid bilaye, C_{80} containing lipid bilayer, and $C_{80}(OH)$ containing lipid bilayer all immersed in KCl solution respectively. Yellow and red lines represnet C_{80} conatining lipid bilayers immersed in NaCl solution and $CaCl_2$ solution respectively.

IV.4.2.3 Localization and dynamics of C_{80}/$C_{80}(OH)_{42}$ in the lipid bilayer

Investigating the localization of C_{80}/$C_{80}(OH)_{42}$ within the lipid bilayer is important for it hints the possible interactions of these molecules with different lipid components. It was previously reported that the preferred localization of the non-hydrophobic C_{60} within DMPC lipid bilayer to be off the center [219]. As shown in Figure 24, the localization of C_{80} inside a lipid bilayer immersed in KCl solution, accords the reports in [219] where C_{80} was displaced towards the lipid head groups during the simulation. As in the case of C_{80}, $C_{80}(OH)_{42}$ was also displaced towards the lipid head group (Figure 25). The displacement of $C_{80}(OH)_{42}$ as well as its proximity towards the head groups however never induced structural change on the overall bilayer structure as confirmed by the SCDs reported in section 3.1 and this result generally accords the reports in [196]. Further, the closeness of $C_{80}(OH)_{42}$ towards lipid head groups never induced lipid interdigitation or leaflet separation (Figure 23) and it didn't affect the distribution of water and ions around the head groups (Figure 21). The absence of structural change due to lipid oxidation in C_{80} containing bilayers, contrary to previous report where C_{60} was reported to cause such effect, could be either due to the chain differences between DMPC and POPC or could be due to the presence of different lipids in this study. CHOL might have increased the order of POPC which in turn help resist any structural change that C_{80} would have instigated. Furthermore, there is no considerable difference on the localization of the molecules resulting from the type of salt solution in which the bilayers are immersed (Figure 26).

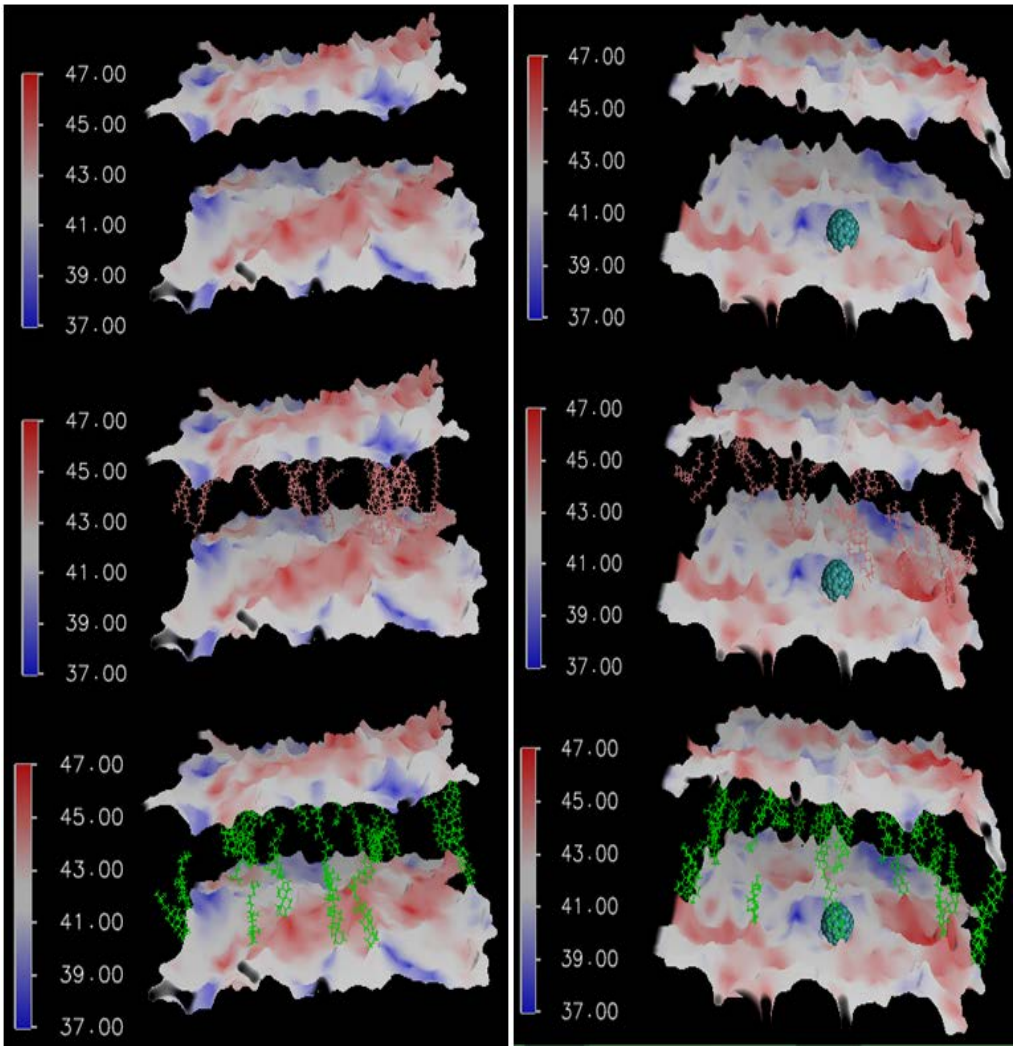

Figure 24. The Localization of C_{80} inside Lipid Bilayer Immersed in KCl Solution after 20 ns Simulation Window. A lipid bilayer free of C_{80} is shown on the left column and on the right C_{80} containing lipid bilayer. The figures from top to bottom represent, the localization of C_{80} off the center closer to lipid head group, localization of CHOL and the localization of DSPE inside the lipid bilayer respectively. The lipid bilayers are drawn on black-white-red (BWR) color scale to investigate if lateral bilayer thickness relates to the localization of C_{80}, CHOL or DSPE. From the figures it is evident that C_{80} never induced thickening or thinning of the lipid bilayer in 0.15 M KCl solution.

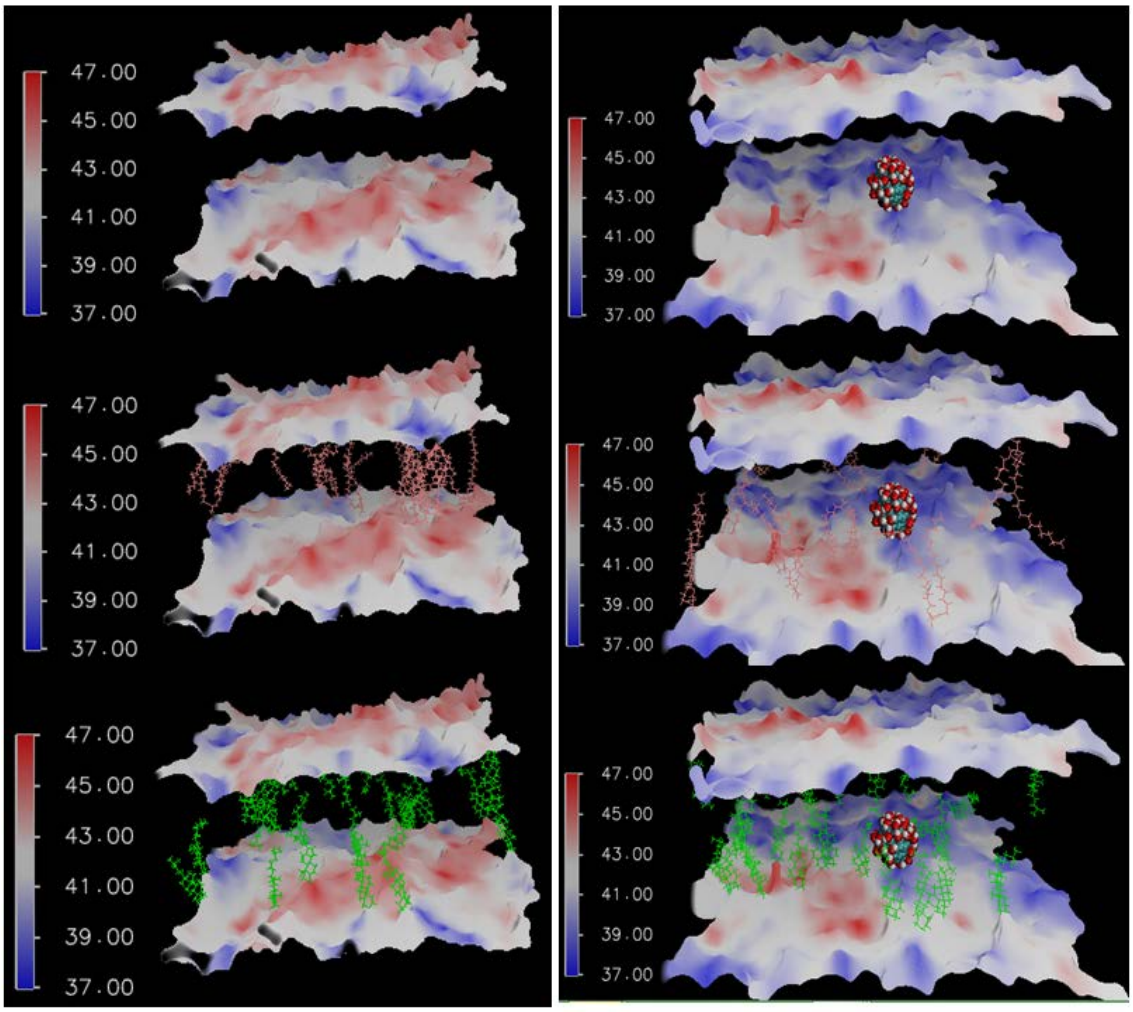

Figure 25. The Localization of $C_{80}(OH)_{42}$ inside Lipid Bilayer Immersed in KCl Solution after 20 ns Simulation Window. A lipid bilayer free of $C_{80}(OH)_{42}$ is shown on the left column and on the right $C_{80}(OH)_{42}$ containing lipid bilayer. The figures from top to bottom represent, the localization of $C_{80}(OH)_{42}$ off the center closer to lipid head group, localization of CHOL and the localization of DSPE inside the lipid bilayer respectively. The lipid bilayers are drawn on BWR to investigate if lateral bilayer thickness change relates to the localization of $C_{80}(OH)_{42,}$ CHOL or DSPE. From the figures it is evident that $C_{80}(OH)_{42}$ never induced thickening or thinning of the lipid bilayer in 0.15 M KCl solution.

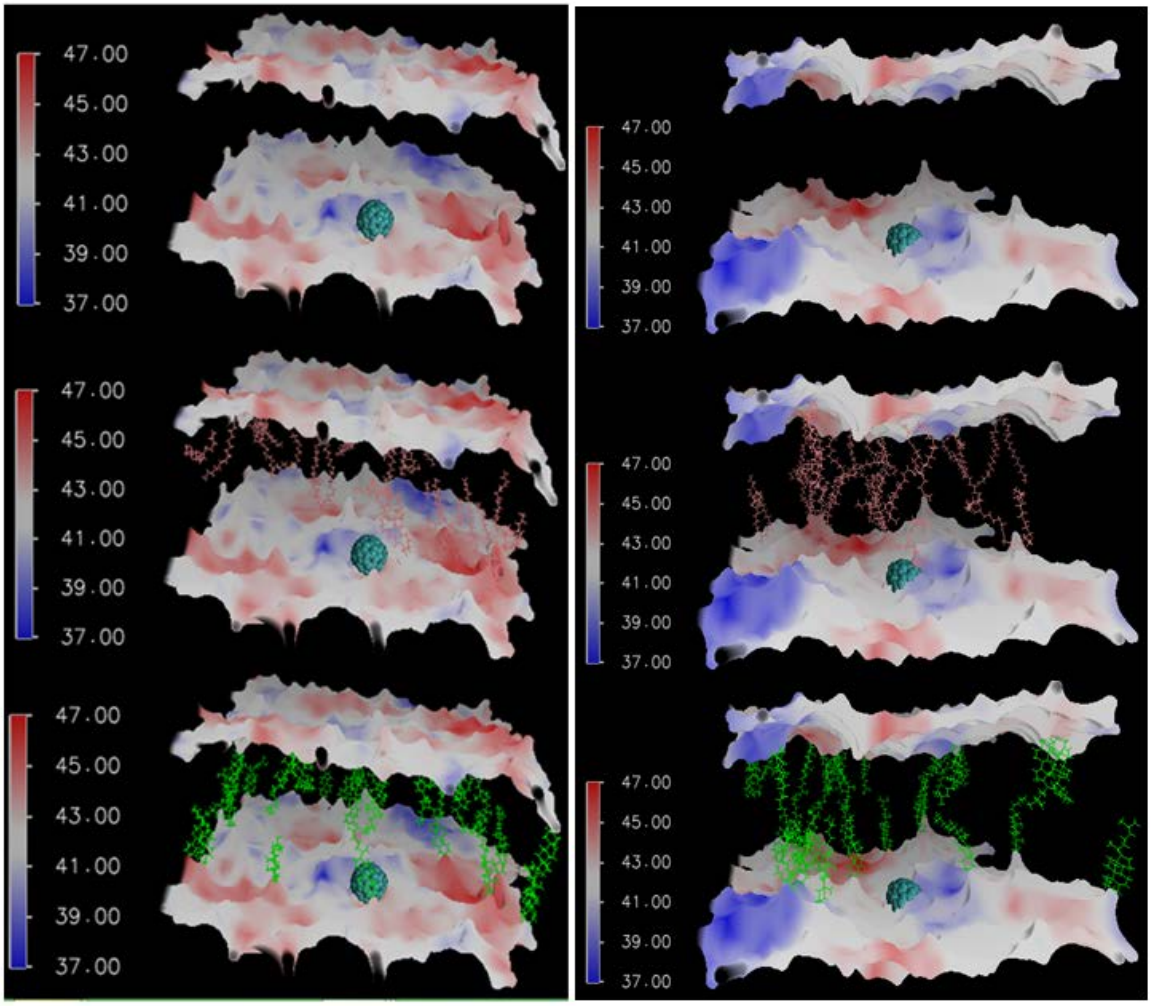

Figure 26. Comparison of the Localization of C_{80} inside Lipid Bilayer Immersed in KCl and $CaCl_2$ Solutions after 20 ns Simulation Window. A lipid bilayer containing C_{80} in KCl solution is shown on the left column and on the right, C_{80} containing lipid bilayer in $CaCl_2$ solution. The figures from top to bottom represent, the localization of C_{80} off the center closer to lipid head group, localization of DSPE and the localization of CHOL inside the lipid bilayers respectively. The lipid bilayers are drawn on BWR color scale to indicate if a change in bilayer thickness is related to the localization of C_{80}. As in the case of KCl Solution, it is evident that C_{80} never induced thickening or thinning of the lipid bilayer solvated in 0.15 M $CaCl_2$ solution. However, the thinning on the lipid bilayer in $CaCl_2$ compared to the on in KCl solution could be attributed to Ca^{++}.

IV.4.3 Steered Molecular Dynamic Simulation (SMD)

The purpose of the SMD was to compare the amount of forces needed to displace C_{80} versus $C_{80}(OH)_{42}$ across the different regions of the lipid bilayers and then understand the stability of the particles inside the LBLs through energy computations. The displacements of the particles in non-restrained simulation are portrayed in Figure 27 & Figure 28 and corresponding displacement trajectory videos are provided as supplementary materials. The energy computations revealed that more energy was required to drive $C_{80}(OH)_{42}$ out of the LBL structure compared to the amount of energy required to displace C_{80} out (Figure 29). As the steered molecular dynamic simulations were conducted at a very low velocity (0.0001 Å/timestep), the process is considered reversible. Therefore, the total energy required to displace the molecules along a complete LBL trajectory is twice of the energy required for half of the course. Furthermore, the energy required to move a molecule at two trajectories taken 1250 frames apart look identical (Figure 29).

To study the combined effect of ions and lipids on the dynamics of C_{80}, the dynamics of C_{80} inside LBLs immersed in KCl, NaCl and $CaCl_2$ solutions is explored (Figure 29, Figure 30). The relatively higher energy required to move C_{80} inside LBL in NaCl solution compared to the energy required to displace it inside the LBL in KCl solution could be due to a stronger localization or interaction of Na^+ with phosphorus or other atoms in POPC compared to the localization and interaction of K^+ around the same atoms (Figure 22 lower panel). A firm interaction between Na^+ and POPC might have helped a higher order lipid arrangement resulting in a stronger contact/friction between

C_{80} and POPC. This is also supported with the change in SCD of the lipids residing closer to C_{80} which was more pronounced in the LBL immersed in KCl solution compared to the LBL in NaCl solution (Figure 19). Similarly, higher energy was required to move C_{80} within the lipid bilayer immersed in the $CaCl_2$ solution (Figure 30). To sum up, the differences in the amount of energy required to displace C_{80} inside of LBLs immersed in different salt solutions could be mainly due to the interactions between the ions and POPC.

Although the major causes for the higher energy requirement to move $C_{80}(OH)_{42}$ inside the lipid bilayer is uncertain, hydroxyl functionalization, differences in electrostatic energy of the molecules, and SCD differences of the lipids residing closer to the molecules could be some of the factors. To assess the OH functionalization effect, the amount of energy required to move the two molecules in the bulk solution was evaluated (Figure 30). This computation revealed that more energy is needed to displace $C_{80}(OH)_{42}$ inside the bulk solution which most likely is due to a hydrogen bonding between the OH in functionalized C_{80} and surrounding water molecules. To assess if similar phenomenon contributed for the higher energy requirement to displace $C_{80}(OH)_{42}$ inside the lipid bilayer, hydrogen bonds formed between $C_{80}(OH)_{42}$ and POPC are evaluated using VMD's HBonds plugin [206] by setting a 3 Å donor-acceptor distance and 20 degrees' angle cut-off. As shown in Figure 30, new hydrogen bonds start to immerge after 1-3 nm simulation windows. Hence, the energy required to move $C_{80}(OH)_{42}$ needs to have additional energy to break the new hydrogen bonding in addition to the energy required to move C_{80}. This is also supported by the shifting in the magnitude of the energy

required to move $C_{80}(OH)_{42}$ inside KCl bulk solution compared to the energy required to move C_{80} (Figure 30). The energy required to move C_{80} in KCl and $CaCl_2$ solutions became almost constant, Figure 30, while the energy required to move $C_{80}(OH)_{42}$ increases inside the bulk solution due to hydrogen bonding of the later with water.

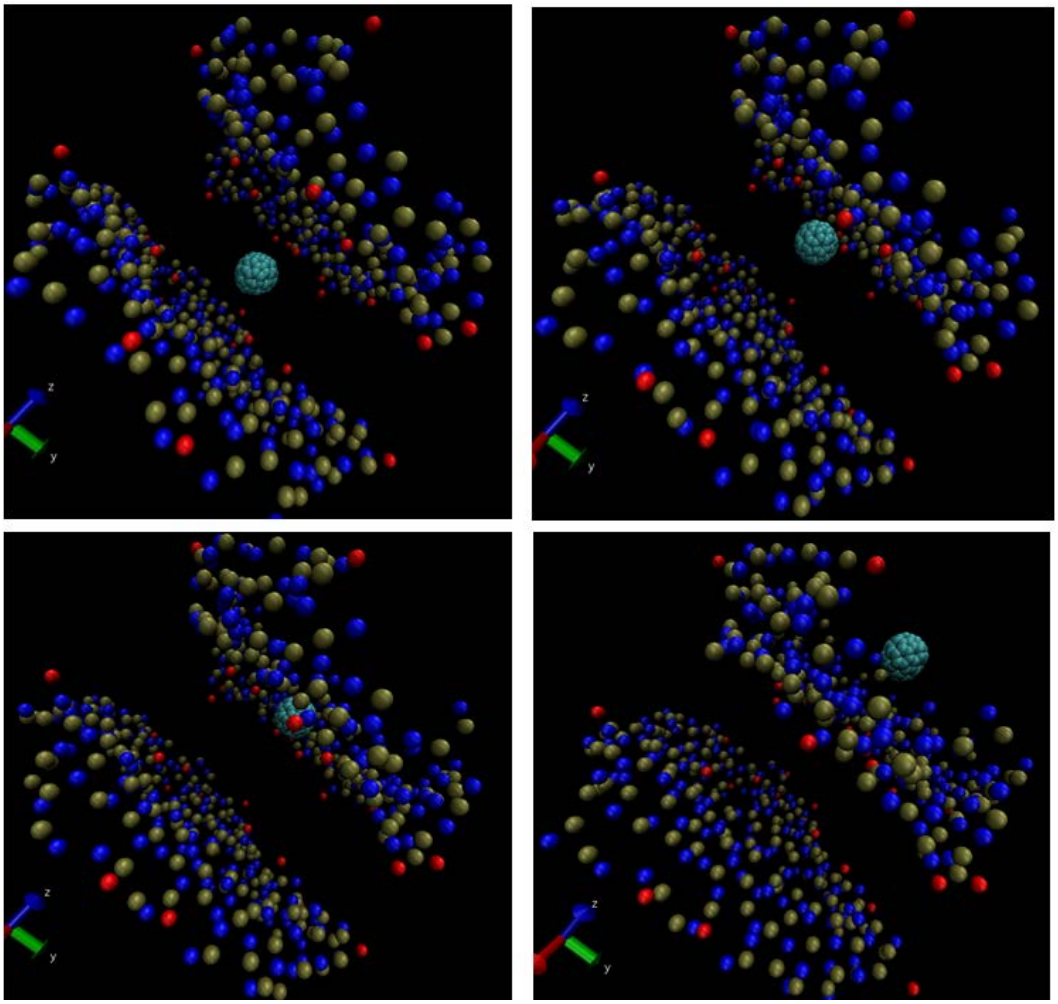

Figure 27. Steered Molecular Dynamic Simulationto to Study the Dynamics of C_{80} Inside of a Lipid Bilayer Immersed in KCl Solution. The trajectories are taken at different time frames to indicate C_{80} crossing different regions of the lipid bilayer. Beginning of the trajectory indicated on the top-left and the molecule emerging out of the lipid bilayer shown on the bottom-right. Blue, green and red points represent phosphorus, nitrogen and oxygen atoms constituting the lipid bilayer.

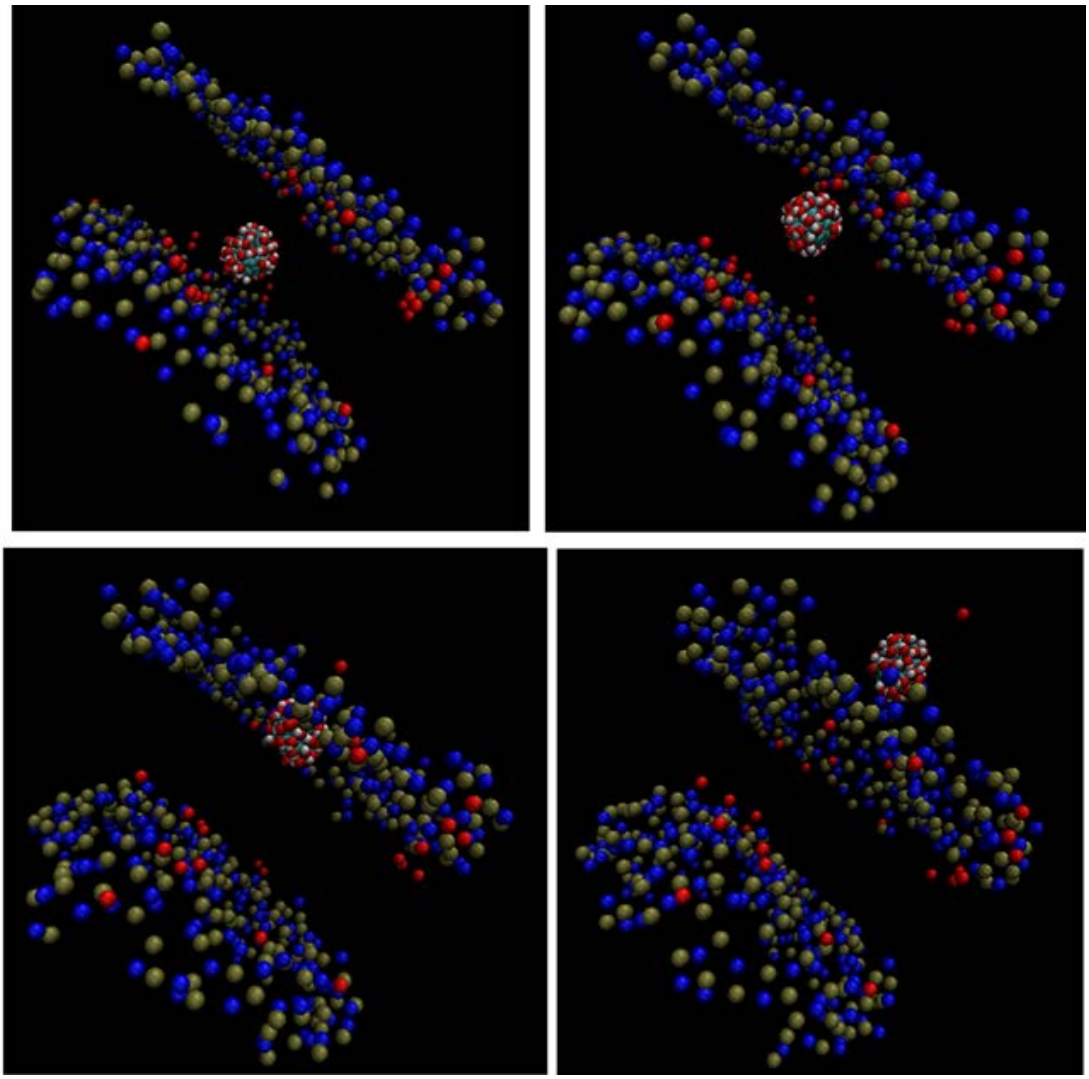

Figure 28. Steered Moleculard Dynamic Simulation to Study the Dynamics of $C_{80}(OH)_{42}$ Inside a Lipid Bilayer Immersed in KCl Solution. The tajectories are taken at different time frames to indicate $C_{80}(OH)_{42}$ crossing different regions of the lipid bilayer. Beginning of the tajectory is indicated on the top-left and the molecule emerging out of the lipid bilayer on the bottom-right. Blue, gren and red points represent P, N and oxygen atoms constituting the lipid bilayer. The functionalization of C_{80} with OH is shown using red/white points portraying hydrogen & oxygen atoms attached to C_{80}.

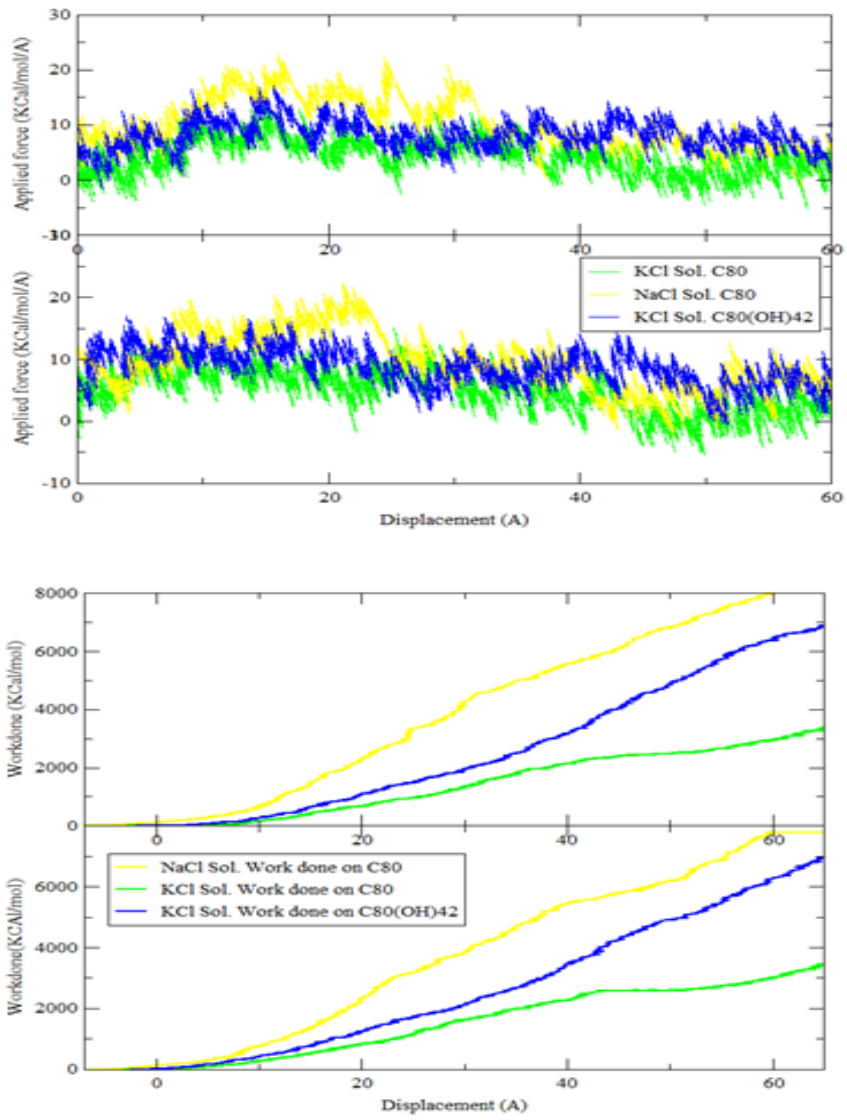

Figure 29. Applied Force Profiles for the Trajectories of C_{80} and $C_{80}(OH)_{42}$ to Cross the Different Regions of the Lipid Bilayers and the Energy Required to Move the Molecules along the Trajectory at 750 (top) & 2000 (bottom) Time Frames. In the top panel, green profiles represent forces applied to move C_{80} inside LBL immersed in KCl solution, the yellow profiles represent applied force to move C_{80} inside LBL immersed in NaCl solution and blue profiles represent the force to move $C_{80}(OH)_{42}$ inside LBL immersed in KCl solution. Same color representations are used to indicate the energy required to move C_{80} & $C_{80}(OH)_{42}$ across LBL immersed in KCl, NaCl and $CaCl_2$ solutions (bottom panel).

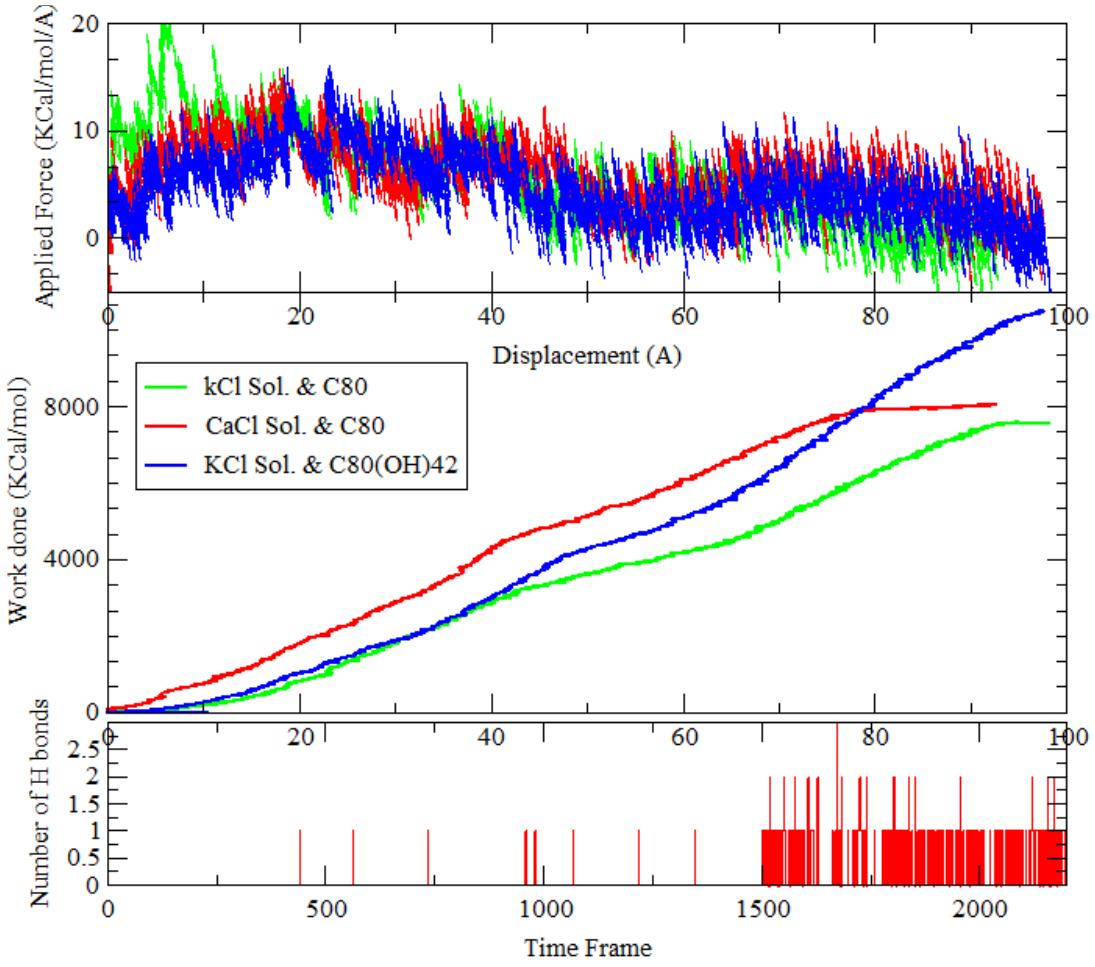

Figure 30. Steered Molecular Dynamics Simulation of C_{80} & $C_{80}(OH)_{42}$ Inside of Lipid Bilayers Solvated using Physiological Salt Solutions. The panels are applied force versus displacement (Kcal/mol/A) shown on the top, energy required to displace C_{80} & $C_{80}(OH)_{42}$ across the different regions of the lipid bilayers (middle) & the number of new hydrogen bonds developed between $C_{80}(OH)_{42}$ & POPC (bottom). Green, red and blue lines represent C_{80} containing LBL in KCl solution, C_{80} containing LBL inCaCl2 solution and $C_{80}(OH)_{42}$ containing LBL in KCl solution respectively. The more work required to displace $C_{80}(OH)_{42}$ over C_{80} across the lipid bilayers are associated to the new hydrogen bonds developed between $C_{80}(OH)_{42}$ and POPC at later time in the simulations. Furthermore, the work required to displace C_{80} in a lipid bilayer immersed in divalent solution (CaCl2 solution) is higher than displacing it inside a lipid bilayer immersed in monovalent solution (KCl solution).

IV.5 Conclusions

Gd-fullerene is a widely researched MRI contrast agent, but the details of its dynamics in liposomal lipid bilayers remain poorly understood. This chapter investigated the structural stability of $C_{80}/C_{80}(OH)_{42}$ containing lipid bilayers immersed in different physiological salt solutions. The structural stability of $C_{80}/C_{80}(OH)_{42}$ containing lipid bilayers immersed in different physiological salt solutions was investigated and the results indicated that while lipids residing closer (< 20 Å) to C_{80} were shown to have a decreased SCD, those residing closer to $C_{80}(OH)_{42}$ remain stable. The local SCD change in, C_{80} loaded bilayers, however didn't affect the overall stability of the bilayers. Density profiles of water, K^+, Na^+, Ca^{++}, Cl^-, POPC, DSPE and CHOL at different simulation windows indicated that C_{80} as well as $C_{80}(OH)_{42}$ did not affect the structural stability of the lipid bilayers for simulations conducted up to 20 ns as supported by water impermeability or similarity in the localization of cations, anions or lipids. These observations are also in line with lipid interdigitation analysis where no significant differences are observed in leaflet overlap or lipid interdigitation between $C_{80}/C_{80}(OH)_{42}$ containing and $C_{80}/C_{80}(OH)_{42}$ free LBLs throughout the simulation. The SMD computations revealed that a higher energy is required to displace $C_{80}(OH)_{42}$ across POPC, CHOL and DSPE containing LBL in KCl solution compared to the energy required to displace C_{80} across the same trajectory. Tow possible reasons may attribute to the higher energy need to displace $C_{80}(OH)_{42}$ compared to C_{80}. First, it could be due to the higher SCD of lipids residing closer to $C_{80}(OH)_{42}$ compared to those residing closer to C_{80}. Second, $C_{80}(OH)_{42}$ was able to form hydrogen bonding with POPC which might

have increased the stability of the molecule within the bilayer. The conclusion of these analyses is that POPC, DSPE, CHOL, $C_{80}(OH)_{42}$ assembly is much more stable in physiological solutions compared to POPC, DSPE, CHOL, C_{80} assembly. Furthermore, $C_{80}/C_{80}(OH)_{42}$ never induced structural instability in these LBL formulations. These results also imply that $Gd_3N@C_{80}(OH)_{42}$ containing liposomes to be stable in physiological environment compared to $Gd_3N@C_{80}$ containing liposomes.

CHAPTER V

DISSERTATION SUMMARY

The thesis had three specific objectives. First, studying the state of the art of theranostic liposomes and identify potential targets for theranostic delivery. Second, to develop novel glioblastoma theranostic liposome with higher imaging and cancer cells killing capability. Third, study the structural stability of these experimentally developed theranostics in physiological salt solutions and at body temperature by using molecular dynamics simulations.

In the first chapter the state of the art of theranostics liposomes are discussed, categorically, in detail with more emphasis on formulation mechanisms, challenges and possible improvement directions for their usage in glioma treatments. This updated review is different from the previous reviews in that it focuses only on liposomes and hence have a better coverage on theranostic liposomes. Targets that are often used for drug delivery are presented but also new potential glioma biomarkers mined from different databases and the literature are discussed with more emphasis on their role in gliomas migration, proliferation, activation etc. The novelty of the targets identification process is that patient databases such as TCGA, the protein atlas and REMBERANDT are accessed and the application of the identified targets are reviewed in the literature.

These new biomarkers can be targeted to improve the delivery of imaging agents and cytotoxic or cytostatic drugs through ligand-receptor mediated endocytosis, antibody (fragment) based delivery, peptide based delivery, or other mechanisms such as a recombinant immunotherapy modality.

In the second chapter the design and testing of a dual-targeted theranostic is discussed in detail. For the first time $Gd_3N@C_{80}(OH)$ and DXR encapsulated theranostic liposome conjugated with transferrin (Tf) and lactoferrin (Lf) is developed and tested. The novelty of this formulation is that besides to having the novel higher contrast agent $Gd_3N@C_{80}(OH)$, it has a potential to cross the BBB through lactoferrin receptors, transferrin receptors or both depending on the expression level of the receptors and targets transferrin or lactoferrin receptors expressing cancer cells. To this end, the hydrodynamic size, zeta potential, encapsulation efficiency and the assembly of $Gd_3N@C_{80}(OH)$ and DXR loaded liposomes are characterized. The functionalization, tagging and PEGylating of the liposomes are also verified using Fourier-transform infrared spectroscopy (FTIR) and ultraviolet-visible spectrophotometry (UV-VIS) analysis. Cell viability test on U251-MG cells indicated successful delivery of DXR via Tf and dual (Tf & Lf) tagged theranostics. Importantly, the dual targeted liposomes were able to significantly induce cell death compared to cells death recorded for lactoferrin, a less expressed receptor on U251-MG cell, targeted liposomes. Furthermore, drug-free liposomes treated cells never shown a significant viability difference from untreated cells indicating the biocompatibility of the lipid components of the liposomes.

In the third chapter the dynamics and structural stability of Gd-fullerene ($Gd_3N@C_{80}$) inside of lipid bilayers immersed in physiological salt solutions and the interactions of those molecules with the lipid bilayer constituents are discussed in detail. The novelty is that for the first time the structural stability of C_{80}/$C_{80}(OH)_{42}$ containing POPC: DSPE: Cholesterol lipid bilayers that are immersed in 0.15 M KCl, NaCl and $CaCl_2$ are evaluated using, NAMD, molecular dynamic simulations. The stability study is realized by computing root means square deviations, area per lipid, radial distribution functions of ions, number density profiles, order parameters, lipid bilayer thickness and lipid interdigitations and these results are discussed in terms of the effect of the molecules on the lipid bilayer structures or vice versa. Furthermore, the dynamics of the fullerene cages, i.e. C_{80}/$C_{80}(OH)_{42}$, across different regions of the lipid bilayers are studied using steered molecular dynamics simulations. The results indicate that C_{80}/$C_{80}(OH)_{42}$ remains structurally stable throughout the simulation windows. The energy required to displace $C_{80}(OH)_{42}$ across the lipid bilayer is found to be higher than the energy required to displace C_{80}, partly, due to hydrogen bonding of the former with the head groups of POPC. Further, a lower SCD of the lipids closer to C_{80} compared to the lipids residing closer to $C_{80}(OH)_{42}$ might have contributed for the less stability of C_{80} containing LBLs compared to those loaded with $C_{80}(OH)_{42}$. These results, along with experimental and computational studies which proven the stability of Gd_3N inside C_{80} support the hypothesis that OH-functionalized fullerene cages and thereby OH functionalized Gd-fullerene containing liposomes to be stable in physiological salt solutions and are in accordance with the experimental observations reported in the second chapter.

REFERENCES

1. Ostrom, Q.T., et al., *CBTRUS statistical report: primary brain and central nervous system tumors diagnosed in the United States in 2007-2011.* Neuro Oncol, 2014. **16 Suppl 4**: p. iv1-63.

2. Ostrom, Q.T., et al., *CBTRUS Statistical Report: Primary Brain and Other Central Nervous System Tumors Diagnosed in the United States in 2009–2013.* Neuro-Oncology, 2016. **18**(suppl_5): p. v1-v75.

3. Ellingson, B.M., et al., *Consensus recommendations for a standardized Brain Tumor Imaging Protocol in clinical trials.* Neuro Oncol, 2015. **17**(9): p. 1188-98.

4. Weller, M., et al., *EANO guideline for the diagnosis and treatment of anaplastic gliomas and glioblastoma.* Lancet Oncol, 2014. **15**(9): p. e395-403.

5. Caravan, P., *Strategies for increasing the sensitivity of gadolinium based MRI contrast agents.* Chem Soc Rev, 2006. **35**(6): p. 512-23.

6. Hesselink, J.R. and G.A. Press, *MR contrast enhancement of intracranial lesions with Gd-DTPA.* Radiol Clin North Am, 1988. **26**(4): p. 873-87.

7. Hesselink, J.R., et al., *Benefits of Gd-DTPA for MR imaging of intracranial abnormalities.* J Comput Assist Tomogr, 1988. **12**(2): p. 266-74.

8. Maeda, H., *The enhanced permeability and retention (EPR) effect in tumor vasculature: the key role of tumor-selective macromolecular drug targeting.* Adv Enzyme Regul, 2001. **41**: p. 189-207.

9. McWilliams, J.P., et al., *Image-guided tumor ablation: emerging technologies and future directions.* Semin Intervent Radiol, 2010. **27**(3): p. 302-13.

10. Ahmed, M., *Image-guided tumor ablation: standardization of terminology and reporting criteria--a 10-year update: supplement to the consensus document.* J Vasc Interv Radiol, 2014. **25**(11): p. 1706-8.

11. Spinczyk, D., *Towards the clinical integration of an image-guided navigation system for percutaneous liver tumor ablation using freehand 2D ultrasound images.* Comput Aided Surg, 2015: p. 1-12.

12. Kim, S.S., et al., *Effective treatment of glioblastoma requires crossing the blood-brain barrier and targeting tumors including cancer stem cells: The promise of nanomedicine.* Biochem Biophys Res Commun, 2015.

13. Peer, D., et al., *Nanocarriers as an emerging platform for cancer therapy.* Nat Nanotechnol, 2007. **2**(12): p. 751-60.

14. Woodworth, G.F., et al., *Emerging insights into barriers to effective brain tumor therapeutics.* Front Oncol, 2014. **4**: p. 126.

15. Kumari, S., et al., *Overcoming blood brain barrier with a dual purpose Temozolomide loaded Lactoferrin nanoparticles for combating glioma (SERP-17-12433).* Scientific Reports, 2017. **7**(1): p. 6602.

16. Mu, L.-M., et al., *Lipid vesicles containing transferrin receptor binding peptide TfR-T12 and octa-arginine conjugate stearyl-R8 efficiently treat brain glioma along with glioma stem cells.* Scientific Reports, 2017. **7**(1): p. 3487.

17. Vosshenrich, R. and P. Reimer, *Nephrogenic systemic fibrosis.* Vasa., 2009. **38**(1): p. 31-38.

18. Adiseshaiah, P., et al., *A Novel Gadolinium-Based Trimetasphere Metallofullerene for Application as a Magnetic Resonance Imaging Contrast Agent.* Invest Radiol, 2013.

19. Dellinger, A., et al., *Functionalization of gadolinium metallofullerenes for detecting atherosclerotic plaque lesions by cardiovascular magnetic resonance.* J Cardiovasc Magn Reson, 2013. **15**(1): p. 7.

20. Weaver, M. and D.W. Laske, *Transferrin receptor ligand-targeted toxin conjugate (Tf-CRM107) for therapy of malignant gliomas.* J Neurooncol., 2003. **65**(1): p. 3-13.

21. Voth, B., et al., *Transferrin receptors and glioblastoma multiforme: Current findings and potential for treatment.* Journal of Clinical Neuroscience, 2015. **22**(7): p. 1071-1076.

22. Dai, Z., *Advances in Nanotheranostics I,* in *Design and Fabrication of Theranosic Nanoparticles,* ZhifeiDai, Editor 2016, Springer: Heidelberg

23. Sung Duk Jo, et al., *Targeted Nanotheranostics for Future Personalized Medicine: Recent Progress in Cancer Therapy.* Theranostics 2016. **6**(9): p. 1362-1376.

24. Moumita Roy Chowdhury, et al., *Cancer nanotheranostics: Strategies, promises and impediments.* Biomedicine & Pharmacotherapy 2016. **84** p. 291-304.

25. Musafar Gani Sikkandhar, et al., *Theranostic Probes for Targeting Tumor Microenvironment: An Overview.* International Journal o f Molecular Sciences, 2017. **18**.

26. Lisa Sercombe, et al., *Advances and Challenges of Liposome Assisted Drug Delivery.* Frontiers in Pharmacology, 2015. **6**(286).

27. Daniel Bobo, et al., *Nanoparticle-Based Medicines: A Review of FDA-Approved Materials and Clinical Trials to Date.* Pharm Res 2016. **33**: p. 2373-2387.

28. Bulbake, U., et al., *Liposomal Formulations in Clinical Use: An Updated Review.* Pharmaceutics, 2017. **9**(2): p. 12.

29. Porcu, E.P., et al., *Indocyanine green delivery systems for tumour detection and treatments.* Biotechnol Adv, 2016. **34**(5): p. 768-89.

30. Bangham, A.D. and R.W. Horne, *Negative staining of phospholipids and their structural modification by surface-active agents as observed in the electron microscope.* Journal of Molecular Biology, 1964. **8**(5): p. 660-IN10.

31. Xing, H., K. Hwang, and Y. Lu, *Recent Developments of Liposomes as Nanocarriers for Theranostic Applications.* Theranostics, 2016. **6**(9): p. 1336-1352.

32. Allen, T.M. and P.R. Cullis, *Liposomal drug delivery systems: from concept to clinical applications.* Adv Drug Deliv Rev, 2013. **65**(1): p. 36-48.

33. Gabizon, A. and D. Papahadjopoulos, *Liposome formulations with prolonged circulation time in blood and enhanced uptake by tumors.* Proceedings of the National Academy of Sciences of the United States of America, 1988. **85**(18): p. 6949-6953.

34. Dou, Y., K. Hynynen, and C. Allen, *To heat or not to heat: Challenges with clinical translation of thermosensitive liposomes.* Journal of Controlled Release, 2017. **249**: p. 63-73.

35. Massiot, J., et al., *Impact of lipid composition and photosensitizer hydrophobicity on the efficiency of light-triggered liposomal release.* Physical chemistry chemical physics : PCCP, 2017. **19**(18): p. 11460-11473.

36. Ferreira, R.V., et al., *Thermosensitive gemcitabine-magnetoliposomes for combined hyperthermia and chemotherapy.* Nanotechnology, 2016. **27**(8): p. 085105.

37. Gao, C., et al., *pH-Responsive prodrug nanoparticles based on a sodium alginate derivative for selective co-release of doxorubicin and curcumin into tumor cells.* Nanoscale, 2017. **9**(34): p. 12533-12542.

38. Elgqvist, J., *Nanoparticles as Theranostic Vehicles in Experimental and Clinical Applications—Focus on Prostate and Breast Cancer.* International Journal of Molecular Sciences, 2017. **18**(5): p. 1102.

39. Bowen, T., W.T. Al-Jamal, and K. Kostarelos, *The engineering of doxorubicin-loaded liposome-quantum dot hybrids for cancer theranostics.* Chinese Physics B, 2014. **23**(8): p. 087805.

40. Aaron Tan, et al., *Quantum dots and carbon nanotubes in oncology: a review on emerging theranostic applications in nanomedicine.* Nanomedicine 2011. **6**(6): p. 1101-1114.

41. Wen, C.J., et al., *Nanocomposite liposomes containing quantum dots and anticancer drugs for bioimaging and therapeutic delivery: a comparison of cationic, PEGylated and deformable liposomes.* Nanotechnology, 2013. **24**(32): p. 325101.

42. Muthu, M.S., et al., *Theranostic liposomes of TPGS coating for targeted co-delivery of docetaxel and quantum dots.* Biomaterials, 2012. **33**(12): p. 3494-501.

43. Kim, M.W., et al., *Cancer-targeted Nucleic Acid Delivery and Quantum Dot Imaging Using EGF Receptor Aptamer-conjugated Lipid Nanoparticles.* Scientific Reports, 2017. **7**(1): p. 9474.

44. Seleci, M., et al., *Theranostic Liposome–Nanoparticle Hybrids for Drug Delivery and Bioimaging.* International Journal of Molecular Sciences, 2017. **18**(7): p. 1415.

45. Wen, C.-J., et al., *Theranostic liposomes loaded with quantum dots and apomorphine for brain targeting and bioimaging.* International Journal of Nanomedicine, 2012. **7**: p. 1599-1611.

46. Tedeschi, E., et al., *Gadolinium retention in the body: what we know and what we can do.* La radiologia medica, 2017. **122**(8): p. 589-600.

47. Zhou, Z. and Z.-R. Lu, *Gadolinium-Based Contrast Agents for MR Cancer Imaging.* Wiley interdisciplinary reviews. Nanomedicine and nanobiotechnology, 2013. **5**(1): p. 1-18.

48. Fraum, T.J., et al., *Gadolinium-based contrast agents: A comprehensive risk assessment.* Journal of Magnetic Resonance Imaging, 2017. **46**(2): p. 338-353.

49. Ren, L., et al., *MRI-visible liposome nanovehicles for potential tumor-targeted delivery of multimodal therapies.* Nanoscale Nanoscale, 2015. **7**(30): p. 12843-12850.

50. Grange, C., et al., *Combined delivery and magnetic resonance imaging of neural cell adhesion molecule-targeted doxorubicin-containing liposomes in experimentally induced Kaposi's sarcoma.* Cancer Res, 2010. **70**(6): p. 2180-90.

51. Jin, Y., et al., *Nanosystem composed with MSNs, gadolinium, liposome and cytotoxic peptides for tumor theranostics.* Colloids Surf B Biointerfaces, 2017. **151**: p. 240-248.

52. Li, S., et al., *A Novel Multifunctional Theranostic Liposome Drug Delivery System: Construction, Characterization, and Multimodality MR, Near-infrared Fluorescent and Nuclear Imaging.* Bioconjugate chemistry, 2012. **23**(6): p. 1322-1332.

53. Dellinger, A., et al., *Application of fullerenes in nanomedicine: an update.* Nanomedicine (Lond), 2013. **8**(7): p. 1191-208.

54. Tagami, T., et al., *MRI monitoring of intratumoral drug delivery and prediction of the therapeutic effect with a multifunctional thermosensitive liposome.* Biomaterials, 2011. **32**(27): p. 6570-8.

55. Kono, K., et al., *Multi-functional liposomes having temperature-triggered release and magnetic resonance imaging for tumor-specific chemotherapy.* Biomaterials, 2011. **32**(5): p. 1387-95.

56. Rizzitelli, S., et al., *The release of Doxorubicin from liposomes monitored by MRI and triggered by a combination of US stimuli led to a complete tumor regression in a breast cancer mouse model.* J Control Release, 2016. **230**: p. 57-63.

57. Rizzitelli, S., et al., *Sonosensitive theranostic liposomes for preclinical in vivo MRI-guided visualization of doxorubicin release stimulated by pulsed low intensity non-focused ultrasound.* J Control Release, 2015. **202**: p. 21-30.

58. Neuwelt, E.A., et al., *Ultrasmall superparamagnetic iron oxides (USPIOs): a future alternative magnetic resonance (MR) contrast agent for patients at risk for nephrogenic systemic fibrosis (NSF)?* Kidney international, 2009. **75**(5): p. 465-474.

59. Vasanawala, S.S., et al., *Safety and Technique of Ferumoxytol Administration for MRI.* Magnetic resonance in medicine, 2016. **75**(5): p. 2107-2111.

60. Nguyen, V.D., et al., *Nanohybrid magnetic liposome functionalized with hyaluronic acid for enhanced cellular uptake and near-infrared-triggered drug release.* Colloids Surf B Biointerfaces, 2017. **154**: p. 104-114.

61. He, Y., et al., *Design of multifunctional magnetic iron oxide nanoparticles/mitoxantrone-loaded liposomes for both magnetic resonance imaging and targeted cancer therapy.* International Journal of Nanomedicine, 2014. **9**: p. 4055-4066.

62. Erten, A., et al., *MR and fluorescence imaging of doxorubicin loaded nanoparticles using a novel in vivo model.* Nanomedicine : nanotechnology, biology, and medicine, 2010. **6**(6): p. 797-807.

63. van der Geest, T., et al., *Radionuclide imaging of liposomal drug delivery.* Expert Opinion on Drug Delivery, 2016. **13**(9): p. 1231-1242.

64. Medicine, N.R.C.U.a.I.o.M.U.C.o.S.o.t.S.o.N., *Advancing Nuclear Medicine Through Innovation.* . Targeted Radionuclide Therapy, 2007. **4**(National Academies Press (US)).

65. Soundararajan, A., et al., *(186)Re-Liposomal Doxorubicin (Doxil): In Vitro Stability, Pharmacokinetics, Imaging and Biodistribution in a Head and Neck Squamous Cell Carcinoma Xenograft Model.* Nuclear medicine and biology, 2009. **36**(5): p. 515-524.

66. Bao, A., et al., *Direct 99mTc labeling of pegylated liposomal doxorubicin (Doxil) for pharmacokinetic and non-invasive imaging studies.* J Pharmacol Exp Ther, 2004. **308**(2): p. 419-25.

67. Delphine Denoyer and N. Pouliot, *Radionuclide Theranostics in Cancer.* Molecular Imaging & Dynamics, 2013. **4**(1).

68. Zhang, N., et al., *Bubble-generating nano-lipid carriers for ultrasound/CT imaging-guided efficient tumor therapy.* International Journal of Pharmaceutics, 2017.

69. Al-Ahmady, Z., et al., *Engineering thermosensitive liposome-nanoparticle hybrids loaded with doxorubicin for heat-triggered drug release.* International Journal of Pharmaceutics, 2016. **514**(1): p. 133-141.

70. Viglianti, B.L., et al., *In vivo monitoring of tissue pharmacokinetics of liposome/drug using MRI: Illustration of targeted delivery.* Magnetic Resonance in Medicine, 2004. **51**(6): p. 1153-1162.

71. Fahy, E., et al., *Update of the LIPID MAPS comprehensive classification system for lipids.* Journal of Lipid Research, 2009. **50**(Suppl): p. S9-S14.

72. Lozano, N., et al., *Monoclonal antibody-targeted PEGylated liposome-ICG encapsulating doxorubicin as a potential theranostic agent.* Int J Pharm, 2015. **482**(1-2): p. 2-10.

73. Gao, H., *Progress and perspectives on targeting nanoparticles for brain drug delivery.* Acta Pharmaceutica Sinica B, 2016. **6**(4): p. 268-286.

74. Mäger, I., et al., *Targeting blood-brain-barrier transcytosis – perspectives for drug delivery.* Neuropharmacology, 2017. **120**: p. 4-7.

75. Li, Y.M. and W.A. Hall, *Cell surface receptors in malignant glioma.* Neurosurgery, 2011. **69**(4): p. 980-94; discussion 994.

76. Bindera, D.C., A.A. Davis, and D.A. Wainwright, *Immunotherapy for cancer in the central nervous system: Current and future directions.* Oncoimmunology, 2016. **5**(2).

77. Mallawaaratchy, D.M., et al., *Membrane Proteome Analysis of Glioblastoma Cell Invasion.* J Neuropathol Exp Neurol, 2015. **74**(5): p. 425-441.

78. Meng, J., V. Agrahari, and I. Youm, *Advances in Targeted Drug Delivery Approaches for the Central Nervous System Tumors: The Inspiration of Nanobiotechnology.* J Neuroimmune Pharmacol, 2017. **12**(1): p. 84-98.

79. J., R., *Maximizing Local Access to Therapeutic Deliveries in Glioblastoma. Part V: Clinically Relevant Model for Testing New Therapeutic Approaches.* , S.D. Vleeschouwe, Editor. 2017, Codon Publications Brisbane (AU).

80. Day, B.W., B.W. Stringer, and A.W. Boyd, *Eph receptors as therapeutic targets in glioblastoma.* British Journal of Cancer, 2014. **111**(7): p. 1255-1261.

81. Gilder, A.S., et al., *The Urokinase Receptor Induces a Mesenchymal Gene Expression Signature in Glioblastoma Cells and Promotes Tumor Cell Survival in Neurospheres.* Scientific reports, 2018. **8**(1).

82. Gilder, A.S., et al., *The Urokinase Receptor Induces a Mesenchymal Gene Expression Signature in Glioblastoma Cells and Promotes Tumor Cell Survival in Neurospheres.* Scientific Reports, 2018. **8**: p. 2982.

83. Wadajkar, A.S., et al., *Tumor-targeted nanotherapeutics: overcoming treatment barriers for glioblastoma.* Wiley Interdisciplinary Reviews: Nanomedicine and Nanobiotechnology, 2017. **9**(4): p. e1439-n/a.

84. Nandeesh, B.N., et al., *Recurrent Glioblastomas Exhibit Higher Expression of Biomarkers with Stem-like Properties.* Journal of neurosciences in rural practice, 2018. **9**(1).

85. Pearson, J.R.D. and T. Regad, *Targeting cellular pathways in glioblastoma multiforme.* Signal Transduction and Targeted Therapy, 2017. **2**: p. 17040.

86. Zhu, H., et al., *Overexpression of centrosomal protein 55 regulates the proliferation of glioma cell and mediates proliferation promoted by EGFRvIII in glioblastoma U251 cells.* Oncology Letters, 2018. **15**(2): p. 2700.

87. Eskilsson, E., et al., *EGFRvIII mutations can emerge as late and heterogenous events in glioblastoma development and promote angiogenesis through Src activation.* Neuro-Oncology, 2016. **18**(12): p. 1644-1655.

88. Takeshi Shimamura, Syed R. Husain, and Raj K. Puri, *The IL-4 and IL-13 pseudomonas exotoxins: new hope for brain tumor therapy.* Neurosurgical Focus, 2006. **20**(4): p. E11.

89. Sonawane, P., et al., *Novel Molecular Multilevel Targeted Antitumor Agents.* Cancer translational medicine, 2017. **3**(3): p. 69-79.

90. Hersh, D.S., et al., *Differential expression of the TWEAK receptor Fn14 in IDH1 wild-type and mutant gliomas.* Journal of Neuro-Oncology, 2018.

91. Perez, J.G., et al., *The TWEAK Receptor Fn14 is a Potential Cell Surface Portal for Targeted Delivery of Glioblastoma Therapeutics.* Oncogene, 2016. **35**(17): p. 2145-2155.

92. Jaal, J., et al., *VEGFR-2 Expression in Glioblastoma Multiforme Depends on Inflammatory Tumor Microenvironment.* International Journal of Inflammation, 2015. **2015**: p. 385030.

93. Schneider, J.R., K. Kwan, and J.A. Boockvar, *Use of HER2-Specific Chimeric Antigen Receptor-Modified Virus-Specific T Cells as a Potential Therapeutic for Progressive HER2-Positive Glioblastoma.* Neurosurgery, 2017. **81**(5): p. N42-N43.

94. Kalamatianos, T., et al., *naplastic Lymphoma Kinase in Glioblastoma: Detection/Diagnostic Methods and Therapeutic Options.* PRA Recent Patents on Anti-Cancer Drug Discovery, 2018. **13**.

95. Narushima, Y., et al., *Integrative Network Analysis Combined with Quantitative Phosphoproteomics Reveals Transforming Growth Factor-beta Receptor type-2 (TGFBR2) as a Novel Regulator of Glioblastoma Stem Cell Properties.* Molecular & Cellular Proteomics : MCP, 2016. **15**(3): p. 1017-1031.

96. Séhédic, D., et al., *Locoregional Confinement and Major Clinical Benefit of (188)Re-Loaded CXCR4-Targeted Nanocarriers in an Orthotopic Human to Mouse Model of Glioblastoma.* Theranostics, 2017. **7**(18): p. 4517-4536.

97. Cruickshanks, N., et al., *Role and Therapeutic Targeting of the HGF/MET Pathway in Glioblastoma.* Cancers, 2017. **9**(7): p. 87.

98. Wallace, G.C., et al., *Targeting Oncogenic ALK and MET: A Promising Therapeutic Strategy for Glioblastoma.* Metabolic brain disease, 2013. **28**(3): p. 355-366

.

99. Knubel, K.H., et al., *MerTK inhibition is a novel therapeutic approach for glioblastoma multiforme.* Oncotarget, 2014. **5**(5): p. 1338-1351.

100. Uhlen, M., et al., *A pathology atlas of the human cancer transcriptome.* Science, 2017. **357**(6352).

101. Bausch-Fluck, D., et al., *A mass spectrometric-derived cell surface protein atlas.* PLoS One, 2015. **10**(3): p. e0121314.

102. Doucette, T., et al., *Immune heterogeneity of glioblastoma subtypes: extrapolation from the cancer genome atlas.* Cancer Immunol Res, 2013. **1**(2): p. 112-22.

103. Xenarios, I., et al., *DIP, the Database of Interacting Proteins: a research tool for studying cellular networks of protein interactions.* Nucleic Acids Research, 2002. **30**(1): p. 303-305.

104. Mathias Uhlén, et al., *Tissue-based map of the human proteome.* Science, Proteomics, 2015. **347** (622).

105. Clark, K., et al., *The Cancer Imaging Archive (TCIA): Maintaining and Operating a Public Information Repository.* Journal of Digital Imaging, 2013. **26**(6): p. 1045-1057.

106. *Project Betastasis* 2018 [cited 4/25/2018; Available from: http://www.betastasis.com/glioma/rembrandt/.

107. Fujikawa, A., et al., *Targeting PTPRZ inhibits stem cell-like properties and tumorigenicity in glioblastoma cells.* Scientific Reports, 2017. **7**: p. 5609.

108. Behjati, S., et al., *Recurrent PTPRB and PLCG1 mutations in angiosarcoma.* Nature genetics, 2014. **46**(4): p. 376-379.

109. Qi, Y., Y. Dai, and S. Gui, *Protein tyrosine phosphatase PTPRB regulates Src phosphorylation and tumour progression in NSCLC.* Clinical and Experimental Pharmacology and Physiology, 2016. **43**(10): p. 1004-1012.

110. Ulbricht, U., et al., *RNA interference targeting protein tyrosine phosphatase zeta/receptor-type protein tyrosine phosphatase beta suppresses glioblastoma growth in vitro and in vivo.* J Neurochem, 2006. **98**(5): p. 1497-506.

111. Alessio Amatu, A.S.-B., Salvatore Siena, *NTRK gene fusions as novel targets of cancer therapy across multiple tumour types.* ESMO Open, 2016. **1**(e000023).

112. Palani, M., R. Arunkumar, and A.J. Vanisree, *Methylation and Expression Patterns of Tropomyosin-Related Kinase Genes in Different Grades of Glioma.* NeuroMolecular Medicine, 2014. **16**(3): p. 529-539.

113. Liang, Y., A.W. Bollen, and N. Gupta, *CC chemokine receptor-2A is frequently overexpressed in glioblastoma.* Journal of Neuro-Oncology, 2008. **86**(2): p. 153-163.

114. Vakilian, A., et al., *CCL2/CCR2 signaling pathway in glioblastoma multiforme.* Neurochem Int, 2017. **103**: p. 1-7.

115. Jahani-Asl, A., et al., *Control of glioblastoma tumorigenesis by feed-forward cytokine signaling.* Nature neuroscience, 2016. **19**(6): p. 798-806.

116. Natesh, K., et al., *Oncostatin-M Differentially Regulates Mesenchymal and Proneural Signature Genes in Gliomas via STAT3 Signaling.* Neoplasia (New York, N.Y.), 2015. **17**(2): p. 225-237.

117. Zadeh, G. and K. Aldape, *ACVR1 mutations and the genomic landscape of pediatric diffuse glioma.* Nat Genet, 2014. **46**(5): p. 421-2.

118. Zhu, S., et al., *Recombinant Immunotoxin Therapy of Glioblastoma: Smart Design, Key Findings, and Specific Challenges.* BioMed Research International, 2017. **2017**: p. 7929286.

119. Kanabur, P., et al., *Patient-derived glioblastoma stem cells respond differentially to targeted therapies.* Oncotarget, 2016. **7**(52): p. 86406-86419.

120. Hong, J.-D., et al., *Silencing platelet-derived growth factor receptor-β enhances the radiosensitivity of C6 glioma cells in vitro and in vivo.* Oncology Letters, 2017. **14**(1): p. 329-336.

121. Berghoff, J., et al., *Gamma-secretase-independent role for cadherin-11 in neurotrophin receptor p75 (p75(NTR)) mediated glioblastoma cell migration.* Mol Cell Neurosci, 2015. **69**: p. 41-53.

122. He, X., et al., *MicroRNA-181c inhibits glioblastoma cell invasion, migration and mesenchymal transition by targeting TGF-β pathway.* Biochemical and Biophysical Research Communications, 2016. **469**(4): p. 1041-1048.

123. Tu, Z., et al., *CCR9 in cancer: oncogenic role and therapeutic targeting.* Journal of Hematology & Oncology, 2016. **9**: p. 10.

124. Yoldi, G., et al., *RANK Signaling Blockade Reduces Breast Cancer Recurrence by Inducing Tumor Cell Differentiation.* Cancer Res, 2016. **76**(19): p. 5857-5869.

125. Guo, M., et al., *miR-656 inhibits glioma tumorigenesis through repression of BMPR1A.* Carcinogenesis, 2014. **35**(8): p. 1698-1706.

126. Pyonteck, S.M., et al., *CSF-1R inhibition alters macrophage polarization and blocks glioma progression.* Nat Med, 2013. **19**(10): p. 1264-72.

127. Kunwar, S., et al., *Phase III randomized trial of CED of IL13-PE38QQR vs Gliadel wafers for recurrent glioblastoma().* Neuro-Oncology, 2010. **12**(8): p. 871-881.

128. Kunwar, S., et al., *Direct intracerebral delivery of cintredekin besudotox (IL13-PE38QQR) in recurrent malignant glioma: a report by the Cintredekin Besudotox Intraparenchymal Study Group.* J Clin Oncol, 2007. **25**(7): p. 837-44.

129. Sengupta, S., et al., *Interleukin-13 receptor alpha 2-targeted glioblastoma immunotherapy.* Biomed Res Int, 2014. **2014**: p. 952128.

130. Uhlen, M., et al., *Proteomics. Tissue-based map of the human proteome.* Science, 2015. **347**(6220): p. 1260419.

131. Stelzer, G., Naomi Rosen, Inbar Plaschkes, Shahar Zimmerman, Michal Twik, Simon Fishilevich, Tsippi Iny Stein, Ron Nudel, Iris Lieder, Yaron Mazor, Sergey Kaplan, Dvir Dahary, David Warshawsky, Yaron Guan-Golan, Asher Kohn, Noa Rappaport, Marilyn Safran and Doron Lancet *The GeneCards Suite: From Gene Data Mining to Disease Genome Sequence Analyses.* Current protocols in bioinformatics, 2016. **54** p. 1.30.1-1.30.33.

132. Oswald, C., et al., *Intracellular allosteric antagonism of the CCR9 receptor.* Nature, 2016. **540**(7633): p. 462-465.

133. Gupta, P., et al., *CCR9/CCL25 expression in non-small cell lung cancer correlates with aggressive disease and mediates key steps of metastasis.* Oncotarget, 2014. **5**(20): p. 10170-10179.

134. von dem Knesebeck, A., et al., *RANK (TNFRSF11A) Is Epigenetically Inactivated and Induces Apoptosis in Gliomas.* Neoplasia, 2012. **14**(6): p. 526-34.

135. De, I., et al., *CSF1 overexpression promotes high-grade glioma formation without impacting the polarization status of glioma-associated microglia and macrophages.* Cancer Res, 2016. **76**(9): p. 2552-60.

136. Quail, D.F., et al., *The tumor microenvironment underlies acquired resistance to CSF1R inhibition in gliomas.* Science, 2016. **352**(6288): p. aad3018.

137. Fujita, M., et al., *Role of type-1 interferons in anti-glioma immunosurveillance - Using mouse studies to guide examination of novel prognostic markers in humans.* Clin Cancer Res, 2010. **16**(13): p. 3409-19.

138. Lim, S.Y., et al., *Targeting the CCL2-CCR2 signaling axis in cancer metastasis.* Oncotarget, 2016. **7**(19): p. 28697-710.

139. Ma, Y., et al., *InsR/IGF1R pathway mediates resistance to EGFR inhibitors in glioblastoma.* Clin Cancer Res, 2016. **22**(7): p. 1767-76.

140. Mohan, S., A. Bonni, and A. Jahani-Asl, *Targeting OSMR in glioma stem cells.* Oncotarget, 2017. **8**(10): p. 16103-16104.

141. Buczkowicz, P., et al., *Genomic analysis of diffuse intrinsic pontine gliomas identifies three molecular subgroups and recurrent activating ACVR1 mutations.* Nat Genet, 2014. **46**(5): p. 451-6.

142. Hoffman, L.M., et al., *Spatial genomic heterogeneity in diffuse intrinsic pontine and midline high-grade glioma: implications for diagnostic biopsy and targeted therapeutics.* Acta Neuropathol Commun, 2016. **4**.

143. Kwiatkowski, S.C., et al., *Neuropilin-1 modulates TGFβ signaling to drive glioblastoma growth and recurrence after anti-angiogenic therapy.* PLoS ONE, 2017. **12**(9): p. e0185065.

144. Lee, J., et al., *Epigenetic-Mediated Dysfunction of the Bone Morphogenetic Protein Developmental Pathway Inhibits Differentiation of Human Glioblastoma Tumor Initiating Cells.* Cancer cell, 2008. **13**(1): p. 69-80.

145. Shi, Y., et al., *Tumour-associated macrophages secrete pleiotrophin to promote PTPRZ1 signalling in glioblastoma stem cells for tumour growth.* Nature Communications, 2017. **8**: p. 15080.

146. Fujikawa, A., et al., *Small-molecule inhibition of PTPRZ reduces tumor growth in a rat model of glioblastoma.* Sci Rep, 2016. **6**.

147. Auffinger, B., et al., *New therapeutic approaches for malignant glioma: in search of the Rosetta stone.* F1000 Medicine Reports, 2012. **4**: p. 18.

148. Ellingson, B.M., et al., *Consensus recommendations for a standardized Brain Tumor Imaging Protocol in clinical trials.* Neuro-Oncology, 2015. **17**(9): p. 1188-1198.

149. Wilson, T.A., M.A. Karajannis, and D.H. Harter, *Glioblastoma multiforme: State of the art and future therapeutics.* Surgical Neurology International, 2014. **5**: p. 64.

150. Schonberg, D.L., et al., *Preferential Iron Trafficking Characterizes Glioblastoma Stem-like Cells.* Cancer cell, 2015. **28**(4): p. 441-455.

151. Mu, L.-M., et al., *Lipid vesicles containing transferrin receptor binding peptide TfR-T(12) and octa-arginine conjugate stearyl-R(8) efficiently treat brain glioma along with glioma stem cells.* Scientific Reports, 2017. **7**: p. 3487.

152. Lalani, J., et al., *Protein functionalized tramadol-loaded PLGA nanoparticles: preparation, optimization, stability and pharmacodynamic studies.* Drug Dev Ind Pharm, 2013. **39**(6): p. 854-64.

153. Kumari, S., et al., *Overcoming blood brain barrier with a dual purpose Temozolomide loaded Lactoferrin nanoparticles for combating glioma (SERP-17-12433).* Scientific Reports, 2017. **7**: p. 6602.

154. Xie, H., et al., *Lactoferrin-conjugated superparamagnetic iron oxide nanoparticles as a specific MRI contrast agent for detection of brain glioma in vivo.* Biomaterials, 2011. **32**(2): p. 495-502.

155. Voth, B., et al., *Transferrin receptors and glioblastoma multiforme: Current findings and potential for treatment.* J Clin Neurosci, 2015. **22**(7): p. 1071-6.

156. Lam, F.C., et al., *Enhanced efficacy of combined temozolomide and bromodomain inhibitor therapy for gliomas using targeted nanoparticles.* Nature Communications, 2018. **9**(1): p. 1991.

157. Sun, T., et al., *Targeting transferrin receptor delivery of temozolomide for a potential glioma stem cell-mediated therapy.* Oncotarget, 2017. **8**(43): p. 74451-74465.

158. Gao, H., *Perspectives on Dual Targeting Delivery Systems for Brain Tumors.* Journal of Neuroimmune Pharmacology, 2017. **12**(1): p. 6-16.

159. Gao, H.-l., et al., *Effect of lactoferrin- and transferrin-conjugated polymersomes in brain targeting: in vitro and in vivo evaluations.* Acta Pharmacologica Sinica, 2010. **31**(2): p. 237-43.

160. Ji, B., et al., *Pharmacokinetics and brain uptake of lactoferrin in rats.* Life Sciences, 2006. **78**(8): p. 851-855.

161. Zhang, J., et al., *Gd3N@C84(OH)x: A New Egg-Shaped Metallofullerene Magnetic Resonance Imaging Contrast Agent.* Journal of the American Chemical Society, 2014. **136**(6): p. 2630-2636.

162. Nafradi, B., et al., *Molecular and spin dynamics in the paramagnetic endohedral fullerene Gd₃N@C₈₀*. Journal of Physical Chemistry Letters, 2012. **3**(22): p. 3291-3296.

163. Chen, L., et al., *Spin transition in Gd3N@C80, detected by low-temperature on-chip SQUID technique.* Journal of Applied Physics, 2011. **109**(7).

164. MacFarland, D.K., et al., *Hydrochalarones: A Novel Endohedral Metallofullerene Platform for Enhancing Magnetic Resonance Imaging Contrast.* Journal of Medicinal Chemistry, 2008. **51**(13): p. 3681-3683.

165. Mikawa, M., et al., *Paramagnetic Water-Soluble Metallofullerenes Having the Highest Relaxivity for MRI Contrast Agents.* Bioconjugate Chemistry, 2001. **12**(4): p. 510-514.

166. Gao, Z., et al., *Development of Gd3N@C80 encapsulated redox nanoparticles for high-performance magnetic resonance imaging.* Journal of Biomaterials Science, Polymer Edition, 2017. **28**(10-12): p. 1036-1050.

167. Han, Z., et al., *Targeted gadofullerene for sensitive magnetic resonance imaging and risk-stratification of breast cancer.* Nature Communications, 2017. **8**: p. 692.

168. Kepley, C.L., et al., *Negative regulation of FcεRI signaling by FcγRII costimulation in human blood basophils.* Journal of Allergy and Clinical Immunology, 2000. **106**(2): p. 337-348.

169. Tagen, M., et al., *The mitochondrial uncoupling protein 2 (UCP2) inhibits mast cell activation and reduces histamine content.* Journal of immunology (Baltimore, Md. : 1950), 2009. **183**(10): p. 6313-6319.

170. Ye, J., et al., *Primer-BLAST: A tool to design target-specific primers for polymerase chain reaction.* BMC Bioinformatics, 2012. **13**: p. 134-134.

171. Kepley, C.L., et al., *Syk deficiency in nonreleaser basophils.* Journal of Allergy and Clinical Immunology, 1999. **104**(2): p. 279-284.

172. Ying, X., et al., *Dual-targeting daunorubicin liposomes improve the therapeutic efficacy of brain glioma in animals.* J Control Release, 2010. **141**(2): p. 183-92.

173. Abraham, S.A., et al., *The Liposomal Formulation of Doxorubicin.* 2005. **391**: p. 71-97.

174. Zhou, Z., et al., *Liposomal formulation of amphiphilic fullerene antioxidants.* Bioconjug Chem, 2010. **21**(9): p. 1656-61.

175. Fritze, A., et al., *Remote loading of doxorubicin into liposomes driven by a transmembrane phosphate gradient.* Biochim Biophys Acta, 2006. **1758**(10): p. 1633-40.

176. Coates, J., *Interpretation of Infrared Spectra, A Practical Approach.* Encyclopedia of Analytical Chemistry, (R.A. Meyers (Ed.)): p. 10815–10837.

177. Ma, S.L., et al., *Lapatinib antagonizes multidrug resistance-associated protein 1-mediated multidrug resistance by inhibiting its transport function.* Mol Med, 2014. **20**: p. 390-9.

178. Torsvik, A., et al., *U-251 revisited: genetic drift and phenotypic consequences of long-term cultures of glioblastoma cells.* Cancer Med, 2014. **3**(4): p. 812-24.

179. Ding, H., et al., *Enhanced blood-brain barrier transmigration using a novel Transferrin-embedded fluorescent magnetoliposome nanoformulation.* Nanotechnology, 2014. **25**(5): p. 055101-055101.

180. Liu, F., et al., *Glycosylation improves the functional characteristics of chlorogenic acid–lactoferrin conjugate.* RSC Adv., 2015. **5**(95): p. 78215-78228.

181. Alyane, M., G. Barratt, and M. Lahouel, *Remote loading of doxorubicin into liposomes by transmembrane pH gradient to reduce toxicity toward H9c2 cells.* Saudi Pharm J, 2016. **24**(2): p. 165-75.

182. Ding, H., et al., *Enhanced blood-brain barrier transmigration using a novel transferrin embedded fluorescent magneto-liposome nanoformulation.* Nanotechnology, 2014. **25**(5): p. 055101.

183. Shameli, K., et al., *Synthesis and characterization of polyethylene glycol mediated silver nanoparticles by the green method.* Int J Mol Sci, 2012. **13**(6): p. 6639-50.

184. Chen, C. and C.P. Tripp, *An infrared spectroscopic based method to measure membrane permeance in liposomes.* Biochim Biophys Acta, 2008. **1778**(10): p. 2266-72.

185. Bozzuto, G. and A. Molinari, *Liposomes as nanomedical devices.* International Journal of Nanomedicine, 2015. **10**: p. 975-999.

186. Saraiva, C., et al., *Nanoparticle-mediated brain drug delivery: Overcoming blood–brain barrier to treat neurodegenerative diseases.* Journal of Controlled Release, 2016. **235**: p. 34-47.

187. Huwyler, J., D. Wu, and W.M. Pardridge, *Brain drug delivery of small molecules using immunoliposomes.* Proceedings of the National Academy of Sciences of the United States of America, 1996. **93**(24): p. 14164-14169.

188. Lockman, P.R., et al., *Nanoparticle Surface Charges Alter Blood–Brain Barrier Integrity and Permeability.* Journal of Drug Targeting, 2004. **12**(9-10): p. 635-641.

189. Decuzzi, P., et al., *Size and shape effects in the biodistribution of intravascularly injected particles.* Journal of Controlled Release, 2010. **141**(3): p. 320-327.

190. Wally, J. and S.K. Buchanan, *A structural comparison of human serum transferrin and human lactoferrin.* Biometals, 2007. **20**(3-4): p. 249-262.

191. Wang, S., et al., *Receptor-Mediated Drug Delivery Systems Targeting to Glioma.* Nanomaterials, 2016. **6**(1): p. 3.

192. Kanwar, J.R., R.M. Samarasinghe, and R. Sehgal, *Nano-Lactoferrin in Diagnostic, Imaging and Targeted Delivery for Cancer and Infectious Diseases.* Journal of Cancer Science & Therapy, 2012. **04**(03).

193. Thul, P.J., et al., *A subcellular map of the human proteome.* Science, 2017. **356**(6340).

194. Li, T., et al., *Trimetallic Nitride Endohedral Fullerenes Carboxyl-Gd3N@C80: A New Theranostic Agent for Combating Oxidative Stress and Resolving Inflammation.* ACS Applied Materials & Interfaces, 2017. **9**(21): p. 17681-17687.

195. Dellinger, A., et al., *Functionalization of gadolinium metallofullerenes for detecting atherosclerotic plaque lesions by cardiovascular magnetic resonance.* Journal of Cardiovascular Magnetic Resonance, 2013. **15**(7).

196. Robert, S.G.D.R., et al., *The interaction of C 60 and its derivatives with a lipid bilayer via molecular dynamics simulations.* Nanotechnology, 2009. **20**(11): p. 115102.

197. Bedrov, D., et al., *Passive Transport of C60 Fullerenes through a Lipid Membrane: A Molecular Dynamics Simulation Study.* The Journal of Physical Chemistry B, 2008. **112**(7): p. 2078-2084.

198. Tománek, D. *Guide through the Nanocarbon Jungle: Buckyballs, Nanotubes, Graphene, and Beyond*. 2018; Available from: https://web.pa.msu.edu/people/tomanek/GNJ/SI/fullerene-isomer/index.html.

199. Jie Guan, Z.J., Zhen Zhu, Chern Chuang, Bih-Yaw Jin,4 and David Tom´anek, *Local curvature and stability of two-dimensional systems.* Phys. Rev., 2014. **90**(B).

200. Inc., A.P.L. *Avanti Polar Lipids Inc.* 2018 [cited 2018 05-21]; Available from: https://avantilipids.com/product/850457/.

201. Vanommeslaeghe, K., et al., *CHARMM General Force Field (CGenFF): A force field for drug-like molecules compatible with the CHARMM all-atom additive biological force fields.* Journal of computational chemistry, 2010. **31**(4): p. 671-690.

202. Jo, S., et al., *CHARMM-GUI Membrane Builder for Mixed Bilayers and Its Application to Yeast Membranes.* Biophysical Journal, 2009. **97**(1): p. 50-58.

203. Phillips, J.C., et al., *Scalable Molecular Dynamics with NAMD.* Journal of computational chemistry, 2005. **26**(16): p. 1781-1802.

204. Dwiastuti, R., et al., *Molecular Dynamics Simulations and Empirical Observations on Soy Lecithin Liposome Preparation.* 2016, 2016. **16**(2): p. 7.

205. Gronbech-Jensen, N. and O. Farago, *Constant pressure and temperature discrete-time Langevin molecular dynamics.* J Chem Phys, 2014. **141**(19): p. 194108.

206. Humphrey, W., A. Dalke, and K. Schulten, *VMD: Visual molecular dynamics.* Journal of Molecular Graphics, 1996. **14**(1): p. 33-38.

207. Zhuang, X., et al., *An extensive simulation study of lipid bilayer properties with different head groups, acyl chain lengths, and chain saturations.* Biochimica et Biophysica Acta (BBA) - Biomembranes, 2016. **1858**(12): p. 3093-3104.

208. Guixà-González, R., et al., *MEMBPLUGIN: studying membrane complexity in VMD.* Bioinformatics, 2014. **30**(10): p. 1478-1480.

209. Giorgino, T., *Computing 1-D atomic densities in macromolecular simulations: The density profile tool for VMD.* Computer Physics Communications, 2014. **185**(1): p. 317-322.

210. Levine, B.G., J.E. Stone, and A. Kohlmeyer, *Fast Analysis of Molecular Dynamics Trajectories with Graphics Processing Units—Radial Distribution Function Histogramming.* Journal of computational physics, 2011. **230**(9): p. 3556-3569.

211. González, M.A., *Force fields and molecular dynamics simulations.* JDN, 2011. **12**: p. 169-200.

212. Carugo, O. and S. Pongor, *A normalized root-mean-spuare distance for comparing protein three-dimensional structures.* Protein Science : A Publication of the Protein Society, 2001. **10**(7): p. 1470-1473.

213. Frigini, E.N., J.J. López Cascales, and R.D. Porasso, *Molecular dynamics simulations of glyphosate in a DPPC lipid bilayer*. Chemistry and Physics of Lipids, 2018. **213**: p. 111-117.

214. Jurkiewicz, P., et al., *Structure, dynamics, and hydration of POPC/POPS bilayers suspended in NaCl, KCl, and CsCl solutions.* Biochimica et Biophysica Acta (BBA) - Biomembranes, 2012. **1818**(3): p. 609-616.

215. Ferreira, T.M., et al., *Cholesterol and POPC segmental order parameters in lipid membranes: solid state 1H-13C NMR and MD simulation studies.* Physical Chemistry Chemical Physics, 2013. **15**(6): p. 1976-1989.

216. Piggot, T.J., et al., *On the Calculation of Acyl Chain Order Parameters from Lipid Simulations.* Journal of Chemical Theory and Computation, 2017. **13**(11): p. 5683-5696.

217. Balleza, D., *Mechanical properties of lipid bilayers and regulation of mechanosensitive function: From biological to biomimetic channels.* Channels, 2012. **6**(4): p. 220-233.

218. Gallová, J., et al., *Bilayer thickness in unilamellar extruded 1,2-dimyristoleoyl and 1,2-dierucoyl phosphatidylcholine vesicles: SANS contrast variation study of cholesterol effect.* Colloids and Surfaces B: Biointerfaces, 2004. **38**(1): p. 11-14.

219. Li, L., et al., *A molecular dynamics simulation study of C60 fullerenes inside a dimyristoylphosphatidylcholine lipid bilayer*. The journal of physical chemistry. B, 2007. **111**(16): p. 4067-72.

APPENDIX A

SUPPLEMENTARY FIGURES

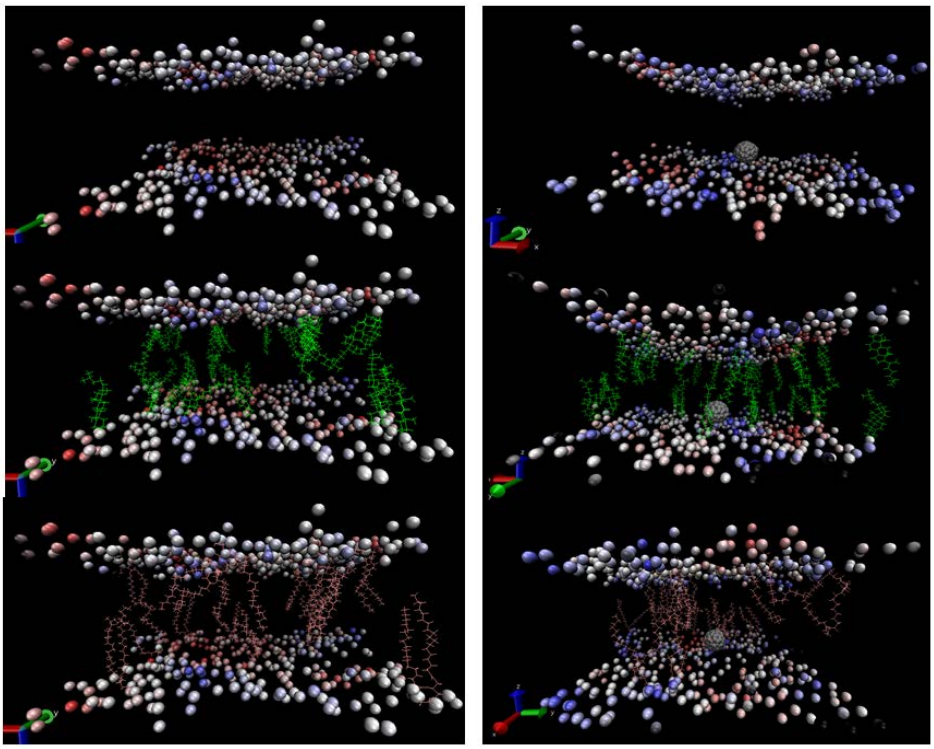

Supplementary Figure 31. Localization of C_{80} Inside Lipid Bilayer Immersed in KCl Solution after 10 ns Simulation Window (similar to Figure 24 but 10 ns earlier). A lipid bilayer free of C_{80} is shown on the left column and on the right C_{80} containing lipid bilayer. The figures from top to bottom represent, the localization of C_{80} off the center closer to lipid head group, localization of CHOL and the localization of DSPE inside the lipid bilayer respectively. The lipid bilayers are drawn on BWR color scale (35-45 Å thickness) to indicate if lateral bilayer thickness relates to the localization of C_{80}, Cholesterol or DSPE. From the figures it is evident that C_{80} never induced thickening or thinning of the lipid bilayer in 0.15 M KCl solution.

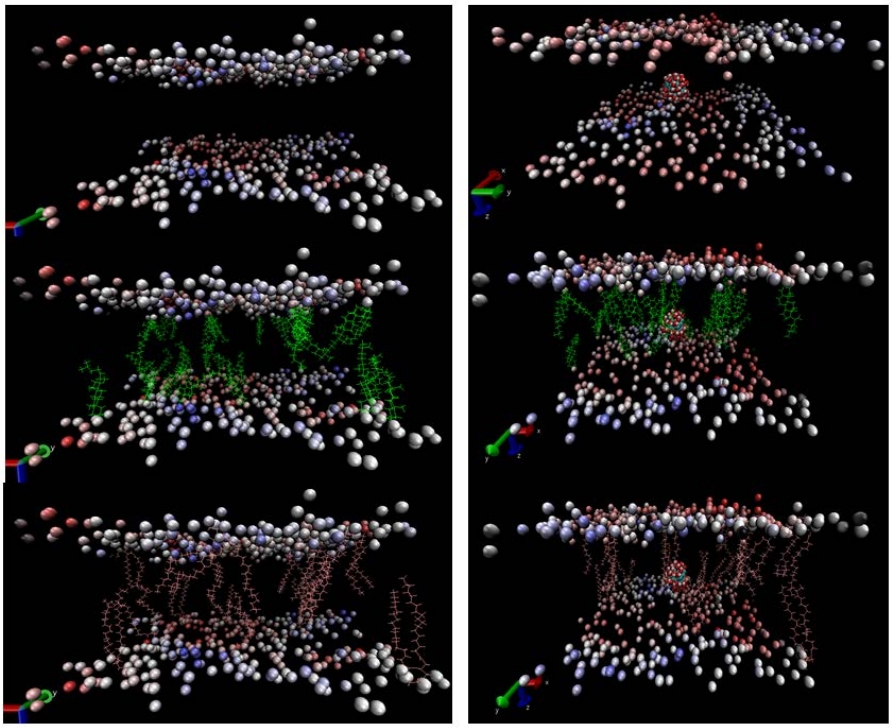

Supplementary Figure 32. Localization of $C_{80}(OH)_{42}$ Inside Lipid Bilayer Immersed in KCl Solution after 10 ns Simulation Window (similar to Figure 25 but 10 ns earlier). A lipid bilayer free of $C_{80}(OH)_{42}$ is shown on the left column and on the right $C_{80}(OH)_{42}$ containing lipid bilayer. The figures from top to bottom represent, the localization of $C_{80}(OH)_{42}$ off the center closer to lipid head group, localization of CHOL and the localization of DSPE inside the lipid bilayer respectively. The lipid bilayers are drawn on BWR color scale (35-45 Å thickness) to indicate if lateral bilayer thickness change relates to the localization of $C_{80}(OH)_{42}$, cholesterol or DSPE. From the figures it is evident that C_{80} never induced thickening or thinning of the lipid bilayer in 0.15 M KCl solution.

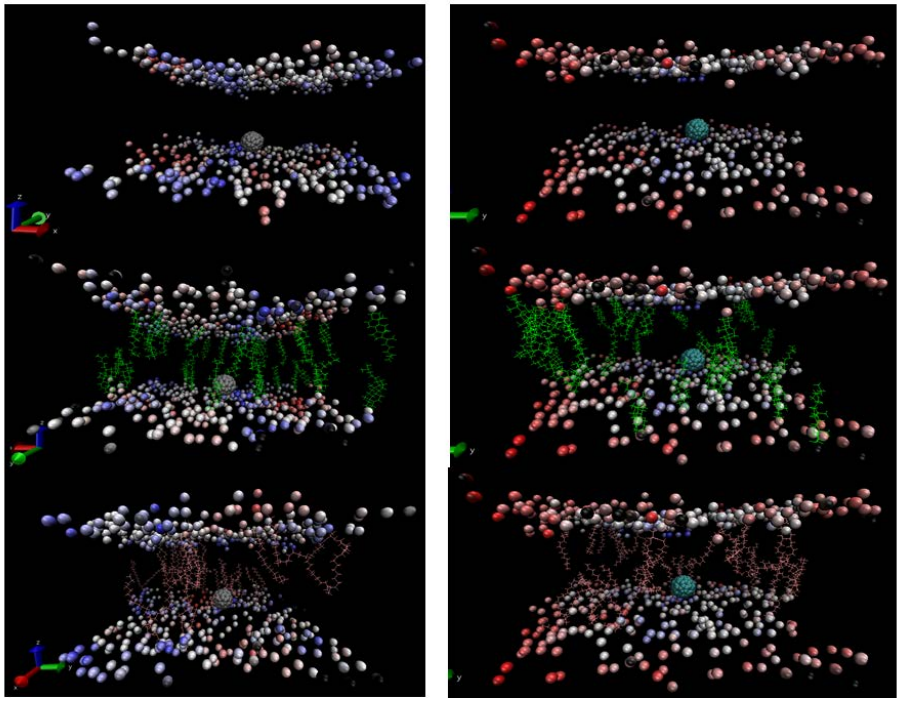

Supplementary Figure 33. Comparison of the Localization of C_{80} Inside Lipid Bilayer Immersed in KCl and $CaCl_2$ Solutions after 10 ns Simulation (similar to Figure 26 but 10 ns earlier). A lipid bilayer containing C_{80} in KCl solution is shown on the left column and C_{80} containing lipid bilayer in $CaCl_2$ solution on the right. The figures from top to bottom represent, the localization of C_{80} off the center closer to lipid head group, localization of CHOL and the localization of DSPE inside the lipid bilayer respectively. The lipid bilayers are drawn on BWR color scale (35-45 Å thickness) to indicate if a change in bilayer thickness relates to the localization of C_{80}. From the figures it is evident that C_{80} never induced thickening or thinning of the lipid bilayer solvated with 0.15 M $CaCl_2$ solution. However, the thickening on the lipid bilayer in $CaCl_2$ compared to the on in KCl solution could be attributed to the Ca^{++}.

APPENDIX B

SUPPLEMENTARY FILES

Supplementary information 1. The file contains supplementary movie which indicates the Brownian motion of liposomes captured using Nanosight Nano tracking analysis. The file is associated to Figure *5*.

Supplementary information 2. The file contains supplementary movie which indicates the dynamics of C_{80} inside POPC: DSPE: Cholesterol lipid bilayer immersed in KCl solution. The file is associated to Figure *24*.

Supplementary information 3. The file contains supplementary movie which indicates the dynamics of $C_{80}(OH)_{42}$ inside POPC: DSPE: Cholesterol lipid bilayer immersed in KCl solution. The file is associated to Figure *25*.

Supplementary information 4. The file contains supplementary movie to indicate the dynamics of C_{80} inside POPC: DSPE: Cholesterol lipid bilayer immersed in $CaCl_2$ solution. The file is associated to Figure *26*.

Supplementary information 5. The file contains supplementary movie to indicate steered molecular dynamics simulation of C_{80} inside POPC: DSPE: Cholesterol lipid bilayer immersed in NaCl solution. The file is associate to Figure *27*.

Supplementary information 6. The file contains supplementary movie to indicate steered molecular dynamics simulation of C_{80} inside POPC: DSPE: Cholesterol lipid bilayer immersed in $CaCl_2$ solution. The file is associated to Figure *28*.

Supplementary information 7. The file contains supplementary movie to indicate steered molecular dynamics simulation of C_{80} inside POPC: DSPE: Cholesterol lipid bilayer immersed in KCl solution. The file is associated to Figure *30*.

Supplementary information 8. The file contains supplementary movie to indicate steered molecular dynamics simulation of $C_{80}(OH)_{42}$ inside POPC: DSPE: Cholesterol lipid bilayer immersed in KCl solution. The file is associated to Figure *30*.